

Translationally Accelerating Wings in Ground Effect

A Numerical Study

Chinmaya Pathanadka

Master of Science Thesis

Translationally Accelerating Wings in Ground Effect

A Numerical Study

by

Chinmaya Pathanadka
Student number: 5040086

in partial fulfillment of the requirements for the degree of

Master of Science
in Mechanical Engineering

at the Delft University of Technology,
to be defended publicly on Monday February 22, 2022 at 1430 hrs.

Committee: Prof. dr. ir. J. Westerweel, TU Delft
Dr. ir. G. E. Elsinga, TU Delft
Dr. ir. M. J. B. M. Pourquie, TU Delft
Ing. E. F. J. Overmars, TU Delft
Dr. ir. A. H. van Zuijlen, TU Delft

An electronic version of this thesis is available at <http://repository.tudelft.nl/>.

Faculty of Mechanical, Maritime and Materials Engineering (3mE) · Delft University of
Technology



Copyright ©
All rights reserved.

“When you have eliminated all which is impossible, then whatever remains, however improbable, must be the truth.”

Arthur Conan Doyle

Acknowledgements

During the course of this thesis, I have been able to evolve as an engineer and an individual owing to the immense support I have received from the people around me, as I worked through the highs and lows that I encountered during this journey.

Firstly, I would like to express my profound gratitude to my supervisors, Dr. Pourquie, Dr. Elsinga and Ing. Overmars for their constant advice and aid during this project. The queries put forward by them during our interactions have always galvanized me to expand the limits of my knowledge to gain more insights into the physics of the research. Furthermore, I would like to thank Prof.dr.ir. J. Westerweel and Dr.ir. A.H. van Zuijlen for accepting to be part of the thesis committee.

I am indebted to Dr. Pourquie for inspiring me to work in the field of CFD, which goes all the way back to his Modelling of Thermo- & Hydrodynamics course. His immense knowledge in CFD and ability to make complex topics look simple is something that I will always look up to. I admire Dr. Elsinga's technical acumen in aerodynamics and his patience, which have helped me to understand the physical mechanisms by using the fundamentals. I would further like to extend my gratitude to Ing. Overmars for being kind enough to answer my questions in a simple manner and providing me with suggestions that have helped me bridge the gap between fundamentals and practical applications in the world of motorsports.

I would also like to acknowledge the contributions of Dr. Tam in uplifting my interests in fluid sciences. The ease and grace with which he explains the concepts, be it sophisticated or trivial, is something that I will always admire.

Lastly, I would like to thank my parents and family for their support and encouragement. I would also like to thank my friends in Delft and back in India for providing me with much-needed moments of inspiration, and making this journey fun and memorable.

Chinmaya Pathanadka
February 22, 2022

Abstract

Aerodynamics has played a significant role in the industry of motorsports in improving the performance and handling of the race car. Rob Smedley, the former head of vehicle performance at Williams Racing stated that *Where teams have problems is when their development or simulation environment – so CFD [Computational Fluid Dynamics] or wind tunnel – doesn't describe well what happens in reality (although in truth, no-one's wind tunnel correlates absolutely 100%)*. One of the reasons for this poor correlation could be arising from the fact that, in real life on track scenarios, the race cars undergo accelerating, decelerating or cornering motion which can have a different influence on the aerodynamics of a race car which is not accounted for in the wind tunnel and simulation environment where a steady constant flow is employed. This research aims to numerically investigate the flow past the front wing of a Formula One car in ground effect subjected to accelerating and decelerating flows in order to understand the trends in the aerodynamic performance.

A scaling analysis is performed to determine the relevant non-dimensional numbers that influence the flow for translationally accelerating airfoils and two dimensionless numbers are arrived at, namely; the Reynolds number and the Froude number. Numerical investigations are carried out for translationally accelerating wings in ground effect to determine the influence of these dimensionless numbers on the aerodynamic forces.

Transient simulations were performed on a two-dimensional airfoil and a three-dimensional wing in ground effect subjected to translational acceleration and deceleration. The Shear Stress Transport (SST) based on $k - \omega$ was employed to model the turbulent flow. The results from the numerical investigations revealed a temporary change in the downforce and the drag force coefficients, as the airfoil (or wing) in ground effect is subjected to translational acceleration (or deceleration). In this study, the mechanisms that contribute to this temporary change in the aerodynamic force coefficients are discussed.

Keywords: *Ground effect, Downforce, Vortical Structures, Computational fluid dynamics, Turbulence modelling, Added Mass.*

Nomenclature

Abbreviations

AOI	Angle of Incidence
CFD	Computational Fluid Dynamics
DNS	Direct Numerical Simulations
LDA	Laser Doppler Anemometry
LES	Large Eddy Simulations
PIV	Particle Image Velocimetry
RANS	Reynolds Averaged Navier Stokes Equations
SST	Shear Stress Transport
UDF	User Defined Function

Physical constants

g	Acceleration due to gravity	9.81 m s^{-2}
-----	-----------------------------	-------------------------

Variables

a	Translational acceleration
c	chord length
f	Frequency
h	Ground clearance
k	Turbulent kinetic energy
P	Pressure
s	Strain rate tensor
t	Time
u, v, w	Velocity components
V	Translational velocity

Greek variables

α	Angle of incidence
δ	Dirac delta function
ϵ	Turbulent dissipation rate

Γ	Circulation
μ	Dynamic viscosity
∇	Nabla operator
ν	Kinetic viscosity
ω	Specific dissipation rate
ρ	Density
Σ	Sigma operator
σ	Molecular viscosity stress
τ	Wall shear stress

Superscripts

'	Perturbation
—	Averaged value
·	Time rate
\wedge	Vector in non-inertial frame

Vectors

Ω	Vorticity
\mathbf{u}	Velocity

Subscripts

(i, j, k)	Mutually perpendicular cartesian directions
∞	Far field region
<i>exp</i>	Experiment
<i>L</i>	Laminar
<i>sim</i>	Simulation
<i>t</i>	Turbulent

Non dimensional numbers

$-C_L$	Downforce coefficient
C_D	Drag force coefficient
C_P	Pressure coefficient
<i>Fr</i>	Froude number
<i>Re</i>	Reynolds number
<i>St</i>	Strouhal number

Table of Contents

Acknowledgements	ii
Abstract	iv
Nomenclature	vii
List of Figures	xiii
List of Tables	xxiv
1 Introduction	1
1-1 Background	1
1-2 Literature Review	2
1-2-1 Generation of downforce & its significance in motorsports	2
1-2-2 Ground Effect Aerodynamics	4
1-2-3 Boundary Layer & Separated Flow	4
1-2-4 Experimental investigations on wings in ground effect	6
1-2-5 CFD investigations on wings in ground effect	11
1-2-6 Vortical Structures	13
1-2-6-1 Definition of a Vortex	13
1-2-6-2 Vortex Formation	14
1-2-6-3 Tip Vortex Formation Mechanism: Rectangular Planform Wing	14
1-2-6-4 Vortical Structures: Inverted airfoil with endplates	16
1-2-7 Accelerating Flows	17
1-2-8 Theoretical treatment of accelerating flows	21
1-3 Research Motivation, Questions & Goals	24

2	Numerical modelling	26
2-1	Geometry and Flow Scenarios	26
2-1-1	2-Dimensional Single Element Inverted Airfoil	26
2-1-2	3-Dimensional Single Element Inverted Airfoil	26
2-1-3	Flow Scenarios	27
2-1-3-1	Case 1: Piecewise Linear Velocity Profile	27
2-1-3-2	Case 2: Non-linear Velocity Profile	27
2-2	Meshing	28
2-3	Governing Equations & Turbulence Modelling	29
2-4	Computational Domain & Type of Boundary Conditions	31
2-4-1	2D Computational Domain	31
2-4-2	3D Computational Domain	32
2-5	Solution Methods	34
2-6	Turbulence Model Validation Study	35
3	Results and discussion	37
3-1	Mesh independence study	37
3-2	Navier Stokes Equation in the non-inertial frame: A Scaling Analysis	40
3-3	Translational Acceleration & Deceleration:2-Dimensional Airfoil	42
3-3-1	Piecewise Linear Velocity Profile	42
3-3-2	Non-linear Smooth Velocity Profile	46
3-3-2-1	2-Dimensional Airfoil: Ground Clearance $h=0.179c$ & Aspect Ratio=1	46
3-3-2-2	2-Dimensional Airfoil: Ground Clearance $h=0.179c$ & Aspect Ratio=1	51
3-3-2-3	2-Dimensional Airfoil: Ground Clearance $h=0.179c$ & Aspect Ratio=1	60
3-4	Translational Acceleration & Deceleration:3-Dimensional Airfoil	67
3-4-1	Velocity & Acceleration profile for the accelerating airfoil	67
3-4-1-1	Primary & Secondary Vortices for a Steady Flow	68
3-4-2	Downforce generated by the airfoil & the drag force on the airfoil	69
3-4-2-1	Streamwise Vorticity: Translationally Accelerating and Decelerating Airfoil	73
3-4-2-2	Behavior of the Flow Separation Point	77
3-4-3	Influence of the magnitude of acceleration on the downforce and drag force of the translationally accelerating & decelerating airfoil	79
3-5	Translational Acceleration: Validation with the Experimental Results	85
3-5-1	Velocity & Acceleration profile for the accelerating airfoil	85
3-5-2	Downforce generated by the airfoil & the drag force on the airfoil	86
4	Conclusions	89
4-1	Summary	89
4-2	Recommendations	91

A Tyrrell Wing Profile	92
B Eddy viscosity models	94
C Accelerating Airfoil: Moving Frame of Reference and Stationary Frame of Reference	96
C-1 Boundary Conditions	97
C-2 Results: Forces and Flow Fields	97
D Fluent settings	99
Bibliography	101

List of Figures

1-1	Lotus 79: First car to take full advantage of ground effects aerodynamics [1] . . .	1
1-2	Downforce generation for an inverted airfoil.	3
1-3	Influence of drag and downforce on the limit speed of an F1 car at three different corners[2]. The impact of downforce and the drag reduction on speed is more evident in the high-speed corner A when compared to corners B and C, where a significant improvement in speed is observed.	3
1-4	Typical growth of boundary layer thickness over an airfoil section [3]	4
1-5	Laminar separation bubble [3]	5
1-6	Illustration of flow regimes over the suction side of an airfoil: (a) fully attached laminar followed by turbulent boundary layer flow over the suction side; (b) laminar, leading edge separation without reattachment of flow over the suction side; (c) laminar followed by turbulent boundary layer with separation near the trailing edge. [3]	6
1-7	Downforce and drag coefficient versus ground clearance for an inverted LS(1)-0413 airfoil [4]. $[\alpha = 1^\circ, \text{Re} = 2 \times 10^6, \text{moving ground plane}]$	7
1-8	Side view of Tyrrell 26 wing model with endplates at ride height h_r [5]. The Tyrrell wing profile(indicated by the solid line) is developed from the LS(1)-0413 MOD wing profile(indicated by the dashes). The rectangular plates attached to the wing at the sides are referred to as endplates.	8
1-9	Oil flow visualization on suction surface, leading edge lowermost: (a) $h_r/c = 0.134$, (b) $h_r/c = 0.090$, (c) $h_r/c = 0.067$ [5]. The direction of the flow is from bottom to top. At $x/c \sim 0.3$, transition through means of the short reattachment bubble is observed for all three ride heights. For the ride height $h/c = 0.134$, a small region of separated flow can be observed at the central portion of the suction side of the wing at the trailing edge. For the ride height $h/c = 0.09$, an increase in the region of separated flow is observed. On reducing the ride height further, at $h/c = 0.067$, a further increase in the region of separated flow is observed.	9

1-10	Downforce at varying incidences as a function of ride height h_r [5]. A greater value of the maximum downforce is observed on increasing the angle of incidence, and a lower gradient for the downforce with height curve is observed. Furthermore, the ground clearance at which maximum ground clearance is generated increases on increasing the angle of incidence, since the flow separation and downforce loss occur at a higher value of ground clearance than for the low angle of incidence case.	10
1-11	An illustration of the vortices generated for the Tyrrell 26 wing [6]. The contour in the image reveals the streamwise vorticity component, Ω_x .	11
1-12	Comparison of experimental and computational wake surveys at $x/c = 1.2$ for $h/c = 0.134$ [7]. The velocities outside the wake region returned by the CFD models are lower than that observed in the experiment. The thickness of the wake is captured by CFD is slightly thicker on comparing with the experimental results.	12
1-13	Mesh structure about inverted Tyrrell airfoil; inset - entire domain mesh [8]	13
1-14	Hurricane Katrina as viewed from a satellite: An example of a naturally occurring vortex [9]	14
1-15	Roll-up of an inviscid vortex sheet into two trailing vortices of equal strength [10]	15
1-16	Wing tip vortices shed from a rectangular planform wing, made visible by smoke filaments [11]	16
1-17	Primary and secondary vortices' location in the straight line scenario [12]	16
1-18	The reference velocity average transient responses determined from 490 transients [13]	17
1-19	The separation chord position responses to the accelerating and decelerating transients [13]. For the accelerating flow, the location of the separation point moves slightly downstream when compared to its steady state location (at $Re_c = 150000$). For the decelerating flow, the location of the separation point moves upstream when compared to its steady state location (at $Re_c = 100000$).	17
1-20	The transition chord position responses to accelerating and decelerating transients [13]. For the accelerating flow, the location of the transition point moves downstream when compared to its location at steady state. For the decelerating flow, the location of the transition point moves upstream when compared to its location at steady state.	18
1-21	NACA 2412 airfoil (a) Subsonic drag at steady and $+0.8845g$, (b) Subsonic lift at steady and $+0.8845g$ [14]	19
1-22	Dimensions and the orientation of the flat plate used for carrying out the experiment [15]. The flat plate immersed in the RowBot tank was accelerated in the x-direction to study the of acceleration on the drag force.	20
1-23	(a) Flat plate velocity and (b) Flat plate acceleration as a function of time t [15].	20
1-24	Drag force on the accelerating flat plate determined experimentally for an immersion depth $h = 100$ mm determined experimentally, along with the theoretical drag force and its components F_{CD} and F_{vm} using the Equation 1-5 [15].	21

1-25	The <i>Frame O</i> is the inertial frame, which is stationary. <i>Frame O'</i> is the non-inertial frame which preserves the orientation. <i>Frame O'</i> accounts for relative translation motion between the inertial and the non-inertial frame. <i>Frame \hat{O}</i> is the non-inertial rotating frame which does not preserve the orientation. <i>Frame \hat{O}</i> accounts for the rotation between the inertial and non-inertial frame. P is the point mass(airfoil, in this instance)	23
2-1	Piecewise linear velocity profile(s) with which the airfoil is accelerated(and decelerated), and the corresponding acceleration profile(s). The velocity profile used for accelerating(and decelerating) the airfoil is generated using the Equation 2-1 . . .	27
2-2	The non-linear velocity with which the airfoil is accelerated(and decelerated) and the corresponding acceleration profiles. The non-linear velocity profiles for accelerating the airfoil is generated using the Equation 2-2	28
2-3	Structured grid for a 2D Tyrrell wing with $h/c = 0.179$ at $\alpha = 3.45^\circ$	32
2-4	Hybrid grid for a 2D Tyrrell wing with $h/c = 0.224$ at $\alpha = 3.45^\circ$	33
2-5	Hybrid grid for a 2D Tyrrell wing with $h/c = 0.224$ at $\alpha = 3.45^\circ$	33
2-6	Experimental aerodynamic downforce for a single element airfoil in ground effect at $\alpha = 3.45^\circ$ from Zerihan et al.[7] is compared with the aerodynamic downforces returned by the four different eddy viscosity turbulence models.	35
2-7	Wall Shear Stress values on the suction side of the airfoil at $\alpha = 3.45^\circ$ for $h/c = 0.179$	36
2-8	Experimental surface pressure distribution on the airfoil at $\alpha = 3.45^\circ$ for $h/c = 0.179$ [7] compared with the surface pressure distributions returned by the four eddy viscosity models	36
3-1	Variation of (a)downforce coefficient and (b)drag coefficient for the five different grids. The force coefficient decreases with increase in the number of points on the airfoil and asymptotically approach a constant value.	37
3-2	2D Airfoil surface pressure distribution for the fine mesh, i.e., the one with 600 points on the airfoil circumference. Comparisons with the experimental values of pressure distribution [7] reveal no significant difference in the pressure distribution at $z= 0$ plane for the ride height, $h/c = 0.179$	38
3-3	3D Airfoil surface pressure distribution at the mid-plane for the fine mesh, i.e., the one with 600 points on the airfoil circumference. Comparisons with the experimental values of pressure distribution [7] reveal no significant difference in the pressure distribution at $z= 0$ plane for the ride height, $h/c = 0.224$	38
3-4	Contours of non-dimensional AC/U^2 in the Equation 3-4 for a unit chord length for velocities in the range 1-100 m/s and acceleration in the range 1-100 ms^{-2} (Note that the x-axis(velocity) is in the log scale).	41
3-5	(a)Downforce generated by the airfoil accelerated with the piecewise linear velocity profile, (b)Drag force on the airfoil accelerated with the piecewise linear velocity profile.	42

- 3-6 (a) Downforce generated by the accelerating airfoil with the piecewise linear velocity profile, (b) Drag force on the airfoil accelerated with the piecewise linear velocity profile. The downforce generated at the same steady state velocities as the accelerating (or decelerating) airfoil reveal no significant differences, while the drag force encountered by the accelerating (or decelerating) airfoil is higher (or lower) than that encountered by the airfoil at the same steady state velocities. 43
- 3-7 (a) Pressure drag and viscous drag contributions to total drag encountered by the airfoil accelerated with the piecewise linear velocity profile, (b) Pressure drag and viscous drag contributions to total drag encountered by the airfoil accelerated with the piecewise linear velocity profile, with baseline correction. The plots reveal that the peaks observed in the total drag force at the start and end of the acceleration are a result of the pressure drag. 44
- 3-8 (a) Pressure drag on the airfoil accelerated (and decelerated) with the piecewise linear velocity profile. The pressure drag on the airfoil at the same steady state velocities as the accelerating (or decelerating) airfoil reveal that the drag force encountered by the accelerating (or decelerating) airfoil is higher (or lower) than that encountered by the airfoil at the same steady state velocities. (b) Viscous drag on the airfoil accelerated (and decelerated) with the piecewise linear velocity profile. The viscous drag at the same steady state velocities as the accelerating (or decelerating) airfoil reveal no significant differences. 45
- 3-9 (a) Velocity profiles for accelerating and decelerating airfoil, (b) Acceleration profile for accelerating and decelerating airfoil 46
- 3-10 (a) Downforce generated by the airfoil accelerated with the non-linear velocity profile, (b) Drag force on the airfoil accelerated with the non-linear velocity profile 47
- 3-11 (a) Instantaneous downforce coefficient for the airfoil accelerated with the non-linear velocity profile, (b) Instantaneous drag coefficient for the airfoil accelerated with the non-linear velocity profile. The instantaneous force coefficients are obtained by non-dimensionalizing the forces with the instantaneous free stream velocity using the Equation 3-10 47
- 3-12 (a) Normalized downforce coefficient for the airfoil accelerated with the non-linear velocity profile, (b) Normalized drag coefficient for the airfoil accelerated with the non-linear velocity profile. The normalized force coefficients reveal that the accelerating airfoil undergoes a 1 % loss in the downforce and experiences an additional drag force of 10%. Similarly, the decelerating airfoil experiences a 4% gain in the downforce and encounters a 30% reduction in the drag force. 48
- 3-13 (a) Downforce generated by the accelerating airfoil at the angle of incidence 3.45° , (b) Downforce coefficient for the accelerating airfoil at the angle of incidence 3.45° . The downforce coefficients indicate that the accelerating airfoil experiences a 3% loss in downforce when compared to the airfoil at the same steady state velocity at $t = 3s$ 48

- 3-14 (a) Drag force on the accelerating airfoil at the angle of incidence 3.45° , (b) Drag force coefficient for the accelerating airfoil at the angle of incidence 3.45° . The drag force coefficients indicate that the accelerating airfoil experiences a 7% increase in the drag force when compared to the airfoil at the same steady state velocity at $t = 3s$ 49
- 3-15 (a) Pressure distribution on the airfoil suction side at $t = 3s$ normalized with dynamic pressure $\frac{1}{2}\rho U_\infty^2$ for the accelerating airfoil. The pressure distribution on the suction side is not as low as the pressure distribution at the same velocity under steady state conditions, resulting in a loss of the downforce. (b) Pressure distribution on the airfoil suction side at $t = 4s$ normalized with dynamic pressure $\frac{1}{2}\rho U_\infty^2$ for the decelerating airfoil. The pressure distribution on the suction side is not as high as the pressure distribution at the same velocity under steady state conditions, resulting in a gain in the downforce. 49
- 3-16 (a) Pressure drag and (b) Viscous drag force on the accelerating airfoil at the angle of incidence 3.45° compared with the drag on the airfoil at the same steady state velocities. 50
- 3-17 (a) Downforce generated by the accelerating airfoil at varying angle of incidences(AOI), (b) Drag force on the accelerating airfoil at varying angle of incidences(AOI). As the angle of incidence is increased, the amount of downforce generated by the airfoil increases. Increased angle of incidence results in an increase in the drag force 51
- 3-18 Vortex Shedding, indicated by the contours of z-component of vorticity, Ω_z , at the trailing edge of the airfoil at $h/c = 0.179$, as a result of the interaction between the two separated layers on the pressure and suction side of the airfoil 52
- 3-19 (a) Downforce generated by the accelerating airfoil at the angle of incidence, 13.45° and $h/c = 0.179$ for the 2g acceleration profile in Figure 3-9 (b) Downforce oscillations induced by the vortex shedding at trailing edge, with a frequency $f \sim 90$ Hz. For a constant Strouhal number, the shedding frequency varies linearly with the inflow velocity 52
- 3-20 (a) Downforce coefficient for the accelerating airfoil at angles of incidences 3.45° and 5.45° , (b) Drag force coefficient for the accelerating airfoil at angles of incidences 3.45° and 5.45° 53
- 3-21 (a) Normalized downforce coefficient for the accelerating airfoil at angles of incidences 3.45° and 5.45° , (b) Normalized drag coefficient for the accelerating airfoil at angles of incidences 3.45° and 5.45° . The normalized force coefficients indicate that the accelerating airfoil at the angle of incidence 3.45° is influenced by the acceleration more than the accelerating airfoil at the angle of incidence 5.95° . . 53
- 3-22 (a) Downforce generated by the accelerating airfoil at the angle of incidence 5.95° , (b) Downforce coefficient for the accelerating airfoil at the angle of incidence 5.95° . The downforce coefficients indicate that the accelerating airfoil experiences a 1% loss in downforce when compared to the airfoil at the same steady state velocity at $t = 3s$ 54

3-23	(a) Drag force on the accelerating airfoil at the angle of incidence 5.95° , (b) Drag force coefficient for the accelerating airfoil at the angle of incidence 5.95° . The drag force coefficients indicate that the accelerating airfoil experiences a 14% increase in the drag force when compared to the airfoil at the same steady state velocity at $t = 3s$	55
3-24	Convective acceleration contour for the translationally accelerating airfoil at the angle of incidence 3.45° at $t = 3.0 s$	56
3-25	Locations of the probes used to measure the convective acceleration encountered by the translationally accelerating airfoil at $x/c = 0.0$, $x/c = 0.2$ and $x/c = 0.4$	56
3-26	Instantaneous convective acceleration encountered by the translationally accelerating airfoil at the angle of incidence 3.45° at the probe location $x/c = 0.0$	57
3-27	Variation of the non-dimensional term 3 in the Equation 3-4 during the course of acceleration	57
3-28	Instantaneous convective acceleration encountered by the translationally accelerating airfoil at the angle of incidence 3.45° at the probe location $x/c = 0.4$	58
3-29	Instantaneous convective acceleration encountered by the translationally accelerating airfoil at the angle of incidence 5.95° at the probe location $x/c = 0.0$	58
3-30	Instantaneous convective acceleration encountered by the translationally accelerating airfoil at the angle of incidence 5.95° at the probe location $x/c = 0.2$	59
3-31	Instantaneous convective acceleration encountered by the translationally accelerating airfoil at the angle of incidence 5.95° at the probe location $x/c = 0.4$	59
3-32	(a) Velocity profiles for the accelerating airfoil generated using the Equation 2-2, (b) Corresponding acceleration profiles for the accelerating airfoil.	60
3-33	(a) Downforces generated by the accelerating airfoil for the three different velocity profiles in the Figure 3-32, (b) Drag force on the accelerating airfoil for the three different velocity profiles in the Figure 3-32	61
3-34	(a) Downforce coefficient for the accelerating airfoil for the three different velocity profiles in the Figure 3-32, (b) Drag force coefficient for the accelerating airfoil for the three different velocity profiles in the Figure 3-32. The force coefficient curves exhibit the influence of magnitude of acceleration for the accelerating airfoil.	61
3-35	(a) Normalized downforce coefficient for the accelerating airfoil with the peak acceleration value $2g$, (b) Normalized drag force coefficient for the accelerating airfoil with the peak acceleration value $2g$. The normalized force coefficients indicate that the accelerating airfoil undergoes a 1% loss in the downforce and encounters a 12% gain in the downforce.	62
3-36	(a) Normalized downforce coefficient for the accelerating airfoil with the peak acceleration value $5g$, (b) Normalized drag force coefficient for the accelerating airfoil with the peak acceleration value $5g$. The normalized force coefficients indicate that the accelerating airfoil undergoes a 3% loss in the downforce and encounters a 25% gain in the drag force.	62

3-37 (a) Normalized downforce coefficient for the accelerating airfoil with the peak acceleration value 8g, (b) Normalized drag force coefficient for the accelerating airfoil with the peak acceleration value 8g. The normalized force coefficients indicate that the accelerating airfoil undergoes a 10% loss in the downforce and encounters a 450% gain in the drag force.	63
3-38 (a) Normalized downforce coefficient for the accelerating airfoil with varying peak acceleration values, (b) Normalized drag force coefficient for the accelerating airfoil with varying peak translational acceleration values. The normalized coefficient curves indicate that the higher the magnitude of acceleration, the higher is the influence of acceleration on the forces.	63
3-39 Convective acceleration contours encountered at three different peak values of translational acceleration. The lower the value of peak translational acceleration, the higher the magnitude of convective acceleration encountered by the translationally accelerating airfoil.	64
3-40 Variation of the non-dimensional <i>Term 3</i> in the Equation 3-4 when the airfoil is subjected to different values of peak translational acceleration. These plots reveal the magnitude of the <i>Term 3</i> when compared to the non-linear term corresponding to the convective acceleration encountered by the translationally accelerating airfoil, which is of order 1, from the Equation 3-4.	65
3-41 Inverted airfoil with endplates. The chord length c is 223.4 mm and the dimensions of the endplate used are $250 \times 100 \times 4$ mm	67
3-42 Average velocities(in km/h), followed by the gear at various points on the Spa-Francorchamps track [16]. We limit our discussion to Turn 1, i.e., La Source, where the car undergoes '5g' deceleration as it brakes into the corner and undergoes '2g' acceleration as it accelerates out of the corner. Finlay et al. [16] arrive at these values of acceleration and deceleration using the velocity and time data available to them.	67
3-43 (a)Velocity profiles for accelerating and decelerating the 3-dimensional airfoil with endplates, (b)Acceleration profile for accelerating and decelerating 3-dimensional airfoil with endplates	68
3-44 Non-dimensional streamwise vorticity, i.e., $(\Omega_x c)/U_\infty$ contours for $h/c = 0.224$ at $x/c = 1.2$ for a streamwise Reynolds number of 4.5×10^6 : (a) Experimental results [6] (b) CFD results for the SST $k-\omega$ model. The SST $k-\omega$ model captures main vortical structures reasonably well, when compared to the vortical contours captured experimentally.	69
3-45 (a)Downforce generated by the airfoil accelerated with the non-linear smooth velocity profile, (b)Drag force on the airfoil accelerated with the non-linear smooth velocity profile	69
3-46 (a)Instantaneous downforce coefficient for the 3D airfoil translationally accelerated with the smooth non-linear velocity profile, generated using the Equation 3-10, (b)Same data as (a), but normalized with the instantaneous force coefficient at $t = 0.0s$	70

3-47 (a)Instantaneous drag force coefficient for the 3D airfoil translationally accelerated and decelerated with the smooth non-linear velocity profile, generated using the Equation 3-10, (b)Same data as (a), but normalized with the instantaneous force coefficient at $t = 0.0s$	70
3-48 (a)Instantaneous downforce coefficient and (b)Instantaneous drag force coefficient for the translationally accelerated 3D airfoil compared with the downforce coefficients at the same steady state velocities. The translationally accelerating airfoil generates less downforce than when compared to that generated at the same steady state velocities. The drag force experienced by the translationally accelerated airfoil is higher than that experienced at the same steady state velocities	71
3-49 (a)Instantaneous downforce coefficient and (b)Instantaneous drag force coefficient for the translationally decelerated 3D airfoil compared with the downforce coefficients at the same steady state velocities. The translationally decelerating airfoil generates more downforce than when compared to that generated at the same steady state velocities. The drag force experienced by the translationally accelerated airfoil is lower than that experienced at the same steady state velocities. . .	72
3-50 Pressure distribution on the airfoil in the mid-plane (i.e, $z=0$) at $t = 2.5s$ normalized with instantaneous dynamic pressure $\frac{1}{2}\rho U_{\infty}^2$ for the translationally accelerating airfoil. The pressure distribution on the suction side is not as low as the pressure distribution at the same velocity under steady state conditions, resulting in a loss of the downforce. (b)Pressure distribution on the airfoil in the mid-plane (i.e, $z=0$) at $t = 2.5s$ normalized with instantaneous dynamic pressure $\frac{1}{2}\rho U_{\infty}^2$ for the translationally decelerating airfoil. The pressure distribution on the suction side is not as high as the pressure distribution at the same velocity under steady state conditions, resulting in a gain in the downforce.	72
3-51 The trends in contours of streamwise vorticity non-dimesionalized with instantaneous free stream velocity from $t = 0.0 s$ to $2.0 s$ at $x/c = 1.2$, when airfoil is accelerated translationally	73
3-52 The trends in contours of streamwise vorticity non-dimesionalized with instantaneous free stream velocity from $t = 2.5 s$ to $5.0 s$ at $x/c = 1.2$, when the airfoil is accelerated translationally	74
3-53 The trends in contours of streamwise vorticity non-dimesionalized with instantaneous free stream velocity from $t = 0.0 s$ to $2.0s$ at $x/c = 1.2$, when airfoil is decelerated translationally	75
3-54 The trends in contours of streamwise vorticity non-dimesionalized with instantaneous free stream velocity from $t = 2.5 s$ to $5.0 s$ at $x/c = 1.2$, when the airfoil is accelerated translationally	76
3-55 Response of the location of separation point to translational acceleration. The location of the separation point is indicated by the change in sign of the x-wall shear stress.(a) Instantaneous x-wall shear stress on the airfoil suction side at the mid-plane(i.e., $z = 0$), (b) Enhanced image of the encircled region. The enhanced image of the x-wall shear stress reveals that, the location of the separation point moves downstream with time when the airfoil is accelerated translationally, until there is no flow separation.	77

3-56	Response of the location of separation point to translational deceleration. The location of the separation point is indicated by the change in sign of the x-wall shear stress.(a) Instantaneous x-wall shear stress on the airfoil suction side at the mid-plane(i.e., $z = 0$), (b) Enhanced image of the encircled region. The enhanced image of the x-wall shear stress reveals that, the location of the separation point moves upstream with time when the airfoil is decelerated translationally from the onset of separation.	78
3-57	Instantaneous x-wall shear stress in the mid-plane for (a) Translationally accelerating airfoil at $t = 2.1s$ compared with the x-wall shear stress at the same steady state velocity, (b) Translationally decelerating airfoil at $t = 4.0s$ compared with the x-wall shear stress at the same steady state velocity. The location of the separation point for the translationally accelerating(or decelerating) airfoil, at any time t , is identical to that of the airfoil at the same steady state velocity.	78
3-58	(a)Velocity profiles for accelerating and decelerating the 3-dimensional airfoil with endplates, (b)Acceleration profile for accelerating and decelerating 3-dimensional airfoil with endplates	79
3-59	(a)Downforce generated by the translationally accelerating and decelerating 3D airfoil, (b)Drag force on the translationally accelerating and decelerating 3D airfoil	80
3-60	(a)Instantaneous downforce coefficient for the 3D airfoil translationally accelerated with the smooth non-linear velocity profile, generated using the Equation 3-10, (b)Normalized instantaneous downforce coefficient for the 3D airfoil translationally accelerated with the smooth non-linear velocity profile, generated using the Equation 3-10.	80
3-61	(a)Instantaneous drag force coefficient for the 3D airfoil translationally accelerated and decelerated with the smooth non-linear velocity profile, generated using the Equation 3-10, (b)Normalized instantaneous drag force coefficient for the 3D airfoil translationally accelerated and decelerated with the smooth non-linear velocity profile, generated using the Equation 3-10.	81
3-62	Variation of the non-dimensional <i>Term 3</i> in the Equation 3-4 when the 3D airfoil is subjected to different values of peak translational acceleration and deceleration. These plots reveal the magnitude of the <i>Term 3</i> when compared to the non-linear term corresponding to the convective acceleration encountered by the translationally accelerating airfoil, which is of order 1, from the Equation 3-4.	82
3-63	Instantaneous streamwise convective acceleration, i.e, $u \frac{\partial u}{\partial x}$ contour in the mid-plane($z = 0$) for the 3D airfoil accelerated translationally with the "8g acc" velocity profile at $t = 1.6s$	83
3-64	Magnitude of instantaneous streamwise convective acceleration of the flow encountered by the translationally accelerating and decelerating 3D airfoil in the mid-plane($z = 0$), $x/c = 1.2$ at a time t when the term AC/U^2 at its peak. . .	83
3-65	Magnitude of instantaneous streamwise convective acceleration of the flow encountered by the translationally accelerating and decelerating 3D airfoil in the mid-plane($z = 0$), $x/c = 1.2$ at a time t when the term AC/U^2 at its peak. . .	84
3-66	Velocity profile with which the airfoil is accelerated translationally in the experiment	85

3-67	(a) Velocity profile with which the airfoil is accelerated translationally in the simulation to validate the CFD model, (b) Acceleration profile as the airfoil is accelerated translationally in the simulation to validate the CFD model, with peak acceleration attained at $t = 0.5s$	85
3-68	(a) Downforce generated by the 2D airfoil accelerated translationally with the velocity profile in Figure 3-67, (b) Drag force experienced by the translationally accelerated 2D airfoil with the velocity profile in Figure 3-67	86
3-69	Starting vortex, indicated by the contour of instantaneous z-vorticity component, i.e, Ω_z at $t = 0.7s$	86
3-70	Starting vortex, indicated by the contour of instantaneous z-vorticity component, i.e, Ω_z at $t = 0.7s$	87
3-71	(a) Downforce generated by the 2D and 3D airfoil accelerated translationally with the "2g acc" velocity profile, (b) Drag force on the 2d and 3D airfoil accelerated translationally with the "2g acc" velocity profile. The downforce generated by the translationally accelerated airfoil is higher than that by the 3D airfoil, whereas the drag force experienced by the translationally accelerating 2D airfoil is lower than the 3D airfoil.	88
C-1	(a) Velocity profiles for accelerating airfoil, (b) Acceleration profile for accelerating airfoil	96
C-2	(a) Downforce generated by the accelerating airfoil, (b) Drag force on the accelerating airfoil	97
C-3	(a) Instantaneous pressure field for accelerating airfoil in the moving frame at $t = 0s$, (b) Instantaneous pressure field for accelerating airfoil in the stationary frame at $t = 0s$	98
C-4	(a) Instantaneous x-velocity field for accelerating airfoil in the moving frame at $t = 0s$, (b) Instantaneous x-velocity field for accelerating airfoil in the stationary frame at $t = 0s$	98

List of Tables

A-1	Single element wing coordinates at an angle of incidence 3.45°	93
-----	---	----

Chapter 1

Introduction

1-1 Background

Up until 1967, the application of aerodynamics in improving the performance of the Formula One racing cars was limited to careful streamlining of the single-seater unit. Other applications involved directing cool air to the brakes and the engine intakes to cool the engine water and oil heat exchangers. 1968 marked the emergence of the inverted airfoils in Formula One cars and were mounted above the front and rear axles. These resulted in a significant increase in the downforce and improved the cornering, braking and traction performances of the car. In 1977, Lotus introduced the first Formula One car to incorporate the full 'ground effect' aided by skirts and hence achieving a significant improvement in the downforce by utilizing the full plane area of the car to generate downforce instead of the relatively small airfoils on the front and rear [17]. The principle by which downforce is generated by the inverted airfoil in ground effect is explained in detail in Sections 1-2-1 and 1-2-2.



Figure 1-1: Lotus 79: First car to take full advantage of ground effects aerodynamics [1]

In this thesis, we focus on the front wing of a racecar. The front wing is a vital aerodynamic

component on the Formula One car, as it is the first part that meets the air flow. The front wing generates a wake, which directly has an effect on the flow field over the body and rear of the race car. Engineers estimate that the front wing of a race car approximately contributes one-third of the total downforce generated by a race car.

Evaluating the aerodynamic forces on a race car accurately is a key challenge faced by the aerodynamic engineers, as it enables them to gain an upper hand over their competitors. Experimental measurements obtained from the wind tunnel tests along with numerical simulations are commonly employed to predict the aerodynamic performance of a race car. Poor correlation between the wind tunnel results and on-track behavior is something which the Formula One teams complain about during the initial stages of a season. The teams carry out wind tunnel tests for a constant velocity flow, which is quite different from the on-track conditions where the race car accelerates, decelerates and does not move in a straight line in large parts of a racetrack. Furthermore, the experiments carried out at the Laboratory for Aero & Hydrodynamics in TU Delft on an accelerating flat plate, rowing-oar revealed that the aerodynamic forces were different from those observed at constant velocities. Hence, a comprehensive study is needed to investigate the aerodynamic influence on a race car during acceleration, deceleration and cornering to accurately predict on-track behavior.

1-2 Literature Review

In this section, a comprehensive review of the literature relevant to the aerodynamics of an accelerating airfoil in ground effect is presented. The principle of downforce generation and its significance in motorsports is discussed in Section 1-2-1. The fundamentals of ground effect aerodynamics and boundary layer are reviewed in Sections 1-2-2 and 1-2-3 respectively. The results from experimental and CFD investigations of airfoils in ground effect are reviewed in Sections 1-2-4 and 1-2-5 respectively. Discussions on vortical structures and accelerating flows are presented in Sections 1-2-6 and 1-2-7 respectively, while theoretical treatment of accelerating flows is presented in Section 1-2-8.

1-2-1 Generation of downforce & its significance in motorsports

The downforce is a measure of the vertical aerodynamic loads generated by the aerodynamic surfaces of a Formula One car. The principle of downforce generation is the same as that of an aircraft wing. In the case of an aircraft, wings are used to generate lift which is achieved by accelerating the air on the upper half of the wing, thus creating an area of low pressure above the wing and an area of slow moving, high-pressure air underneath the wing. This pressure difference results in an upward force of lift which enables the plane to take off. This principle is reversed in Formula One, with air being accelerated underneath the inverted wing creating a zone of low pressure beneath the wing, generating a downforce as illustrated in Figure 1-2.

Larger efforts are now being poured into the aerodynamic development of Formula One cars than ever before. Approximately, a Formula One car can generate a downforce of the order of 3-5 times the weight of the car through a high-speed corner, resulting in high cornering speeds. Figure 1-3 exhibits the influence of downforce and drag on the limit speed of a

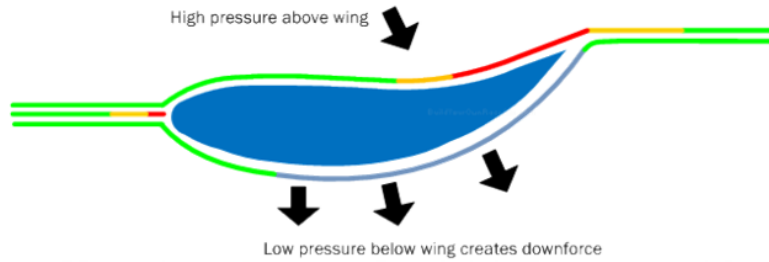


Figure 1-2: Downforce generation for an inverted airfoil.

Corner type	Speed without downforce	Speed with normal downforce	Speed increase due to downforce	Speed increase possible in corners due to drag reduction to 25% of normal value
A high-speed	139.5kph	235.5kph	69%	7.0%
B medium-speed	101.4kph	127.6kph	25%	0.34%
C low-speed	76.6kph	86.2kph	12%	0.2%

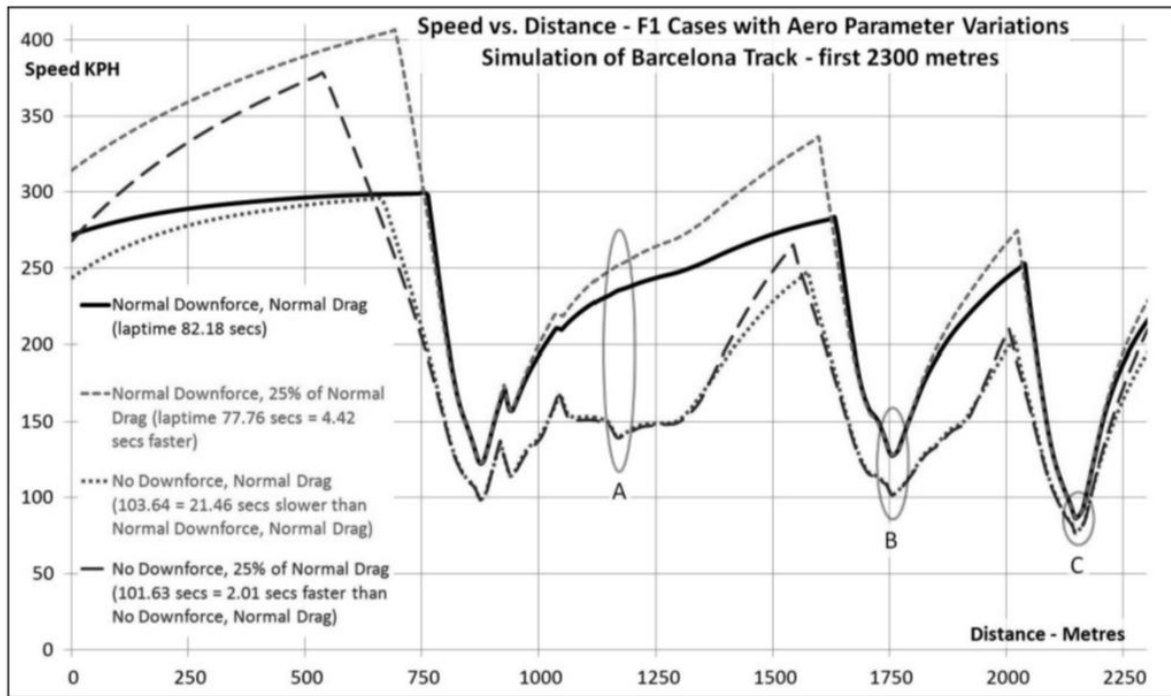


Figure 1-3: Influence of drag and downforce on the limit speed of an F1 car at three different corners[2]. The impact of downforce and the drag reduction on speed is more evident in the high-speed corner A when compared to corners B and C, where a significant improvement in speed is observed.

car for the Sauber Ferrari F1 car, along with several theoretical cars. From the lap time simulations in the Figure 1-3, it can be seen that a race car needs more downforce and less drag in corners, while on the straights it needs less downforce and less drag. Hence, in order to extract maximum performance from a race car, an optimal combination of downforce and drag is needed.

From the lap-time simulations in the Figure 1-3, it can be seen that, on removing the downforce, the lap time increases by 21.46 s when compared to the car with the normal downforce and drag. On lowering the drag to 25% of its real value (not attainable in the real world), the lap time reduces by 4.42 s when compared to the car with the normal downforce and drag. The curves in the Figure 1-3 are fairly simple to understand. When at the cornering limits because you have zero downforce, a reduction in the drag is not of much significance (until reaching the straights). Alternatively, when driving through corners at high speeds because of the downforce, the impact of drag reduction on the improving speeds is significant.

1-2-2 Ground Effect Aerodynamics

The phenomenon of ground effect can be traced back to the claims by pilots that, on approaching the ground, a cushioning effect was observed. Using a fixed ground for an RAF6 airfoil, Zham et al. [18] demonstrated that the lift increased and the drag reduced when compared to the lift and drag values in the freestream for a given angle of attack. The increase in lift of an aircraft wing on approaching the ground was explained in primitive stages of aerodynamic theory [19]. The increase in lift as a result of ground effect is attributed to reduction of the amount of induced drag generated, which improves the lift to drag ratio. When operated in proximity to the ground, the wing tip vortices, which are always generated as an airfoil moves through the air, since the pressure underneath the wing is higher than that above it, are altered. The vortices in proximity to the ground become elliptical instead of being circular. As a result, the effective aspect ratio of the wing becomes greater than its geometric aspect ratio, which results in a reduced induced drag. The geometric aspect ratio is the ratio of the span of the wing to its chord. This phenomenon works as well for inverted wings, which are used in racing cars to increase the downforce. The aerodynamic downforce generated by the inverted wing is used to supplement the low mechanical downforce of a lightweight racing car and increase the tire load without increasing the weight of the car that could affect the performance of the car. The mechanical downforce of a car is a function of the mass of the car, tires and its suspension setup.

1-2-3 Boundary Layer & Separated Flow

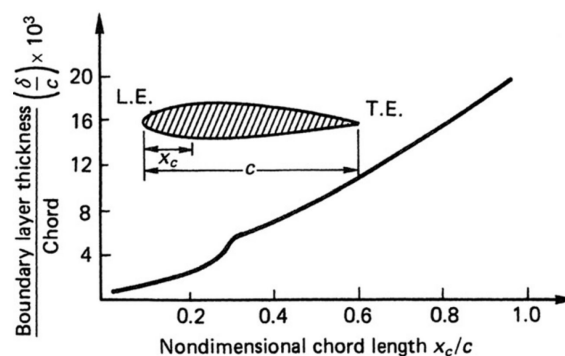


Figure 1-4: Typical growth of boundary layer thickness over an airfoil section [3]

For a general airfoil, the development of the boundary layer commences from its leading edge, or from the forward stagnation point, to be more specific. The flow around the section is

normally laminar in the early stages of the development of the boundary layer. The flow undergoes transition to a fully turbulent state after a certain distance. The location at which the transition occurs is a variable which is influenced by the flow velocities and the surface texture of the airfoil. The location on the airfoil at which the transition occurs from the laminar to turbulent flow is of considerable importance to the boundary layer growth. Experimental results, shown in Figure 1-4, illustrate the typical growth of a boundary layer over a symmetrical airfoil. The boundary layer thickness is found to increase rapidly between $0.25c$ — $0.3c$. This rapid growth is common in the presence of a streamwise adverse pressure gradient and is associated with the transition from laminar to turbulent flow.

The previous works of researchers have established that the process of boundary layer transition can be subdivided into numerous stages for a quiet boundary layer flow over a smooth surface. On moving downstream from the laminar flow present in proximity of the leading edge, two-dimensional unstable series of Tollmien-Schlichting waves appear, which then generate three-dimensional unstable waves and hairpin eddies. In regions of flow where the localized shear is high, vortex breakdown occurs, following which the breakdown of cascading vortices into fully three-dimensional flow fluctuations becomes apparent. So-called turbulent spots appear at these locally intense fluctuations, which later merge into a fully turbulent flow.

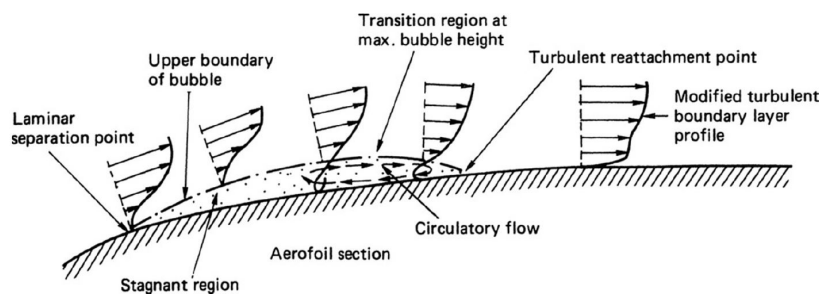


Figure 1-5: Laminar separation bubble [3]

Flow separation is a phenomenon which can occur either in the laminar or turbulent regimes. The curvature of the upper surface of the airfoil may be sufficient to trigger laminar separation in the case of laminar flow and under certain conditions, the separated laminar flow can undergo transition to a turbulent flow which is characterized by the rapid increase in the boundary layer thickness. The lower edge of the shear layer may contact the surface of the airfoil and reattach as a turbulent boundary layer, as illustrated in Figure 1-5. As a result of this, a separation bubble is formed and, depending on its size, this separation bubble, will have a greater or lesser effect on the pressure distribution over the airfoil. This separation bubble increases the drag of the airfoil and is referred to by many as bubble drag [20]. The separation bubble is characterized into two kinds, namely short and long.

Owen et al. [21] proposed a criterion that, if the Reynolds number Re_δ based on the displacement thickness of the boundary layer is greater than 550, a short bubble of the order of 1% of the chord is generated and its effect on the pressure distribution is negligible. As the short bubble breaks down, the flow separates completely from the airfoil surface without reattachment, and stall occurs, resulting in abrupt loss of lift and increase of drag. For

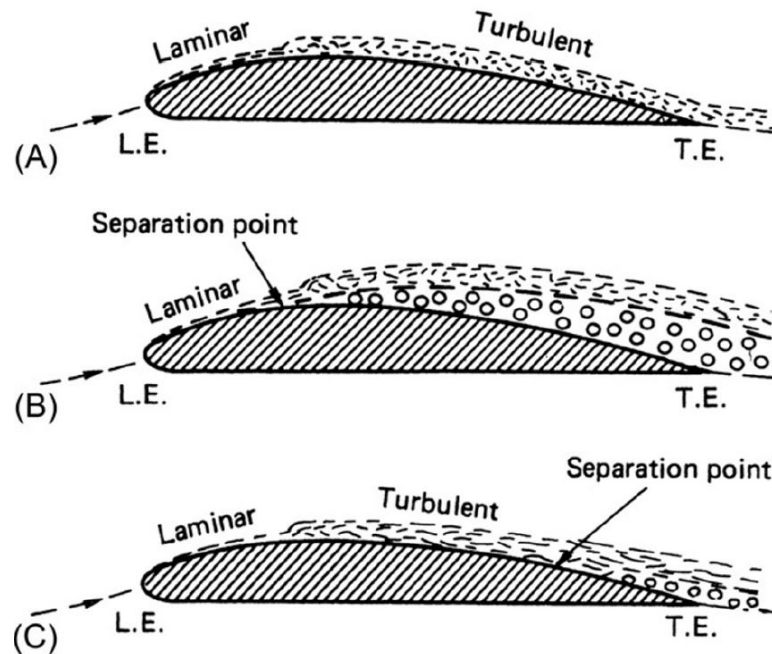


Figure 1-6: Illustration of flow regimes over the suction side of an airfoil: (a) fully attached laminar followed by turbulent boundary layer flow over the suction side; (b) laminar, leading edge separation without reattachment of flow over the suction side; (c) laminar followed by turbulent boundary layer with separation near the trailing edge. [3]

values of $Re_\delta < 440$, a long bubble ranging from a few percent of the chord to almost the entire chord length is generated. When the long bubble breaks down, it does not lead to a complete separation of the flow. Instead, the separated flow passes over the airfoil surface and reattaches further downstream and, eventually, may reattach to the trailing edge of the airfoil. The pressure distribution changes with the long bubble, but the discontinuity in lift is minimal [22].

The three different flow regimes that are possible for a flow around an airfoil are illustrated in Figure 1-6. Figure 1-6(a) illustrates a fully attached flow which comprises a laminar and a turbulent part. A laminar separation scenario without reattachment is shown in Figure 1-6(b). Figure 1-6(c) illustrates a scenario similar to Figure 1-6(a), but with a turbulent separation near the trailing edge[3].

1-2-4 Experimental investigations on wings in ground effect

Although this study is mainly focused on numerical simulations, it is vital that we investigate the experimental results from the testing of the front wings in wind tunnels. In order to validate the CFD results from the simulations, the experimental results are essential. Hence, the experimental literature on the airfoils with ground effect was reviewed, and below we present the summary of the review.

As discussed earlier in the section 1-2-2, the phenomenon of ground effect becomes more significant when the wing is in proximity to the ground. Ground clearance was found to

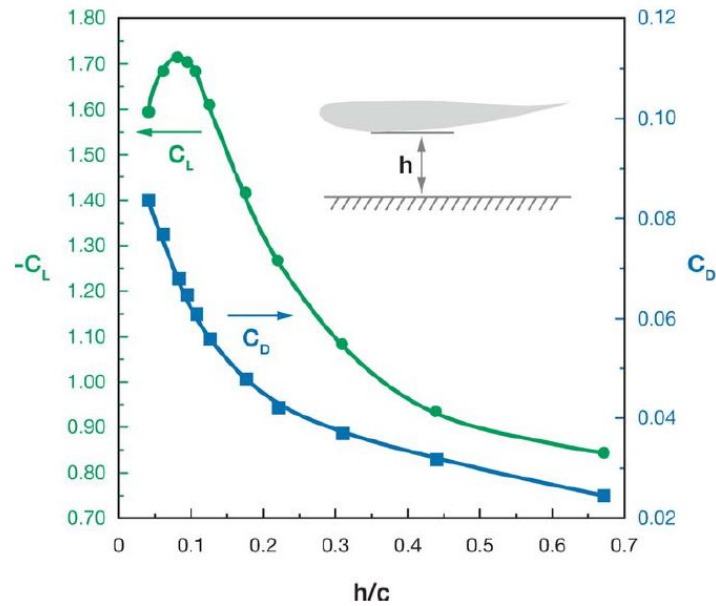


Figure 1-7: Downforce and drag coefficient versus ground clearance for an inverted LS(1)-0413 airfoil [4]. [$\alpha = 1^\circ$, $Re = 2 \times 10^6$, moving ground plane]

be the one of the significant factors that affected the ground effect phenomenon. Figure 2.7 shows the relation between the aerodynamic forces and ground clearances obtained from the three-dimensional experimental investigations carried out by Zerihan et al. [23]. It can be observed from the figure that the downforce keeps increasing until the ground clearance reduces to a critical value. As the ground clearance is reduced beyond this critical value, the downforce decreases. From the Figure 1-7, it can be seen that the critical value of ground clearance is $0.1c$ for the LS(1)-0413 inverted airfoil with an angle of incidence 1° . This is called the force reduction phenomenon. From the Figure 1-7, it can also be observed that drag force also increases as the ground clearance is reduced. Zerihan et al. [24] extended this study for a wing with a two-element airfoil, and it demonstrated the same trends as a single element behavior.

A single element GA (W)-1 wing was tested by Knowles et al. [25] in a wind tunnel with a moving belt that simulated the moving ground. For varying incidences with the suction side of the wing located at a range of heights from $1c$ down to $0.12c$ from the ground, the forces were measured. The tests demonstrated that as the ground clearance was reduced, the amount of downforce generated increased and the stall angle was reduced. The tests also demonstrated an increase in the drag force.

A series of experiments on both single and multi element wings by idealizing them as two-dimensional were presented by Razenback et al. [26, 27, 28]. Detailed measurements were carried out for a stationary NACA 0015 and NACA 4412 single element airfoil in ground effect in a fixed ground wind tunnel at a chord Reynolds number of 1.5 million. A reduction in downforce was observed when the suction surface was in proximity to the ground. This force reduction phenomenon was attributed to the merging of boundary layers of the ground plane and airfoil near the trailing edge. For the cambered airfoil, such as the multi-element wings, the force reduction phenomenon occurred at a ground clearance much higher than that

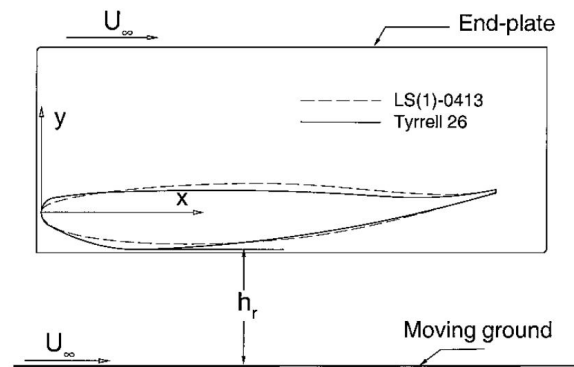


Figure 1-8: Side view of Tyrrell 26 wing model with endplates at ride height h_r [5]. The Tyrrell wing profile (indicated by the solid line) is developed from the LS(1)-0413 MOD wing profile (indicated by the dashes). The rectangular plates attached to the wing at the sides are referred to as endplates.

of the symmetric airfoil. Measurements were also carried out in a fixed ground wind tunnel for a NACA 63₂ – 215 Mod B section with a 30% slotted flap for a two-element model. The results demonstrated that the force reduction phenomenon occurred at a ground clearance less than approximately 22% of the front wing chord length.

Jasinski et al. [29] carried out investigations on the three-dimensional UIUC700 double-element airfoil in a low speed wind tunnel. The results obtained from the investigation revealed that the significance of Reynolds number effects were minimal on the lift and drag forces, with a variation of 3 – 4% observed in the lift and drag forces over the range of Reynolds numbers $0.7 – 1.3 \times 10^6$. On changing the flap deflection with 10° , an average increase in C_L of 0.5 was observed, while the drag coefficient was largely unaffected. The role of the endplate design on the lift and drag coefficients was also investigated. The results demonstrated an increase in lift coefficient and a significant reduction in drag coefficient on increasing the endplate area.

Experimental investigations were carried by J.Zerihan [5] on the front wing in ground effect for a range of Reynolds numbers $4.3 – 4.62 \times 10^5$. An 80% scale of the main element of the 1998 Tyrrell 026 F1 car front wing was used. A wing span of 1100 mm, a chord length of 223.4 mm and an aspect ratio of 4.92 was used. For carrying out the experiments, generic endplates were used, as seen in Figure 1-8. The investigations revealed that the wing generated different levels of downforce with varying ride heights. Downforce enhancements were seen at moderate and large ride heights. At a certain low ride height, a maximum downforce was seen. A force reduction was observed in proximity to the ground on reducing the ride height further. Separation of the boundary layer occurred near the trailing edge of the suction surface at a moderate ground height, as seen in Figure 1-9(a). From Figure 1-9(b) and Figure 1-9(c), it can be seen that, as the wing is brought closer to the ground, the region of separated flow increases in size. For a ground clearance of $0.224c$, the flow was found to separate on the suction side of the wing at $x/c \sim 0.9$ owing to the streamwise adverse pressure gradient. As the ground clearance was lowered further, the separation point was found to move upstream.

No evidence of the downforce reduction phenomenon due to merging of boundary layers of the ground plane and wing was found. The peak downforce occurred at a certain ground clearance at which all the pressure contributions to the force, when added, were maximum.

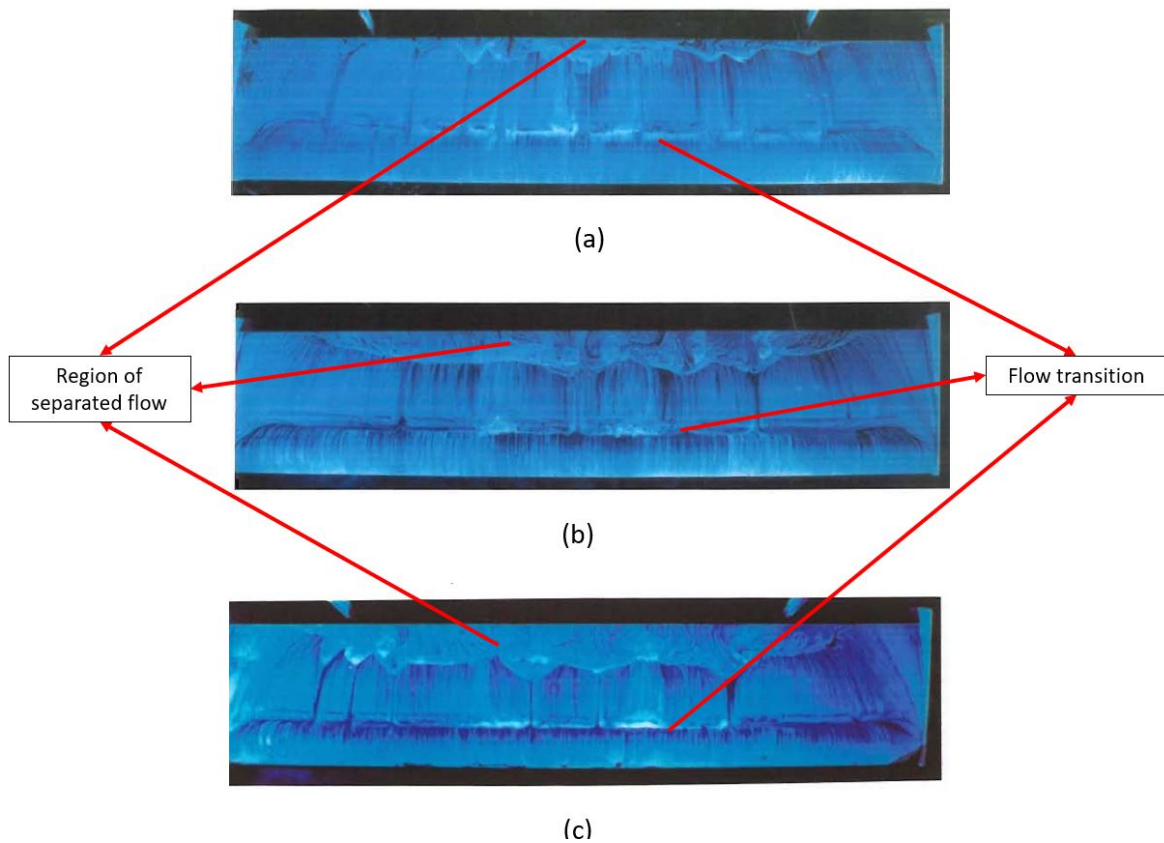


Figure 1-9: Oil flow visualization on suction surface, leading edge lowermost: (a) $h_r/c = 0.134$, (b) $h_r/c = 0.090$, (c) $h_r/c = 0.067$ [5]. The direction of the flow is from bottom to top. At $x/c \sim 0.3$, transition through means of the short reattachment bubble is observed for all three ride heights. For the ride height $h/c = 0.134$, a small region of separated flow can be observed at the central portion of the suction side of the wing at the trailing edge. For the ride height $h/c = 0.09$, an increase in the region of separated flow is observed. On reducing the ride height further, at $h/c = 0.067$, a further increase in the region of separated flow is observed.

As the ground clearance was reduced further, there is a drop in the pressures over the entire pressure surface. This results in a reduction in downforce. Also, on the suction side, the pressures reduce over the range of $x/c = 0.1 - 0.5$ (greater downforce), while on the other half they increase (less downforce). As a result, a single feature is not responsible for the maximum downforce, it is attributed to a summation of the pressures. The boundary layer separation at small ground clearances had a more significant influence on the reduction in performance. The drop in pressures over the pressure surface is also a factor.

J. Zerihan [5] extended his experimental investigations on the single element wing by varying the angle of incidence in the range of $\alpha = -3^\circ$ to $+9^\circ$. The investigations revealed that an increase in the angle of incidence of the wing resulted in a higher value of the maximum downforce as indicated in Figure 1-10, and a lower gradient of the downforce with height curve, in the force enhancement region of the curve. On increasing the angle of incidence, it was observed that the flow separation and loss of downforce occurred at a higher value of ground clearance than for the low angle of incidence case.

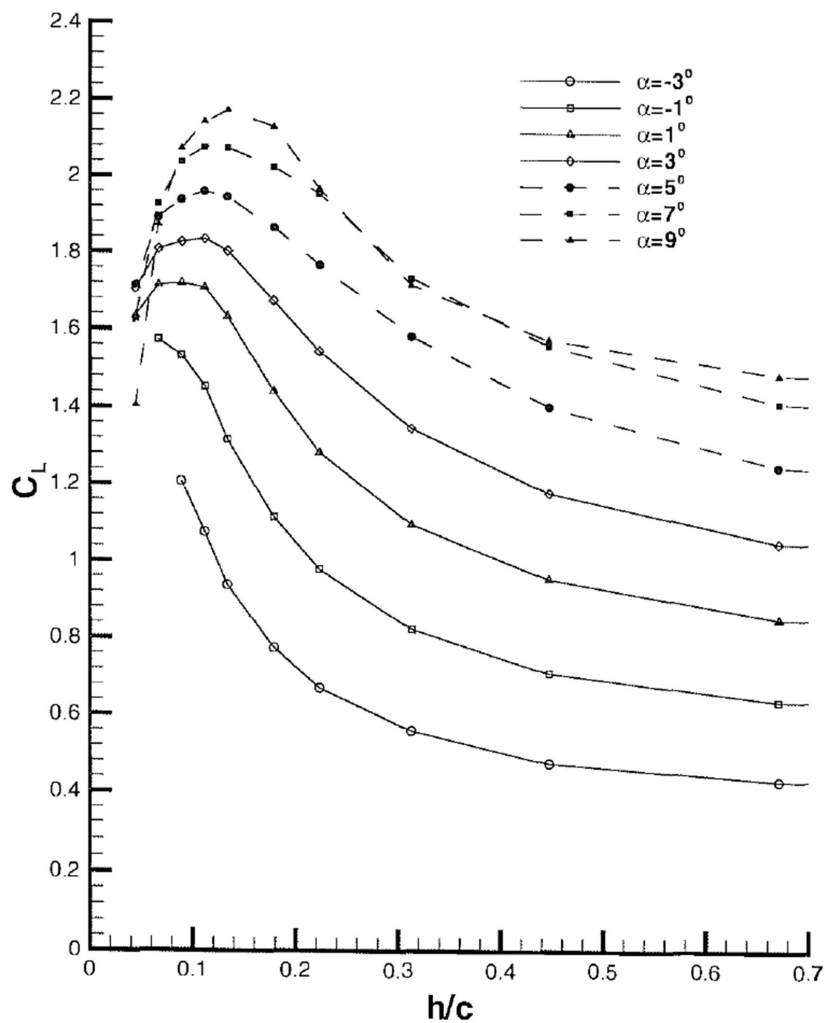


Figure 1-10: Downforce at varying incidences as a function of ride height h_r [5]. A greater value of the maximum downforce is observed on increasing the angle of incidence, and a lower gradient for the downforce with height curve is observed. Furthermore, the ground clearance at which maximum ground clearance is generated increases on increasing the angle of incidence, since the flow separation and downforce loss occur at a higher value of ground clearance than for the low angle of incidence case.

In the case of 3D wings that are installed on race cars, tip vortices are generated, which are absent in the case of a 2D model. These vortices, shown in Figure 1-11, are a result of the flow separation and pressure differences between the suction side and the pressure side of the wing. The experiment demonstrated that the tip vortex resulted in changes in aerodynamic force behavior in ground effect [6]. The presence of the tip vortex played a role in the downforce enhancement process. The tip vortex was found to induce an up-wash on the wing, resulting in an effective reduction in the angle of incidence of the wing and hence smaller extents of separation near the wing tip. As the wing was lowered to the ground, the vortex broke down, which led to a slow-down in force enhancement.

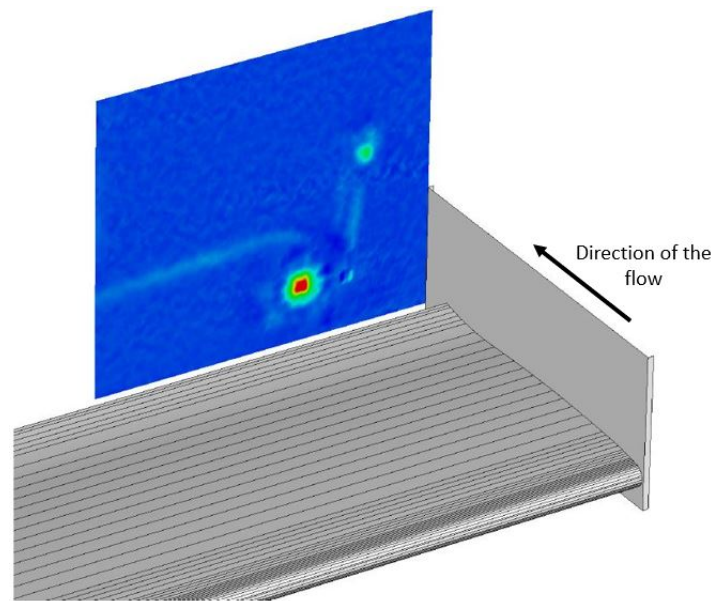


Figure 1-11: An illustration of the vortices generated for the Tyrrell 26 wing [6]. The contour in the image reveals the streamwise vorticity component, Ω_x .

1-2-5 CFD investigations on wings in ground effect

Since this study is focused on the numerical simulations of the front wing of a race car in ground effect subjected to translational accelerating motion, the literature on the CFD investigations of wings in ground effect was reviewed and a summary of this review is presented below.

Zerihan et al. [7] performed a computational study in order to model the flow around an inverted 2D airfoil in ground effect. Solutions of RANS equations with a turbulence model by Spalart-Allmaras(SA) [30] and the SST $k-\omega$ model [31] were used. The CFL3D solver was used with an implicit upwind code. CFL3D is a structured-grid, cell-centered, upwind-biased, RANS code. The results were then compared to experimentally measured surface pressures and LDA results taken at the center of the wing in ground effect. The results displayed good qualitative trends for the aerodynamic performances using the SA turbulence model when surface pressures were compared at different ground clearances. The wake region was predicted reasonably well in the region near the trailing edge. The wake predicted further downstream was found to be thicker than in experiments with reduced velocities, as shown by the comparison of experimental and computational wake surveys in Figure 1-12. The boundary layer on the ground was also predicted well using the SA model, but was significantly thicker when the SST $k-\omega$ model was used. A more detailed discussion on these turbulence models is performed in the Section 2-3.

Mahon et al. [32] investigated the pressure and wake of a 2D inverted cambered airfoil in ground effect for a chord Reynolds number of 1.5 million. The airfoil used in the investigation was a derivative of the LS(1)-0413 MOD profile. A multi-block hybrid grid design containing both structured and unstructured blocks was used. Six different turbulence models were used: the one-equation SA model[30], the standard $k-\epsilon$ model [33], the standard $k-\omega$ model [34], the

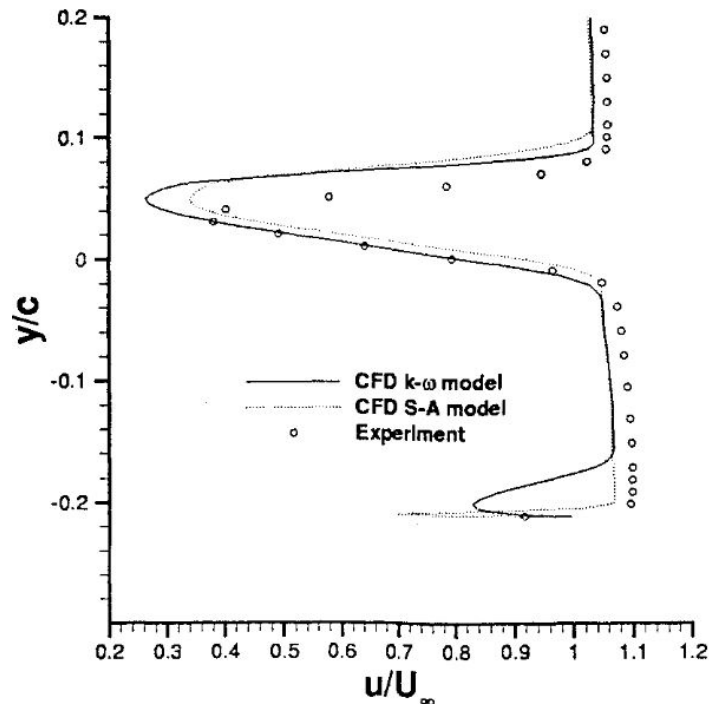


Figure 1-12: Comparison of experimental and computational wake surveys at $x/c = 1.2$ for $h/c = 0.134$ [7]. The velocities outside the wake region returned by the CFD models are lower than that observed in the experiment. The thickness of the wake is captured by CFD is slightly thicker on comparing with the experimental results.

$k-\omega$ SST model [31], the $k-\epsilon$ RNG model [35] and the Realizable $k-\epsilon$ model [36]. Enhanced wall treatment was employed for the $k-\epsilon$ model and its corresponding variants. The ability of the turbulence model to capture major physical features associated with the flow such as surface pressure distribution, separation, level of downforce, and wake for varying ground clearances was investigated. The $k-\omega$ SST model and the realizable $k-\epsilon$ model were found to offer good overall simulations, with $k-\omega$ SST performing better for the surface pressure and the Realizable $k-\epsilon$ offering a better wake prediction. At lower ride heights, the surface pressures, wake flow field, and region of separation on the suction surface of the airfoil were all modelled accurately.

Vogt et al. [8] carried out a 2D CFD investigation on the highly cambered Tyrrell airfoil, in both its uninverted and inverted configurations, in order to gain better insights into the ground effect phenomenon. Solution was obtained by solving the steady state two-dimensional RANS equations. A structured grid was used. For the computations, a chord Reynolds number of 1.5×10^6 was employed. The predictive capabilities of the Reynolds Stress turbulence Model (RSM) [37], standard $k-\epsilon$, $k-\epsilon$ RNG and realizable $k-\epsilon$ models were investigated for their ability to simulate the flow around these highly cambered airfoils. The RSM model produced an excellent, and superior match to the experimental data of Mahon et al. [32], both in terms of pressure coefficient C_p plots and near field velocity deficit wake readings at $x/c = 1.2$. The realizable $k-\epsilon$ model performed just as well as the RSM model in simulating the wake flow, while the other models returned poorer predictions for the wake. The RSM

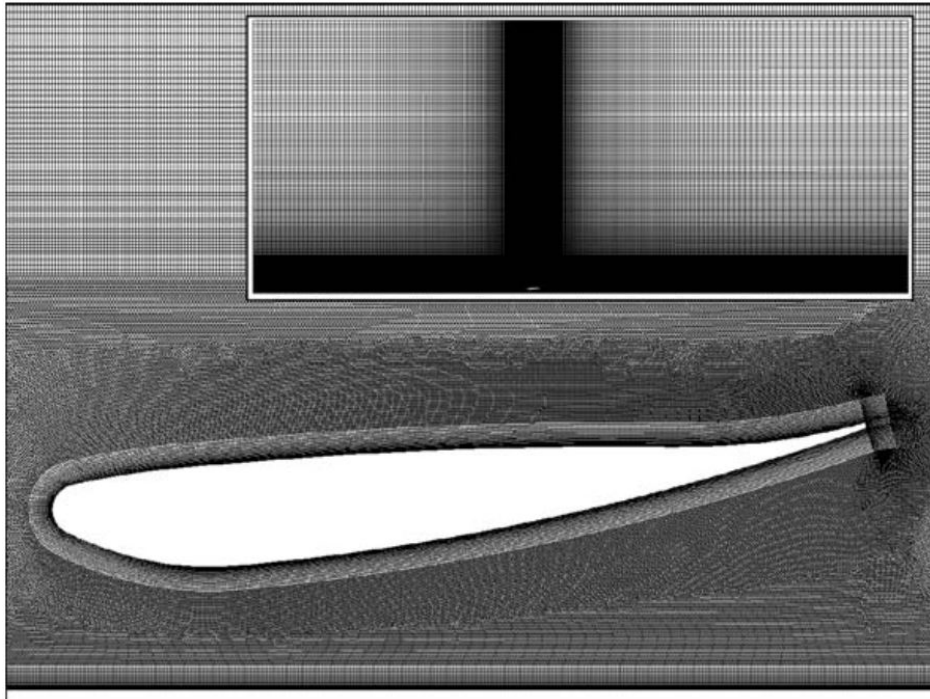


Figure 1-13: Mesh structure about inverted Tyrrell airfoil; inset - entire domain mesh [8]

and realizable $k-\epsilon$ models were found capable of predicting the flow separation at the trailing edge on the suction side of the airfoil.

1-2-6 Vortical Structures

Swirling flows are one of the phenomena that have been observed in multiple applications over the years. An evident example of this are naturally occurring hurricanes, tornadoes, and typhoons. Figure 1-14 shows hurricane Katrina as viewed from a satellite, an illustration of a 'naturally occurring vortex'.

Vortices are commonly present in the field of aerodynamics, where knowledge of their behavior is of utmost importance. Vortices are a common feature in our study and play a vital role. Hence, we will devote some discussion to vortices.

1-2-6-1 Definition of a Vortex

In spite of the considerable amount of research that has been poured into this topic, the question as to what constitutes a vortex in complex flows has long been a source of contention to researchers.

Over the past years, a lot of definitions have been proposed. A majority of these definitions refer to the attributes of a vortex, such as the region of pressure minimum in the core, closed or spiraling streamlines or a threshold level of vorticity [38]. Green [39], in his discussions, puts forward a non-rigorous definition—"a fluid vortex is a region of concentrated vorticity".



Figure 1-14: Hurricane Katrina as viewed from a satellite: An example of a naturally occurring vortex [9]

In spite of this statement having several deficiencies, it does broadly describe what is seen physically. Once the presence of a valid vortex is agreed upon, the more unsophisticated definitions of the threshold vorticity or closed streamlines are more suitable.

1-2-6-2 Vortex Formation

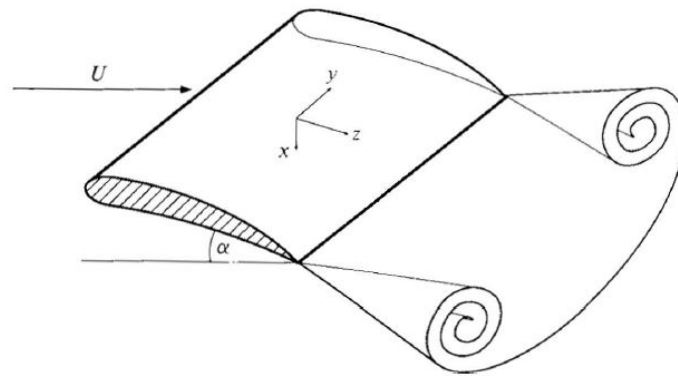
As discussed in Section 1-2-6-1, a vortex can be perceived as a zone of concentrated vorticity. Vorticity is a vital property of the flow necessary for the vortex generation.

Mathematically, the vorticity is defined as the curl of the velocity vector field and, physically, is related to the angular velocity in the flow [11]. The vorticity is generated as a result of flow advancing over a surface in a favorable pressure gradient (i.e., $\frac{\partial P}{\partial x} < 0$). The viscous forces acting in the vicinity of the surface play a vital role in the generation of vorticity [39] and as the flow undergoes separation from the surface in the presence of adverse pressure gradient (i.e., $\frac{\partial P}{\partial x} > 0$), the vorticity which is initially generated in the boundary layer is transported away from the surface. In his works, Delery [40] suggests that vortices can be interpreted as the structures which arise due to the rolling up of the separation surface. The formation mechanisms of a trailing wing-tip vortex system are discussed in the upcoming section, considering a rectangular planform wing as an example.

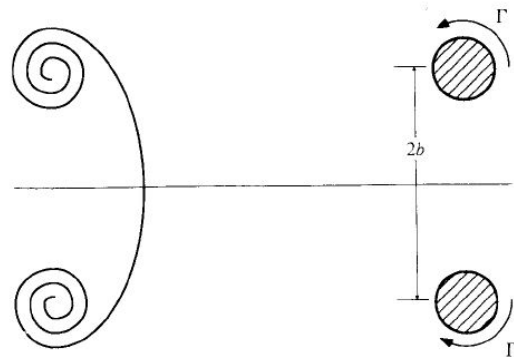
1-2-6-3 Tip Vortex Formation Mechanism: Rectangular Planform Wing

In his discussions, for a finite lifting wing, Green [41] states that as a lifting surface terminates in a fluid, tip vortices are generated. The continuous vortex sheet shed is a result of the streamwise vorticity contained within the tip vortex, which was generated on the lifting surface [42].

According to inviscid theory, a vortex sheet which is generated on the finite lifting wing will roll up as a result of its own induced velocity, as shown by the illustration in Figure 1-15(a). In the course of the roll-up process, the spirals narrow continuously as the distance between the



(a) Vortex sheet roll-up



(b) Intermediate and asymptotic stages of vortex sheet roll-up

Figure 1-15: Roll-up of an inviscid vortex sheet into two trailing vortices of equal strength [10]

neighboring turns reduce [43]. As a result, the vortex sheet between the two spirals undergoes continuous thinning as this vortex sheet is stretched. As a result of this roll-up process, two discrete wing tip vortices are generated, as illustrated by Figure 1-15(b). In his discussions, Green [41] states that, the roll-up process is reasonably quick, and occurs within 2-3 chords downstream of the trailing edge. When there is minimal change in the tangential velocity and the circulation of the vortex with the downstream distance, the roll-up process is deemed complete.

A more intuitive reasoning for the generation of wing tip vortex was put forward by Batchelor [44] and Anderson [11]. Their explanation for the formation of a trailing vortex system on a finite wing is based on the presence of pressure differences at the wing tip, which arise due to the lifting surface. As a result of the differences in the curvature of the airfoil cross-section, a suction, and pressure surface is created [44]. As the wing is finite, the two surfaces must meet at some point, and this occurs at the wing-tip. The pressure difference at the wing tip results in a tendency for the flow to accelerate circularly, curling the flow about the wing-tip [44, 11]. Figure 1-16 exhibits this behavior for a conventional positive lift producing wing. In the instance of a negative lift producing wing, like the ones found on a race car, the wing is inverted, and the suction surface is on the lower side.

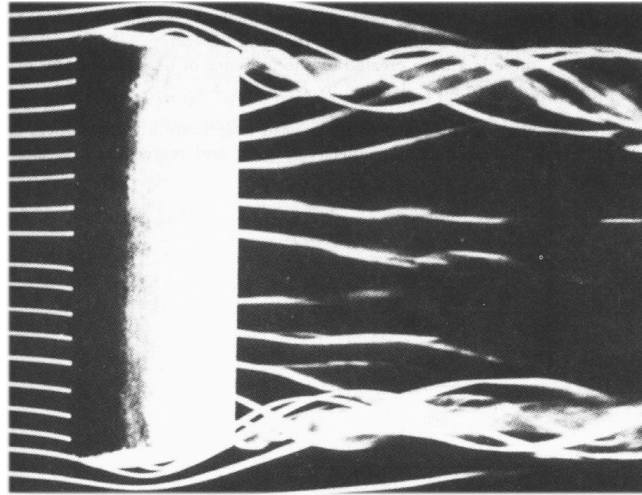


Figure 1-16: Wing tip vortices shed from a rectangular planform wing, made visible by smoke filaments [11]

Either of the above discussed reasonings is sufficient to describe the system of trailing vortices shed from the wing-tip of a rectangular planform wing as those seen experimentally in Figure 1-16.

1-2-6-4 Vortical Structures: Inverted airfoil with endplates

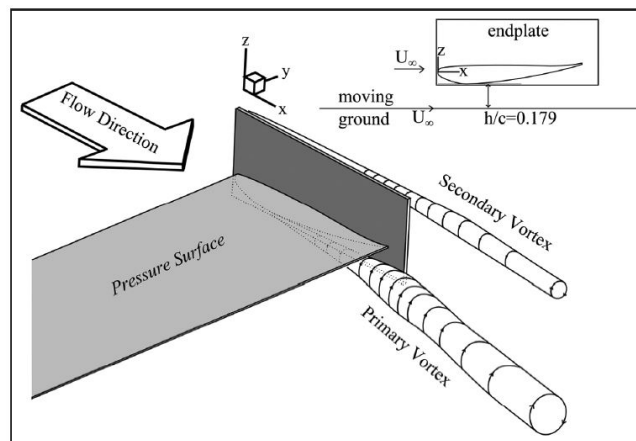


Figure 1-17: Primary and secondary vortices' location in the straight line scenario [12]

Keogh et al. [12] performed CFD investigations on the inverted Terrell wing with endplates. The flow in proximity of the endplates was characterized by primary and secondary vortices. As illustrated in the Figure 1-17, the primary vortex is formed inside the endplate, on the suction side, as a result of the pressure difference between the two sides of the endplate on the suction side of the inverted airfoil. The secondary vortex, formed outside the upper edge of the endplate, is generated due to the increased pressure inside the endplate over the pressure side. As the pressure difference present between the two sides of the endplate on the pressure

side is smaller than the one on the suction side, the secondary vortex produced on the outside edge of the upper edge of the endplate is weaker than the primary vortex. These vortical structures are vital in practical applications, since they travel downstream and interact with the car body and rear wings.

1-2-7 Accelerating Flows

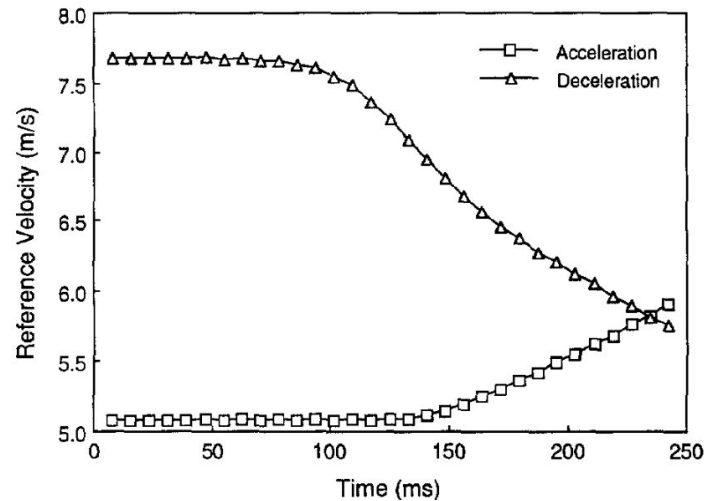


Figure 1-18: The reference velocity average transient responses determined from 490 transients [13]

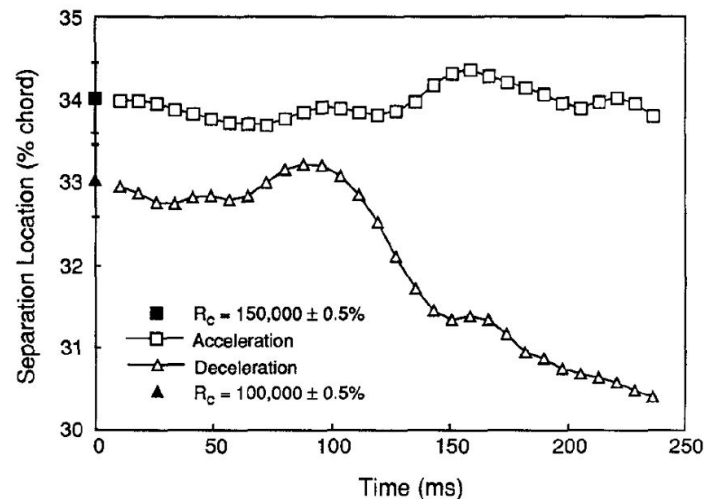


Figure 1-19: The separation chord position responses to the accelerating and decelerating transients [13]. For the accelerating flow, the location of the separation point moves slightly downstream when compared to its steady state location (at $Re_c = 150000$). For the decelerating flow, the location of the separation point moves upstream when compared to its steady state location (at $Re_c = 100000$).

Ellsworth et al. [13] experimentally investigated the effects of an accelerating free stream from

a non-zero velocity on the transitional separation bubble characteristics. The response of the boundary layer velocity profile was determined using hot-wire anemometry at selected chord wise locations on a Wortmann FX 63-137 airfoil at an angle of attack of 7° . The acceleration and deceleration effects were investigated for a chord Reynolds numbers 1.0×10^5 and, 1.5×10^5 respectively. The velocity profiles with which the flow is accelerated and decelerated in the experiments is shown in the Figure 1-18. The experimental results revealed that the separation bubble position shifted downstream in acceleration and shifted upstream in deceleration when compared to its steady state location. This is demonstrated by Figure 1-19. The location of the separation point was more affected in the case of decelerating flow when compared to the accelerating flow.

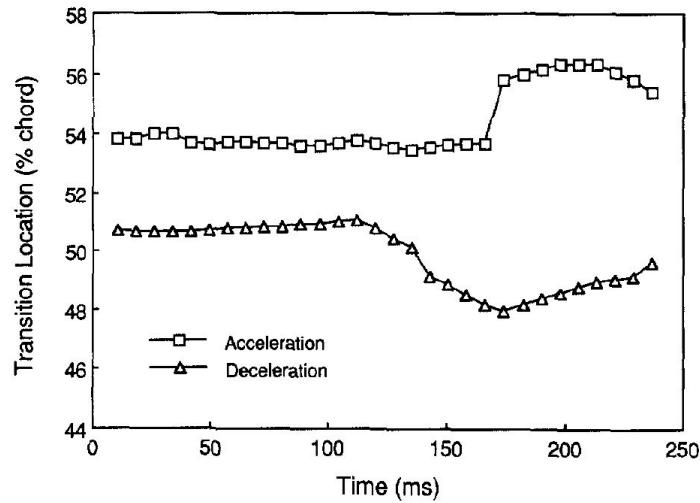


Figure 1-20: The transition chord position responses to accelerating and decelerating transients [13]. For the accelerating flow, the location of the transition point moves downstream when compared to its location at steady state. For the decelerating flow, the location of the transition point moves upstream when compared to its steady state location.

The Figure 1-20 reveals the effects of the acceleration and deceleration on the location of the transition point. The transition point was found to move downstream in acceleration when compared to its steady state location, while in the case of deceleration, the transition point shifted upstream when compared to its steady state location.

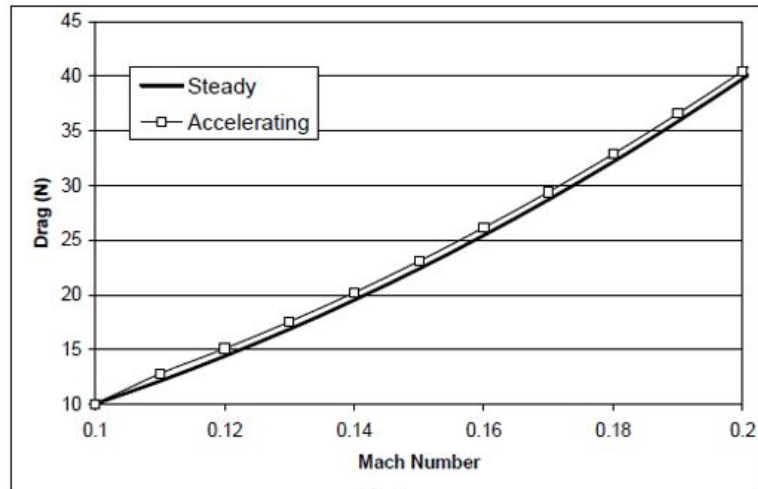
Freytmuth et al. [45] carried out experiments to visualize the accelerating flow around an airfoil. A characteristic time t_c was defined as the typical time for the air to cross a chord of length c from rest at a constant acceleration a . The experiments were carried out for an acceleration Reynolds number, $Re_a = 5300$. The time for which the acceleration was sustained was much larger than t_c .

$$t_c = \left(\frac{c}{a}\right)^{1/2} \quad (1-1)$$

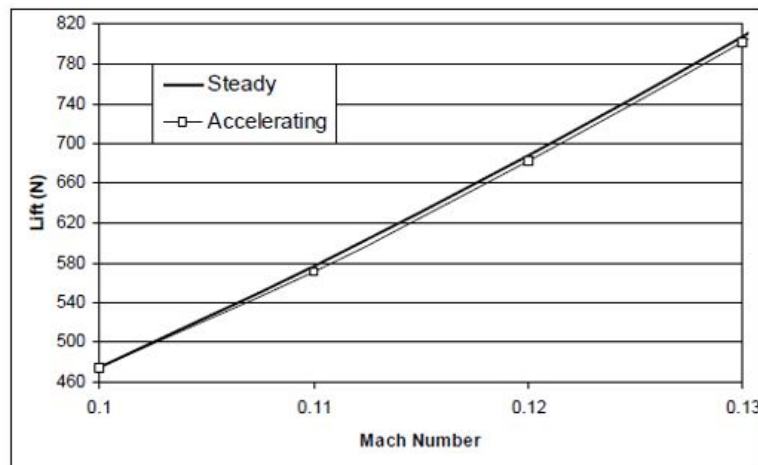
The characteristic velocity v_c was defined using the characteristic time, t_c .

$$v_c = \sqrt{ca} \quad (1-2)$$

The acceleration Reynolds number, Re_a is defined using the characteristic velocity v_c .



(a)



(b)

Figure 1-21: NACA 2412 airfoil (a) Subsonic drag at steady and +0.8845g, (b) Subsonic lift at steady and +0.8845g [14]

$$Re_a = \frac{\rho v_c c}{\mu} = \frac{\rho c \sqrt{ca}}{\mu} \quad (1-3)$$

Roohani [14] numerically investigated the influence of acceleration on two-dimensional objects at both sonic and subsonic speeds. The results for the subsonic flow over a NACA 2412 airfoil demonstrated a difference in body forces for the accelerating and decelerating scenarios, as shown in figure 2.32. A variation of $\pm 4^\circ$ in the stall angle of the airfoil was also observed. An acceleration of 0.8845g was employed on the NACA 2412 airfoil (typical acceleration range encountered in Formula One). The accelerating case was simulated for a range of Mach numbers varying from 0.1 – 0.2 (125-250 kmph). The results demonstrated that there was an increase in drag force generated and a decrease in lift force generated when the airfoil was subjected to acceleration, as shown in Figure 1-21. The handling and the fuel consumption of a race car can be affected noticeably if there is a similar percentage increase in the total

drag force. The traction and the handling of a car can be drastically affected if a similar percentage(1% of typically 6 kN ~ 60 N) reduction in the total aerodynamic downforce is present.

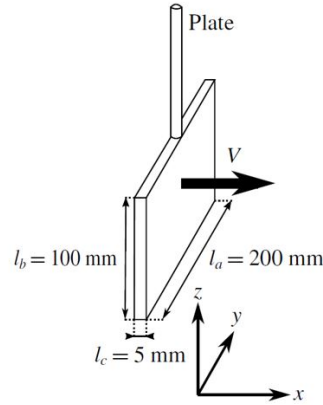


Figure 1-22: Dimensions and the orientation of the flat plate used for carrying out the experiment [15]. The flat plate immersed in the RowBot tank was accelerated in the x-direction to study the of acceleration on the drag force.

Experimental investigation was carried out on the drag force on an accelerating flat plate at the TU Delft Aero-& Hydrodynamics Laboratory by moving the plate through the water in RowBot tank for different immersion depths [15]. The dimensions of the flat plate used for this study are shown in the Figure 1-22. The velocity profile with which the flat plate is accelerated and the corresponding acceleration profile of the flat plate is shown in the Figure 1-23.

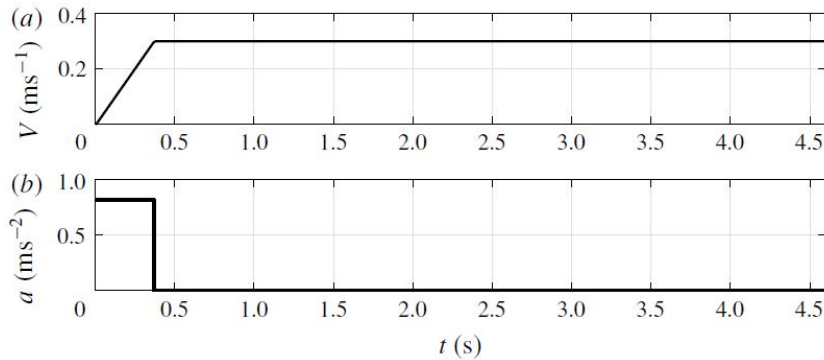


Figure 1-23: (a) Flat plate velocity and (b) Flat plate acceleration as a function of time t [15].

Generally, the steady state drag force on the flat plate is defined as,

$$F_x = \frac{1}{2} \rho V^2 C_D A \quad (1-4)$$

where ρ is the density of the fluid, V is steady state velocity, A is the frontal-area of the flat plate (area in the y - z plane in the Figure 1-22) and C_D is the drag coefficient corresponding to the flat plate. However, in the instance of an accelerating object in a fluid, the added mass

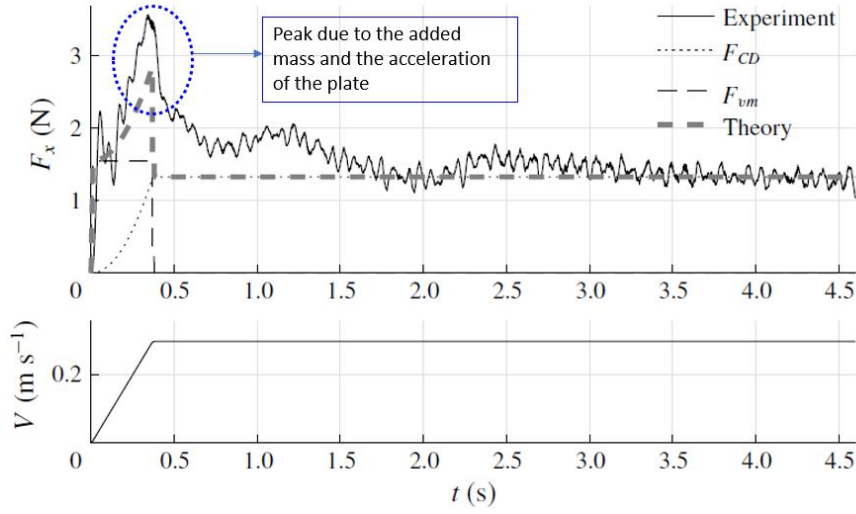


Figure 1-24: Drag force on the accelerating flat plate determined experimentally for an immersion depth $h = 100$ mm determined experimentally, along with the theoretical drag force and its components F_{CD} and F_{vm} using the Equation 1-5 [15].

effects must be incorporated into the definition of the drag force, as shown in the Equation 1-5.

$$F_x(t) = F_{CD}(t) + F_{vm}(t) = \underbrace{\frac{1}{2}\rho V(t)^2 C_D A}_{F_{CD}(t)} + \underbrace{\overbrace{(m_p + m_h)}^{m_v} a(t)}_{F_{vm}(t)} \quad (1-5)$$

where F_{CD} is the steady state drag force and F_{vm} is the virtual force as a result of the product of the virtual mass m_v and the acceleration of the flat plate $a(t)$. The virtual mass includes the mass of the plate m_p and the hydrodynamic mass m_h . For an arbitrary flat plate, Yu [46] provides an empirical correction for modelling the hydrodynamic mass m_h .

$$m_{h(Yu)} = \rho \left[0.788 \frac{l_a^2 l_b^2}{(l_a^2 + l_b^2)^{1/2}} + 0.0619 l_a l_b l_c^{1/2} \right] \quad (1-6)$$

The Figure 1-24 shows the experimentally measured drag force $F_x(t)$ for an immersion depth $h = 100$ mm, along with the theoretical drag force in the Equation 1-24. The time at which the peaks in the experimental and theoretical drag force coincide with the time at which the acceleration ends, i.e., $t = 0.36$ s. The theoretical drag force reveals a sharp drop as soon as the acceleration of the plate ends, since the term corresponding to the virtual force in the Equation 1-5 drops to zero. However, in the experiment, a more gradual decrease in the drag force after the peak at $t = 0.36$ s is observed.

1-2-8 Theoretical treatment of accelerating flows

In motorsports aerodynamics, the working fluid is air, which under the given operating conditions can be assumed to be incompressible (i.e. $\rho = \text{constant}$) with a constant viscosity (i.e. $\mu = \text{constant}$). The equations that govern the flow are given by the Navier-Stokes equations.

Continuity Equation:

$$\frac{\partial u}{\partial x} + \frac{\partial v}{\partial y} + \frac{\partial w}{\partial z} = 0 \quad (1-7)$$

Momentum Equations:

- x-component:

$$\rho \left(\frac{\partial u}{\partial t} + u \frac{\partial u}{\partial x} + v \frac{\partial u}{\partial y} + w \frac{\partial u}{\partial z} \right) = -\frac{\partial p}{\partial x} + \mu \left(\frac{\partial^2 u}{\partial x^2} + \frac{\partial^2 u}{\partial y^2} + \frac{\partial^2 u}{\partial z^2} \right) + \rho g_x \quad (1-8)$$

- y-component:

$$\rho \left(\frac{\partial v}{\partial t} + u \frac{\partial v}{\partial x} + v \frac{\partial v}{\partial y} + w \frac{\partial v}{\partial z} \right) = -\frac{\partial p}{\partial y} + \mu \left(\frac{\partial^2 v}{\partial x^2} + \frac{\partial^2 v}{\partial y^2} + \frac{\partial^2 v}{\partial z^2} \right) + \rho g_y \quad (1-9)$$

- z-component:

$$\rho \left(\frac{\partial w}{\partial t} + u \frac{\partial w}{\partial x} + v \frac{\partial w}{\partial y} + w \frac{\partial w}{\partial z} \right) = -\frac{\partial p}{\partial z} + \mu \left(\frac{\partial^2 w}{\partial x^2} + \frac{\partial^2 w}{\partial y^2} + \frac{\partial^2 w}{\partial z^2} \right) + \rho g_z \quad (1-10)$$

The coupled non-linear partial differential equations above are solved to obtain the pressure and velocity fields in the flow across space and time.

Numerically and theoretically, opting a frame of reference relative to which the airfoil is at rest when advantageous when the airfoil is accelerated in a fluid. The equations of motion must be modified for the moving reference frame.

The equations of motion in the non-inertial frame can be arrived at by using two different approaches. Batchelor et al. [44] uses the Lagrangian fluid parcel approach to derive the equations of motion in the non-inertial frame, while Kageyama et al. [47] adopts the Eulerian approach to derive the Navier-Stokes equations in the non-inertial frame. Although the Eulerian approach is more mathematically rigorous, it can be used for any vector field, even in cases where the fluid parcel concept is invalid. As this approach involves using Galilean and rotational transformations, the physical meaning of terms in this derivation is clearer.

Here, we go through the modified equation of motion that is obtained from the citations. In the non-inertial frame, the incompressible form of the Navier-Stokes equation for an arbitrary accelerating airfoil P in the Figure 1-25 involves six fictitious terms and is given by Equation 1-11. *Centrifugal* forces originate from the transformation of the convection terms in the Navier-Stokes equations, while the *Coriolis* forces originate from the transformation of both the transient and convection terms in the Navier-Stokes equations. *Translation* and the *unsteady motion* forces originate from the transformation of the transient component of the Navier-Stokes equations. *Magnus* force is the term that represents the interaction between the translating and rotating part of the flow.

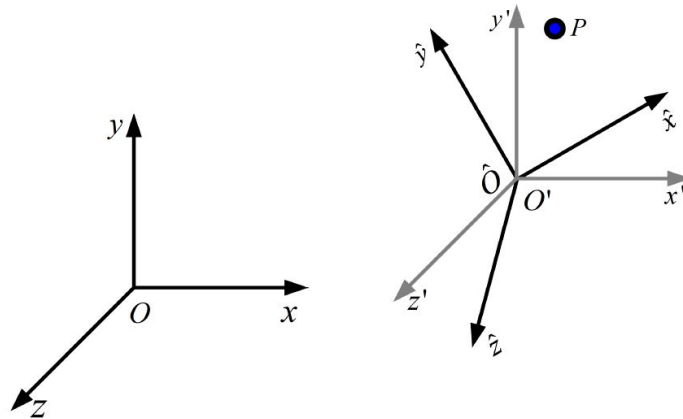


Figure 1-25: The *Frame O* is the inertial frame, which is stationary. *Frame O'* is the non-inertial frame which preserves the orientation. *Frame O'* accounts for relative translation motion between the inertial and the non-inertial frame. *Frame O-hat* is the non-inertial rotating frame which does not preserve the orientation. *Frame O-hat* accounts for the rotation between the inertial and non-inertial frame. P is the point mass (airfoil, in this instance)

$$\frac{\partial \hat{\mathbf{u}}}{\partial t} + (\hat{\mathbf{u}} \cdot \hat{\nabla}) \hat{\mathbf{u}} = -\hat{\nabla} \hat{\psi} + v \hat{\nabla}^2 \hat{\mathbf{u}} - \underbrace{\frac{\partial}{\partial t}(\mathbf{V}(t))}_{\text{Translation}} + \underbrace{\hat{\mathbf{x}} \wedge \boldsymbol{\Omega} + \hat{\mathbf{x}} \wedge \dot{\boldsymbol{\Omega}}}_{\text{Euler}} + \underbrace{2\hat{\mathbf{u}} \wedge \boldsymbol{\Omega}}_{\text{Coriolis}} - \underbrace{\hat{\mathbf{x}} \wedge \boldsymbol{\Omega} \wedge \boldsymbol{\Omega}}_{\text{Centrifugal}} + \underbrace{2\mathbf{V}(t) \wedge \boldsymbol{\Omega}}_{\text{Magnus}} \tag{1-11}$$

and,

$$\psi = \frac{p}{\rho} \tag{1-12}$$

In the case of the accelerating airfoil, only the unsteady translation is present and there is no rotation.

$$\begin{aligned} \hat{\mathbf{x}} &= 0 \\ \hat{\boldsymbol{\Omega}} &= 0 \\ \dot{\boldsymbol{\Omega}} &= 0 \end{aligned} \tag{1-13}$$

For the case of unsteady translation, the Equation 1-11 reduces to

$$\frac{\partial \hat{\mathbf{u}}}{\partial t} + (\hat{\mathbf{u}} \cdot \hat{\nabla}) \hat{\mathbf{u}} = -\hat{\nabla} \hat{\psi} + v \hat{\nabla}^2 \hat{\mathbf{u}} - \underbrace{\frac{\partial}{\partial t}(\mathbf{V}(t))}_{\text{Translation}} \tag{1-14}$$

1-3 Research Motivation, Questions & Goals

The research motivation leading up to this thesis is summarized below. Rob Smedley, the former head of vehicle performance at Williams Racing stated that *Where teams have problems is when their development or simulation environment – so CFD [Computational Fluid Dynamics] or wind tunnel – doesn't describe well what happens in reality (although in truth, no-one's wind tunnel correlates absolutely 100%)*. One of the reasons for this poor correlation could be arising from the fact that, in real life on track scenarios, the race cars undergo accelerating, decelerating or cornering motion which can have a different influence on the aerodynamics of a race car which is not accounted for in the wind tunnel and simulation environment where a steady constant flow is employed. This thesis aims at understanding the trends in aerodynamic forces and the flow structures in the wake region when a wing in ground effect is subjected to accelerating and decelerating flows. Also, experimental investigations on an accelerating flat plate at the Aero & Hydrodynamics Lab at TU Delft revealed a peak in the drag force response when the transition occurred from acceleration to a constant velocity.

The general outline of the approach that was followed during the course of the thesis is listed below:

1. Literature review on the aerodynamic behavior of the front wing of a race car subjected to acceleration, deceleration and cornering from a theoretical perspective and numerical methodologies to simulate them.
2. Designing a single element front wing based on the currently available wing profile and generating the grids for computation.
3. Performing 2-dimensional and 3-dimensional numerical simulations for the steady-state aerodynamics cases and validate the results with the existing experimental data.
4. Extending the steady-state constant velocity investigations to transient accelerating and decelerating cases to capture the trends in aerodynamic forces and flow structures.
5. Validating the CFD results for accelerating flows with the experimental data obtained from the Aero & Hydrodynamics Laboratory.

Based on the literature reviewed, the following research questions and goals are formulated.

- The thesis aims to verify whether the spike in the drag force that the wing in ground effect generates is a local effect which is a result of the velocity profile with which the flat plate is accelerated in the experiment, to determine the influence of acceleration on the drag force of a flat plate.
- The loss of the downforce in the inverted airfoils in proximity to the ground is primarily attributed to the flow separation on the suction side. The influence of accelerating and decelerating flows on the flow separation has not been investigated thoroughly. The thesis aims at understanding the trends in the flow separation points for accelerating and decelerating flows to explain the loss and gain of downforce/grip that race-car drivers experience when they accelerate or decelerate.

-
- The tip-vortices that are generated by the endplate significantly contribute to the downforce enhancement process. The thesis aims at studying the strengths of the tip-vortices for accelerating and decelerating flows past a wing in ground effect to explain the loss and gain of downforce/grip that race-car drivers experience when they accelerate or decelerate.
 - Performing a dimensionless number study for the acceleration and deceleration encountered, and investigating their influence on the aerodynamic performance of the wing.
 - The thesis aims at verifying whether the downforce generated by the wing in ground effect subjected to accelerating and decelerating flows is only dependent on the chord Reynolds number.

Numerical modelling

The flow past the front wing of a Formula One car is investigated numerically in this study using the commercially available Computational Fluid Dynamics(CFD) package ANSYS Fluent. ANSYS-Fluent 19.2 is employed to perform the CFD simulations on the cluster of the Process & Energy department, TU Delft. In this section, the steps involved in numerical modelling, namely: geometry, flow conditions, meshing and turbulence modelling are reviewed.

2-1 Geometry and Flow Scenarios

2-1-1 2-Dimensional Single Element Inverted Airfoil

The profile for the single element 2-dimensional inverted airfoil is based on the coordinates available for the main element of the 1998 Tyrrell 026 F1 car front wing. The coordinates used for generating the wing profile can be found in Table A-1 in the Appendix A. This results in a wing with a unit chord length and an angle of incidence 3.45° . The angle of incidence is defined as the angle between the wing chord and the longitudinal axis of the wing, i.e., the x-axis. For the 2-dimensional calculations, a unit span length is used for the wing, which results in a geometric aspect ratio of unity. The aspect ratio of the wing is defined as the ratio of the square of the span to the wing area.

Another 2-dimensional inverted airfoil with a chord length 223.4 mm is also generated with a unit span length. The results generated with this profile were then used for comparing with the 3-dimensional flow effects which are observed for the 3-dimesnional wing with endplates in section 2-1-2.

2-1-2 3-Dimensional Single Element Inverted Airfoil

For the 3-dimesional investigations, the same airfoil profile used in the above section 2-1-1 is used. However, in this instance, the same aspect ratio of the 4.92 which was found in the 1998

Tyrrell car is maintained. As a result, the coordinates in Appendix A need to be multiplied by a factor of $\frac{1117069}{5000000}$, which results in a chord length of 223.4 mm. The wing span corresponding to an aspect ratio of 4.92 is 1100 mm. Generic endplates of the same dimensions $250 \times 100 \times 4$ mm from the reviewed literature [5] are added to the inverted airfoil at the edges.

2-1-3 Flow Scenarios

In this section, the velocity profiles with which the wing is accelerated, and their corresponding acceleration profiles, are reviewed.

2-1-3-1 Case 1: Piecewise Linear Velocity Profile

A linear velocity similar to the one used for experiments on accelerating flat plates at the Aero & Hydrodynamics Lab [15] is generated. The velocity profile used to accelerate and decelerate the airfoil can be defined using the function below.

$$u(t) = \begin{cases} U_1, & t \leq 3.0s \\ at, & 3.0s < t \leq 4.2s \\ U_2, & t > 4.2s \end{cases} \quad (2-1)$$

The Figure 2-1 shows the velocity profile with which the airfoil is accelerated and decelerated, and the corresponding acceleration profiles.

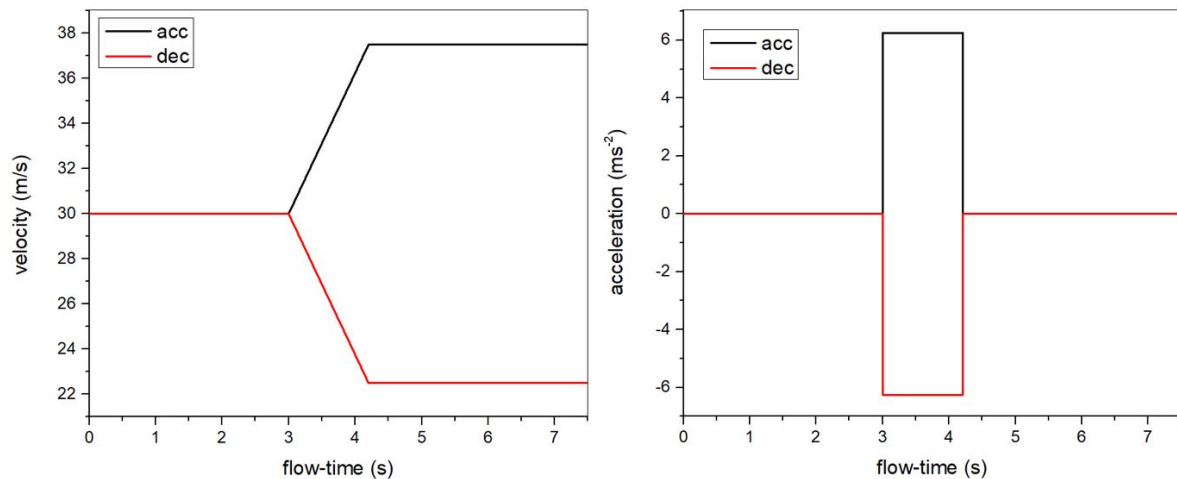


Figure 2-1: Piecewise linear velocity profile(s) with which the airfoil is accelerated (and decelerated), and the corresponding acceleration profile(s). The velocity profile used for accelerating (and decelerating) the airfoil is generated using the Equation 2-1

2-1-3-2 Case 2: Non-linear Velocity Profile

A non-linear velocity profile is generated for a smooth acceleration profile. This profile was generated to resemble the smooth accelerating and decelerating motions which a racecar

undergoes on the racetrack. The velocity profile was generated using the Fermi-Dirac function below.

$$u(t) = \frac{U_1 - U_2}{1 + e^{(t-t_0)/\Delta t}} + U_2 \quad (2-2)$$

The Figure 2-2 illustrates the non-linear velocity profiles used for accelerating (and decelerating) the airfoil, generated using the equation 2-2, and the corresponding acceleration profiles.

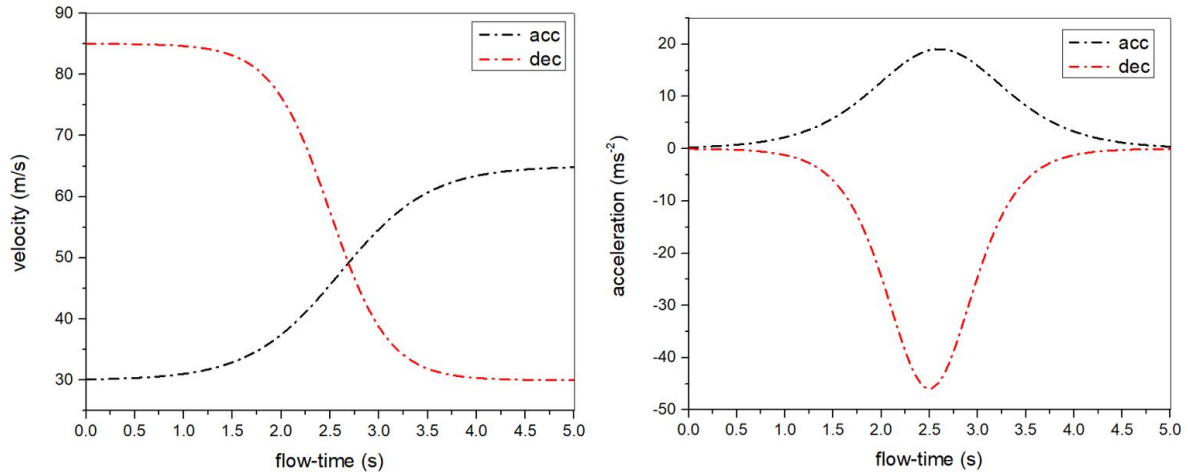


Figure 2-2: The non-linear velocity with which the airfoil is accelerated (and decelerated) and the corresponding acceleration profiles. The non-linear velocity profiles for accelerating the airfoil is generated using the Equation 2-2

2-2 Meshing

In CFD, in order to solve the flow governing equations numerically, we need to divide the computational domain into a number of elements/cells. In this study, the meshes are generated by using *ANSYS meshing module* and *pointwise (Gridgen)* meshing tool. Meshes are broadly classified into three types.

- **Structured mesh**
 1. Cells are topologically similar.
 2. Better convergence and less numerical diffusion.
 3. Difficult to set up for complex geometries and computationally expensive.
- **Unstructured mesh**
 1. Cells are not topologically similar.
 2. Risk of false numerical diffusion.
 3. Easier to generate for complex geometries.
- **Hybrid mesh**

1. Combination of structured and unstructured meshes.
2. Implementation usually as unstructured grid, or as multi-block grid.
3. Enable parts of complex geometries to be discretized with structured grids.

Previous research has employed all the above-mentioned types of grids. Zerihan et al. [7], Roohani et al. [14], Keogh et al. [48, 12] and Voght et al. [8] performed their numerical investigations on wings using structured grids while Qu et al. [49], Roberts et al. [50], Nara et al. [51] employed unstructured grids for their numerical investigations. Mahon et al. [32, 52] carried out numerical studies using hybrid meshes. In all the above cases, the authors were able to obtain satisfactory results for the aerodynamic forces and were able to capture the behavior of the wake.

2-3 Governing Equations & Turbulence Modelling

The Finite Volume Method(FVM) is employed by the ANSYS Fluent solver to solve the flow field around the front wing using discretized Navier-Stoke(NS) equations. The NS equations are the mathematical expressions which describe the fundamentals of the viscous Newtonian fluid flows. Although the set of equations correctly represent the physics of the flow, they fail to provide analytical solutions explicitly, except for simplified flow regimes. As a result, numerical methods are required for solving these set of equations. The incompressible variant of the NS equations is presented in Equations 2-3 and 2-4 as the low Mach numbers experienced by Formula One cars do not require compressible calculations.

$$\frac{\partial u_i}{\partial x_i} = 0 \quad (2-3)$$

$$\rho_f \left(\frac{\partial u_i}{\partial t} + \frac{u_j \partial u_i}{\partial x_j} \right) = -\frac{\partial p}{\partial x_i} + \mu \frac{\partial^2 u_i}{\partial x_j^2} - \rho_f \frac{\partial V(t)}{\partial t} \quad (2-4)$$

Direct Numerical Simulation(DNS)

DNS involves computing the solutions of the unsteady Navier-Stokes equation without any turbulence model, and is capable of resolving the domain at every spatial and temporal scale(i.e., from the Kolmogorov scale to the integral scale). The computational effort of DNS varies approximately with the third power of Reynolds number [53]. As a result of this, DNS is ruled out of scope for this research, as it is limited to simple geometries at low Reynolds numbers.

Large Eddy Simulation(LES)

Modelling must be employed to reduce the complexity of the problem and to reduce the computational requirements of DNS. NS equations are segregated into resolved and unresolved parts by Large Eddy Simulations(LES) which allows for the use of coarser grids as well. For simulating accurately, this must be carried out with care to capture the eddies which have large anisotropy and energy, while the smaller scales of isotropic turbulence are modelled.

Earth simulator in Japan was employed to perform one of the world's largest unsteady turbulence simulations of flow around a Formula One car using LES by Tsubokura et al. [54]. The commercial software Gridgen was employed to generate the unstructured computational grid. The computational domain size was $34.0\text{ m} \times 2.7\text{ m} \times 2.47\text{ m}$ and a total of 117,060,909 elements was used to fill in the entire computational domain. The results obtained from the simulation demonstrated that the lift coefficient predicted was only about 1% larger than that obtained from wind tunnel experiments. Although the disagreements between the drag coefficient predicted with the data from the wind tunnel experiments and the simulations are present, the differences were less than 10%.

Reynolds Averaged Navier Stokes(RANS) Turbulence Modelling

In CFD simulations, RANS turbulence modelling is computationally less intensive when compared to DNS and LES. Although this approach is efficient as a result of relaxation of grid spacing requirements, it requires more modelling of physics when compared to DNS and LES, which is a potential source for error.

In this approach, the variables (\mathbf{u}, p) in the NS Equations 2-3 and 2-4 are substituted by their mean $(\bar{\mathbf{u}}, \bar{p})$ and fluctuating values (\mathbf{u}', p') using Reynolds decomposition [55].

$$\mathbf{u} = \bar{\mathbf{u}} + \mathbf{u}' \quad (2-5)$$

$$p = \bar{p} + p' \quad (2-6)$$

The RANS equations are obtained as in the equations below.

$$\frac{\partial \bar{u}_i}{\partial x_i} = 0 \quad (2-7)$$

$$\frac{\partial \bar{u}_i}{\partial t} + \frac{\partial}{\partial x_j} (\bar{u}_j \bar{u}_i) = -\frac{1}{\rho} \frac{\partial \bar{p}}{\partial x_i} + \frac{\partial^2}{\partial x_j \partial x_j} (\nu \bar{u}_i) - \frac{\partial}{\partial x_j} (\overline{u'_j u'_i}) \quad (2-8)$$

This results in an additional stress term $(\overline{u'_j u'_i})$ in the governing equations. This is termed as the Reynolds stress tensor, which is represented in its expanded form as follows:

$$\overline{u'_j u'_i} = - \begin{pmatrix} \overline{u' u'} & \overline{u' v'} & \overline{u' w'} \\ \overline{v' u'} & \overline{v' v'} & \overline{v' w'} \\ \overline{w' u'} & \overline{w' v'} & \overline{w' w'} \end{pmatrix} \quad (2-9)$$

The Reynolds stress tensor is a symmetric tensor with six unknowns and is obtained from the averaging of the convective acceleration terms of the momentum equations. These six unknowns in combination with the four unknown flow parameters (three components of velocity and pressure) result in a total of ten unknowns, for which we have only four equations. As a result, the RANS equations need additional modelling for closure, and hence a suitable turbulence closure model must be used.

The RANS models we consider employ the eddy viscosity model, which is mathematically analogous to the stress and strain rate relation for a Newtonian fluid [56]. This model, also known as The Boussinesq approximation, allows for a simple expression for Reynolds stress based on turbulent kinetic energy k , eddy viscosity μ_t and mean strain rate as shown in the equation below.

$$-\overline{\rho u'_i u'_j} = \mu_t \left(\frac{\partial \bar{u}_i}{\partial x_j} + \frac{\partial \bar{u}_j}{\partial x_i} \right) - \frac{2}{3} \delta_{ij} (\rho k) \quad (2-10)$$

The eddy viscosity models which are incorporated in the ANSYS Fluent solver are listed below, and a short background on these models is discussed in Appendix B.

1. Spalart-Allmaras(SA) model
2. k - ϵ model
 - Standard k - ϵ model
 - RNG k - ϵ model
 - Realizable k - ϵ model
3. k - ω model
 - Standard k - ω model
 - SST k - ω model
4. k - k_L - ω transition model
5. SST transition model

2-4 Computational Domain & Type of Boundary Conditions

Both 2-dimensional(2D) and the 3-dimensional(3D) computational domains are used in the present study. For the former, the inverted airfoil profile without the endplates is chosen. However, in the 2D airfoil case, the tip-vortices are not captured, which can only be captured in the 3D computational domain.

2-4-1 2D Computational Domain

For the 2D airfoil, as the geometry is relatively simple, a structured grid is generated using the ANSYS meshing module as shown in Figure 2-3. The computational domain is set such that inlet is located at $5c$ upstream of the wing, outlet is located at $10c$ downstream of the wing, top-wall is located at a height $5c$ from the wing and the ground clearance is set at $0.179c$. A ground clearance of $0.179c$ is chosen since, typically, the ride height range in which the Formula One cars operate is $0.150c$ — $0.250c$. Also, the behavior of the 2-dimensional Tyrrell airfoil subjected to ground effect aerodynamics is well established for a ride height $h = 0.179c$ in the works of Zerihan et al. [7]. At the inlet, a velocity inlet boundary condition

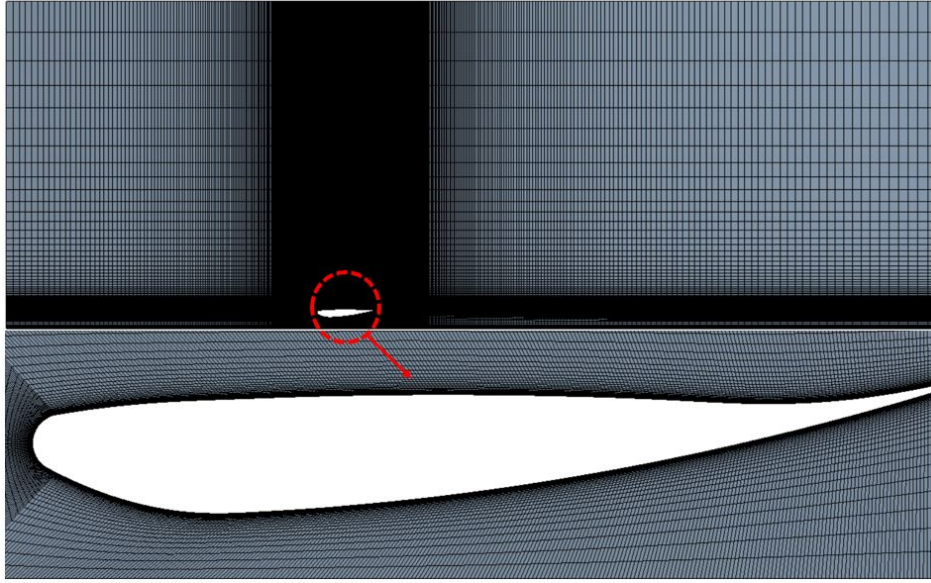


Figure 2-3: Structured grid for a 2D Tyrrell wing with $h/c = 0.179$ at $\alpha = 3.45^\circ$

is chosen, and the inlet velocity is varied as a function of time as discussed in the Section 2-1-3, in order to impose the accelerating flow. The pressure outlet was specified as uniform gauge pressure 0 Pa relative to the atmospheric pressure of 101,325 Pa. The top-wall and the ground are modelled as no slip walls, with the ground plane modelled as stationary relative to the freestream velocity.¹

The value of wall y^+ is maintained below 1 over the airfoil and the ground wall. The distance of the first node from a wall (Δy_1) is non-dimensionalized in the form of y^+ value (y^+) expressed as:

$$y^+ = \frac{u_\tau \Delta y_1}{\nu} \quad (2-11)$$

Here u_τ denotes the frictional velocity determined using wall shear stress (τ_w) and density (ρ).

$$u_\tau = \sqrt{\frac{\tau_w}{\rho}} \quad (2-12)$$

$$\tau_w = \mu \left(\frac{\partial u}{\partial y} \right)_{y=0} \quad (2-13)$$

2-4-2 3D Computational Domain

For the 3-dimensional wing with endplates, Pointwise V18.4 is employed to generate a hybrid mesh. In order to generate the hybrid mesh, *Voxel* block meshing strategy is employed

¹An alternative approach is to implement the frame motion with a stationary ground plane in the absolute frame and a zero velocity in the absolute frame at the inlet. The values of lift and drag forces altered from the former approach by approximately 0.01%. The minor differences in the values of the forces are due to the fact that the numerical errors do not exhibit Galilean invariance. A detailed comparison of the two different approaches can be found in the Appendix C.

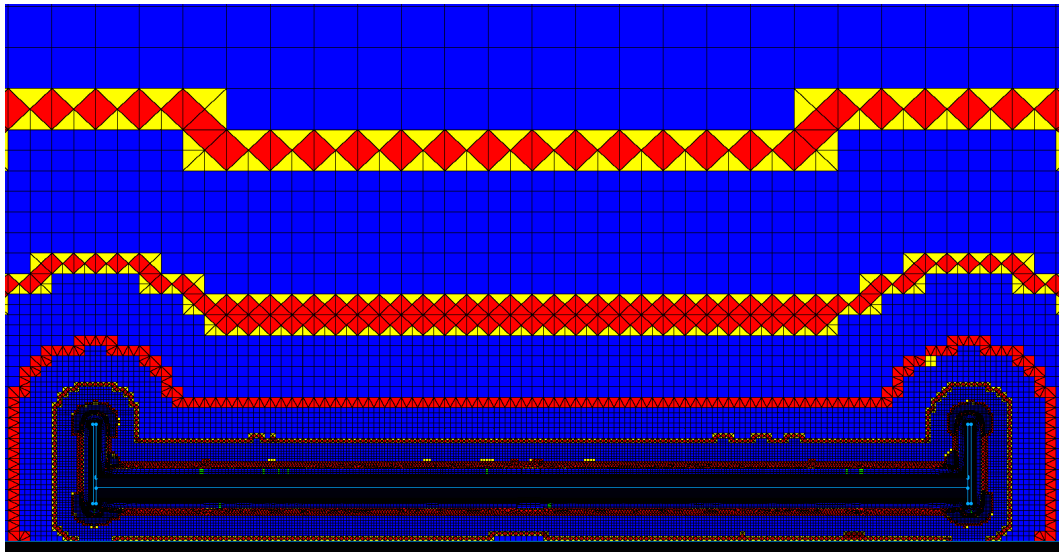


Figure 2-4: Hybrid grid for a 2D Tyrrell wing with $h/c = 0.224$ at $\alpha = 3.45^\circ$

which allows for generating meshes that resolve boundary layers, wakes, and other phenomena encountered in flows by extruding layers of high-quality, high aspect ratio tetrahedrons. The Voxel block meshing generates a hybrid mesh consisting of hexahedral cells which are clustered about the 3-dimensional wing, as shown in Figure 2-4. Transition between the levels in the hexahedral mesh in the proximity of the 3-dimensional wing are constructed using the tetrahedral cells and pyramids [57]. In order to accurately capture the wake region, local refinement is carried out downstream of the 3-dimensional wing, as illustrated in the Figure 2-5.

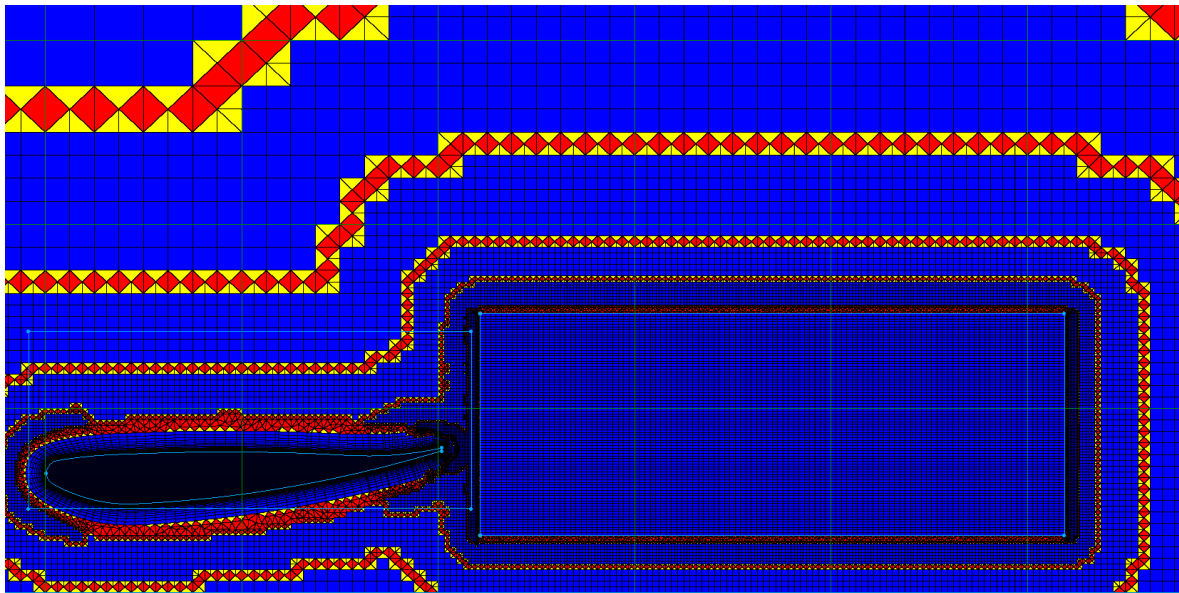


Figure 2-5: Hybrid grid for a 2D Tyrrell wing with $h/c = 0.224$ at $\alpha = 3.45^\circ$

The computational domain is built such that inlet is located at $5c$ upstream of the wing, outlet

is located at $10c$ downstream of the wing, top-wall is located at a height $5c$ from the wing and the ground clearance is set at $0.224c$. A ground clearance of $0.224c$ is chosen since, typically, the ride height range in which the Formula One cars operate is $0.150c$ — $0.250c$. Also, the behavior of the 2-dimensional Tyrrell airfoil subjected to ground effect aerodynamics is well established for a ride height $h = 0.224c$ in the works of Zerihan et al. [5]. The side-walls are located at a distance $7c$ from the endplates. At the inlet, a velocity inlet boundary condition is chosen, and the inlet velocity is varied as a function of time as discussed in the Section 2-1-3, in order to impose the accelerating flow. The pressure outlet was specified as uniform gauge pressure 0 Pa relative to the atmospheric pressure of $101,325$ Pa. The top-wall and the ground are modelled as no slip walls, with the ground plane modelled as stationary relative to the freestream velocity. The side-walls are modelled as stationary, no-slip walls.

2-5 Solution Methods

For the current study, a pressure-based solver was adopted, since previous studies have indicated that compressibility effects at simulated mach numbers were negligible [58]. Pressure-velocity coupling is accomplished by implementing the SIMPLE(Semi Implicit Method for Pressure Linked Equations) algorithm. The advantage of this technique is that the mass and momentum are conserved simultaneously at each time step. The fluent user manual recommends using the SIMPLE pressure-velocity coupling method for cases that require small-time steps, as it significantly reduces the computational expense [59]. The SIMPLE algorithm involves several steps, which are repeated iteratively until the convergence criterion is satisfied.

- Initially, the momentum equation(Equation 1-10) is solved to obtain an approximate velocity field. The pressure gradient term is determined utilizing the previous iteration or an initial guess.
- In order to obtain the new pressure distribution, the pressure equation is formulated and solved.
- Then, the velocities are corrected and a new set of conservative fluxes are calculated.

Least Squares Cell-Based method is employed for the evaluation of spatial gradients as it is computationally efficient when compared to the Node based gradient methods. Although the Green Gauss Cell-based method is the least computationally expensive gradient spatial discretization scheme available in Fluent, it is avoided since it is prone to false numerical diffusion. A second order scheme is chosen for pressure interpolation at the cell faces. Third-Order MUSCL scheme is implemented for the discretization of the Momentum. The Third-Order MUSCL offers the stability of the second-order upwind scheme and accuracy of the central differencing scheme since, it is a blend of the second-order upwind scheme and the central differencing scheme. Also, the Fluent user manual recommends this scheme for all types of meshes since it has the potential to improve spatial accuracy by minimizing the numerical diffusion. The second-order upwind spatial discretization scheme is used for the Turbulent Kinetic Energy and Specific Dissipation Rates. The Bounded Second-Order Implicit scheme is employed for the temporal discretization because of its ability to enhance the numerical stability since the variables(like Turbulent Kinetic Energy) are bounded.

A detailed mathematical treatment of the above-mentioned methods can be found in the Fluent Theory Guide [60]. The summary of all the settings implemented in the Fluent solver can be found in Appendix D.

2-6 Turbulence Model Validation Study

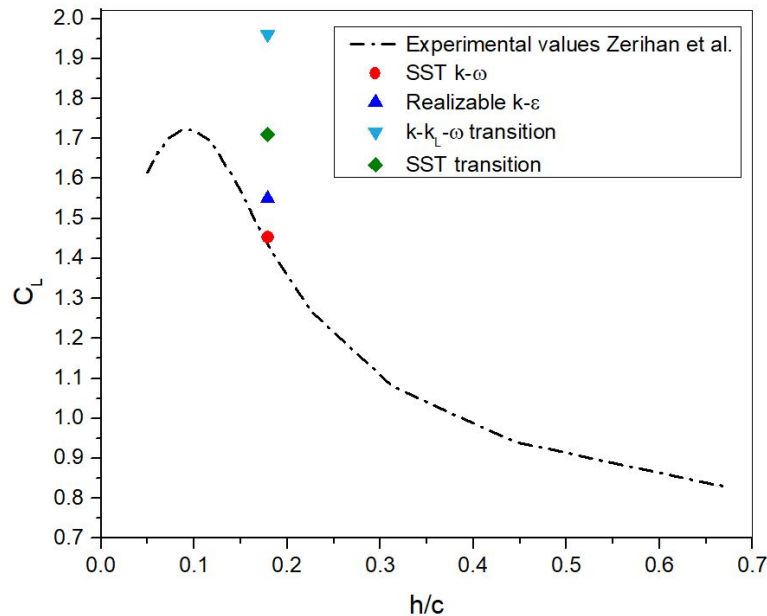


Figure 2-6: Experimental aerodynamic downforce for a single element airfoil in ground effect at $\alpha = 3.45^\circ$ from Zerihan et al.[7] is compared with the aerodynamic downforces returned by the four different eddy viscosity turbulence models.

As the computational costs are lower for a 2D computational domain, initially, a turbulence model validation study was performed for the 2D computational domain. The study revealed that the realizable $k-\epsilon$ model, with enhanced wall treatment and the SST $k-\omega$ model returned satisfactory values of downforce coefficients when compared to the values obtained from the experimental investigations of Zerihan[5]. However, in cases where the airfoil was located at ground heights, $h/c \leq 0.224$, flow separation was observed on the suction side of the airfoil at the trailing edge.

In the scenarios involving flow separation, the SST $k-\omega$ model returned more accurate values of downforce, as shown in the Figure 2-6. Experimental investigations on the Tyrrell wing subjected to ground effect aerodynamics revealed that, for a ride height $h = 0.224c$, flow separation was observed at the trailing edge of the wing on the suction side, at $x/c \sim 0.9$ [5]. The separation point was found to move further upstream on further reduction in the ride height value. The SST $k-\omega$ model was able to capture the flow separation accurately at the trailing edge on the suction side of the airfoil, as indicated by the wall shear stress values in Figure 2-7, at $x/c \sim 0.85$. Furthermore, the SST $k-\omega$ model returned values of surface pressure which closely agreed with the experimental values, as shown in the Figure 2-8. Based on these results, the SST $k-\omega$ turbulence model is chosen for all further simulations.

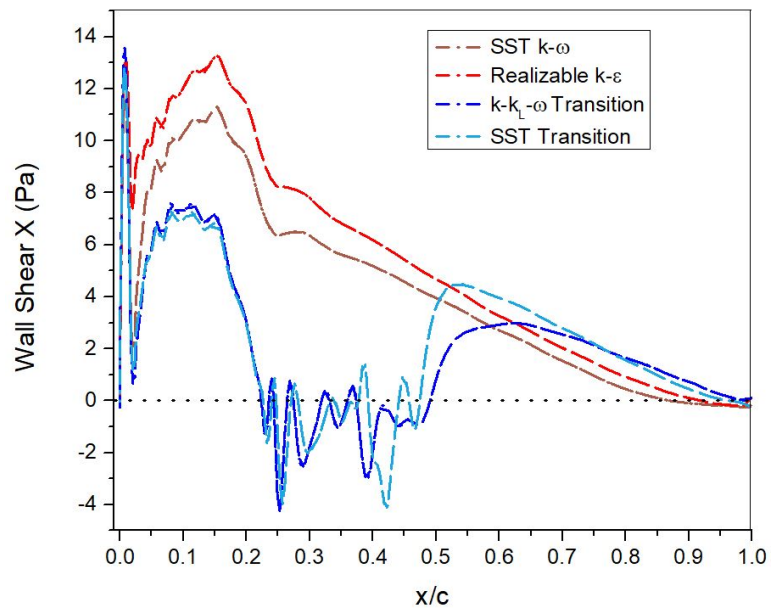


Figure 2-7: Wall Shear Stress values on the suction side of the airfoil at $\alpha = 3.45^\circ$ for $h/c = 0.179$

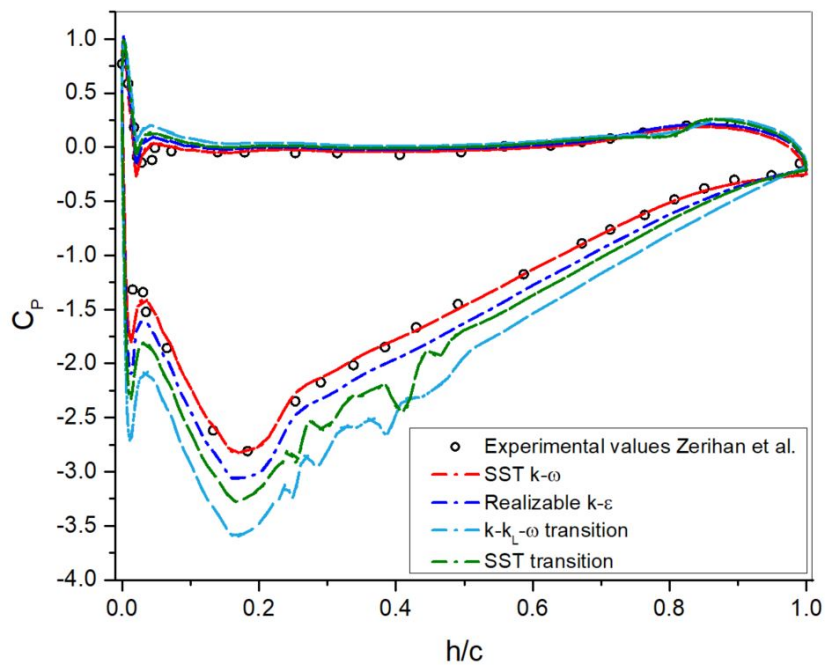


Figure 2-8: Experimental surface pressure distribution on the airfoil at $\alpha = 3.45^\circ$ for $h/c = 0.179$ [7] compared with the surface pressure distributions returned by the four eddy viscosity models

Results and discussion

3-1 Mesh independence study

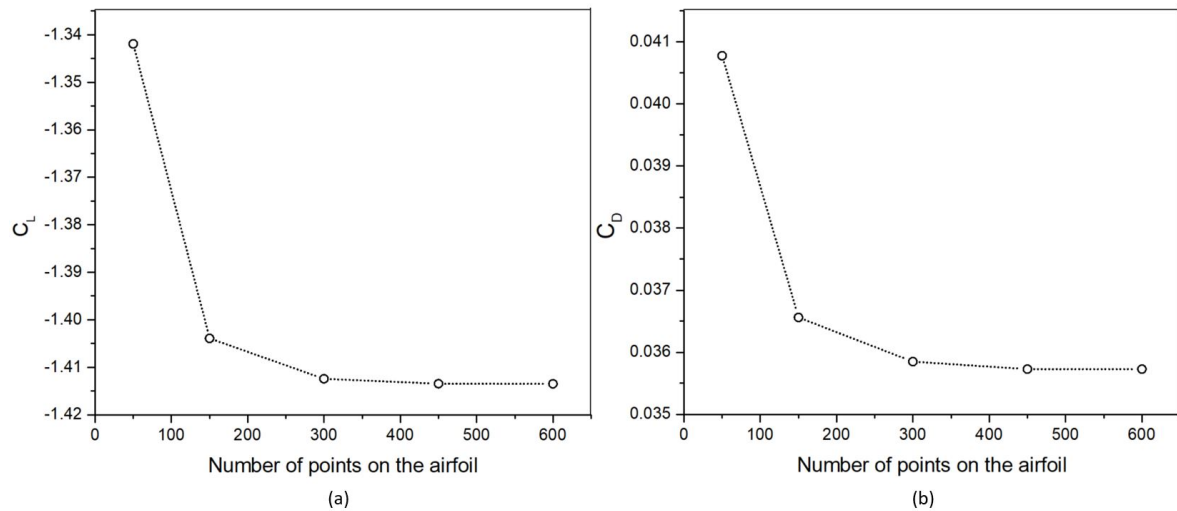


Figure 3-1: Variation of (a)downforce coefficient and (b)drag coefficient for the five different grids. The force coefficient decreases with increase in the number of points on the airfoil and asymptotically approach a constant value.

For the mesh independence study, a 2-dimensional airfoil with the chord length, $c = 223.4$ mm, a ground height $h = 0.179c$ and an aspect ratio 4.92 airfoil is chosen. Five different grids are employed to determine the sensitivity to grid refinement and are tested for the case present in Zerihan et al. [7]. The number of the points on the surface of the airfoil was increased in steps, while maintaining a constant value of $y^+ \sim 1$ for the five different grids. The streamwise velocity of the air was set at a constant 30 m/s, which corresponded to a chord Reynolds number of 4.5×10^5 . The ground wall was modelled as stationary relative to the free stream air. The Figures 3-1(a) and 3-1(b) illustrate the variation of the force coefficients

with the number of points on the airfoil. Furthermore, the CFD pressure distribution on the airfoil surface for the fine mesh, i.e., the one with 600 points on the airfoil is validated by comparison against the experimental pressure distribution results at the mid-plane of the 3-dimensional wing(i.e., $z = 0$ plane) from Zerihan et al. [7] in the Figure 3-2.

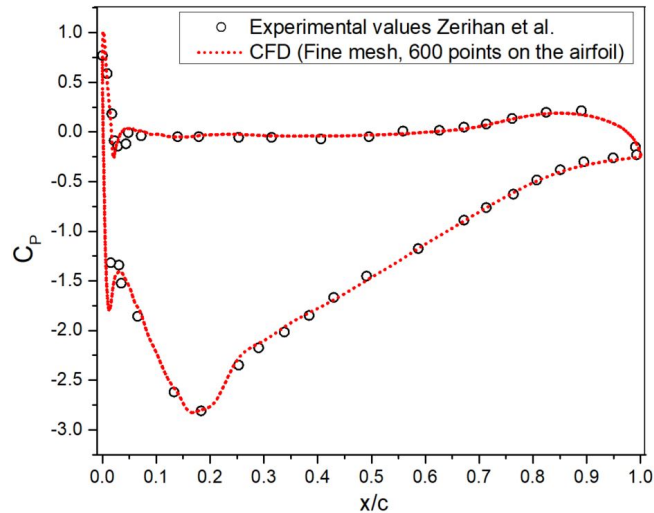


Figure 3-2: 2D Airfoil surface pressure distribution for the fine mesh, i.e., the one with 600 points on the airfoil circumference. Comparisons with the experimental values of pressure distribution [7] reveal no significant difference in the pressure distribution at $z = 0$ plane for the ride height, $h/c = 0.179$

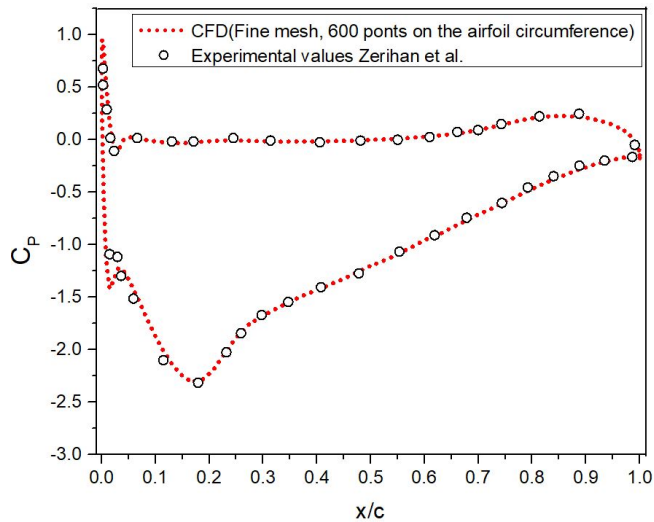


Figure 3-3: 3D Airfoil surface pressure distribution at the mid-plane for the fine mesh, i.e., the one with 600 points on the airfoil circumference. Comparisons with the experimental values of pressure distribution [7] reveal no significant difference in the pressure distribution at $z = 0$ plane for the ride height, $h/c = 0.224$

A similar approach is followed for the 3-dimensional airfoil with endplates. A y^+ value of ~ 1 is maintained on the airfoil surface and the same number of points along the airfoil circumference is maintained. A fine mesh with 40 million cells is generated, and the pressure

distribution on the airfoil surface at the mid-plane $z = 0$ is validated by comparing against the experimental pressure distribution results from Zerihan et al. [7], as shown in the Figure 3-3.

From the mesh independence study, it is evident that the fine mesh, i.e., the mesh with 600 points along the circumference of the airfoil and a y^+ value of ~ 1 on the airfoil surface returned satisfactory values of pressure distribution on the airfoil surface when compared to that obtained from the experimental investigation. Henceforth, for all further simulations, the mesh is generated with 600 points along the airfoil circumference and a y^+ value of ~ 1 on the airfoil surface.

3-2 Navier Stokes Equation in the non-inertial frame: A Scaling Analysis

In this section, a scaling analysis is performed to determine the relevant non-dimensional numbers that govern the physics of the flow over an accelerating airfoil. For the accelerating airfoil, the Navier-Stokes equation in the non-inertial frame is,

$$\rho \left[\frac{\partial \underline{u}}{\partial t} + \underline{u} \cdot \underline{\nabla} \underline{u} \right] = -\underline{\nabla} p + \mu \underline{\nabla}^2 \underline{u} - \frac{\rho V[\underline{x}, t]}{\partial t} \quad (3-1)$$

Non-dimensionalizing the relevant length, velocity and time scales,

$$\begin{aligned} \underline{x} &= C \underline{x}^* \\ t &= \tau t^* \\ p &= \pi p^* \\ \underline{\nabla} &= \frac{1}{C} \underline{\nabla}^* \\ \underline{u}(x, t) &= U \underline{u}^* \\ a_x &= A a_x^* \end{aligned} \quad (3-2)$$

where, C is the chord length scale, τ is the acceleration timescale, U is the velocity scale, π is the characteristic pressure and A is the acceleration scale.

From the Equations 3-1 and 3-2,

$$\begin{aligned} \rho \left[\frac{\partial U \underline{u}^*}{\partial \tau t^*} + U \underline{u}^* \cdot \frac{1}{C} \underline{\nabla}^* U \underline{u}^* \right] &= -\frac{1}{C} \underline{\nabla}^* \pi p^* + \frac{\mu}{C^2} \underline{\nabla}^{*2} U \underline{u}^* - \rho A a_x^* \\ \left(\frac{\rho U}{\tau} \right) \frac{\partial \underline{u}^*}{\partial t^*} + \left(\frac{\rho U^2}{C} \right) \underline{u}^* \cdot \underline{\nabla}^* \underline{u}^* &= -\frac{\pi}{C} \underline{\nabla}^* p^* + \frac{\mu U}{C^2} \underline{\nabla}^{*2} \underline{u}^* - \rho A a_x^* \end{aligned} \quad (3-3)$$

In the inertial regime, the term π scales with the dynamic pressure ρU^2 . Dividing the Equation 3-3 by $\frac{\rho U^2}{C}$,

$$\underbrace{\left[\frac{C}{U \tau} \right]}_{\text{Term 1}} \frac{\partial \underline{u}^*}{\partial t^*} + \underbrace{\underline{u}^* \cdot \underline{\nabla}^* \underline{u}^*}_{\text{Convective Acceleration}} = -\underline{\nabla}^* p^* + \underbrace{\left[\frac{\mu}{\rho U C} \right]}_{\text{Term 2}} \underline{\nabla}^{*2} \underline{u}^* - \underbrace{\left[\frac{AC}{U^2} \right]}_{\text{Term 3}} a_x^* \quad (3-4)$$

In the equation above, τ is replaced with $\sqrt{\frac{C}{A}}$, which is the timescale for the flow to travel a distance C with an acceleration A.

$$\underbrace{\left[\sqrt{\frac{AC}{U^2}} \right]}_{\text{Term 1}} \frac{\partial \underline{u}^*}{\partial t^*} + \underbrace{\underline{u}^* \cdot \underline{\nabla}^* \underline{u}^*}_{\text{Convective Acceleration}} = -\underline{\nabla}^* p^* + \underbrace{\left[\frac{\mu}{\rho U C} \right]}_{\text{Term 2}} \underline{\nabla}^{*2} \underline{u}^* - \underbrace{\left[\frac{AC}{U^2} \right]}_{\text{Term 3}} a_x^* \quad (3-5)$$

In the Equation 3-5, the inverse of *Term 1* corresponds to the Froude number, the inverse of *Term 2* corresponds to the Reynolds number and the inverse of *Term 3* corresponds to the Froude number squared. The Equation 3-5 reveals that the two non-dimensional parameters that govern the flow over an accelerating airfoil are the *Reynolds number* and the *Froude number*.

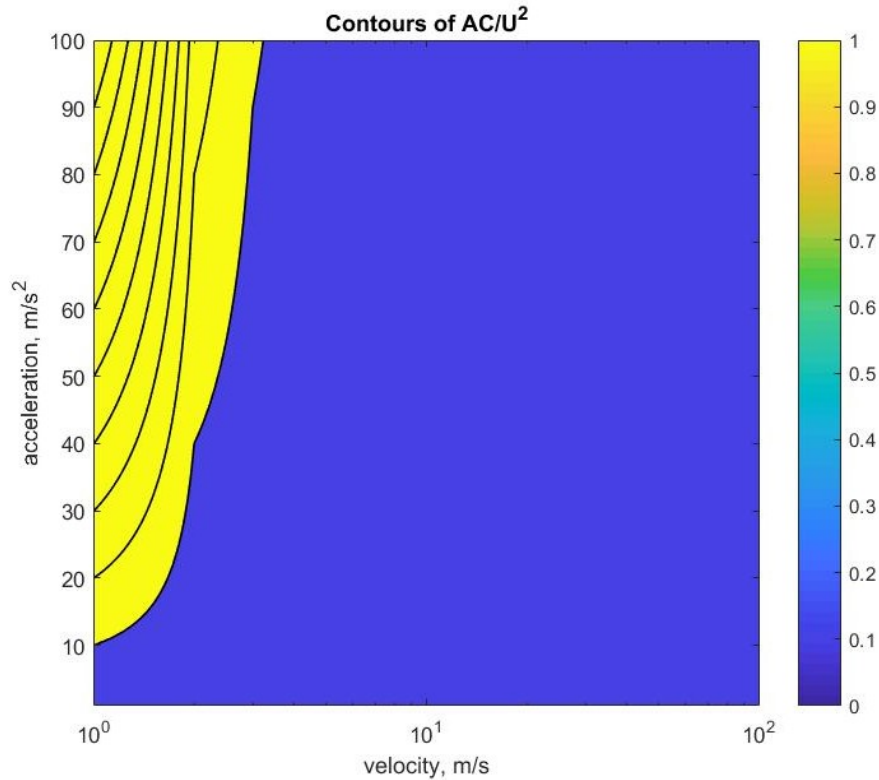


Figure 3-4: Contours of non-dimensional AC/U^2 in the Equation 3-4 for a unit chord length for velocities in the range 1-100 m/s and acceleration in the range 1-100 ms^{-2} (Note that the x-axis (velocity) is in the log scale).

The Figure 3-4 shows the contours of the non-dimensional *Term 3* in the Equation 3-4. From the Equation 3-4, it is evident that translational acceleration becomes relevant when the order of magnitude of the non-dimensional AC/U^2 is $O(1)$. From the Figure 3-4, the order of magnitude of the non-dimensional AC/U^2 from the Equation 3-4 is 1 and higher for values of velocity ≤ 3 m/s and acceleration ≥ 10 ms^{-2} . However, we limit our discussions to realistic on track values of velocities and acceleration, where in, the value of non-dimensional AC/U^2 in the Equation 3-4 is < 1 .

3-3 Translational Acceleration & Deceleration:2-Dimensional Airfoil

In this section, we review the influence of the translational acceleration and deceleration on the drag and lift forces for a 2-dimensional inverted airfoil in ground effect.

3-3-1 Piecewise Linear Velocity Profile

Velocity & Acceleration Profile

The 2-dimensional airfoil with a ground clearance of $h=0.179c$ and a unit chord length is accelerated and decelerated with a linear velocity profile as shown in the Figure 2-1. The ground height $h/c = 0.179$ is chosen since it is a well established case in the works of Zerihan [5] and is in the range of ground clearances that the race cars operate in, i.e., $0.150c-0.250c$. The flow is accelerated from a flow-time $t = 3s$ to $t = 4.2s$. The acceleration corresponding to this velocity profile is $a = \pm 6.25\text{ms}^{-2}$, which is something that a race car can typically encounter on a racetrack. The chord Reynolds number of the accelerating airfoil varies from 2×10^6 to 2.6×10^6 , which is the order of chord Reynolds number that the front wing encounters on a racetrack. The non-dimensional *Term 3* in the Equation 3-4 attains a peak of ~ 0.007 on acceleration and ~ -0.01 on deceleration.

Downforce generated by the airfoil & the drag force on the airfoil

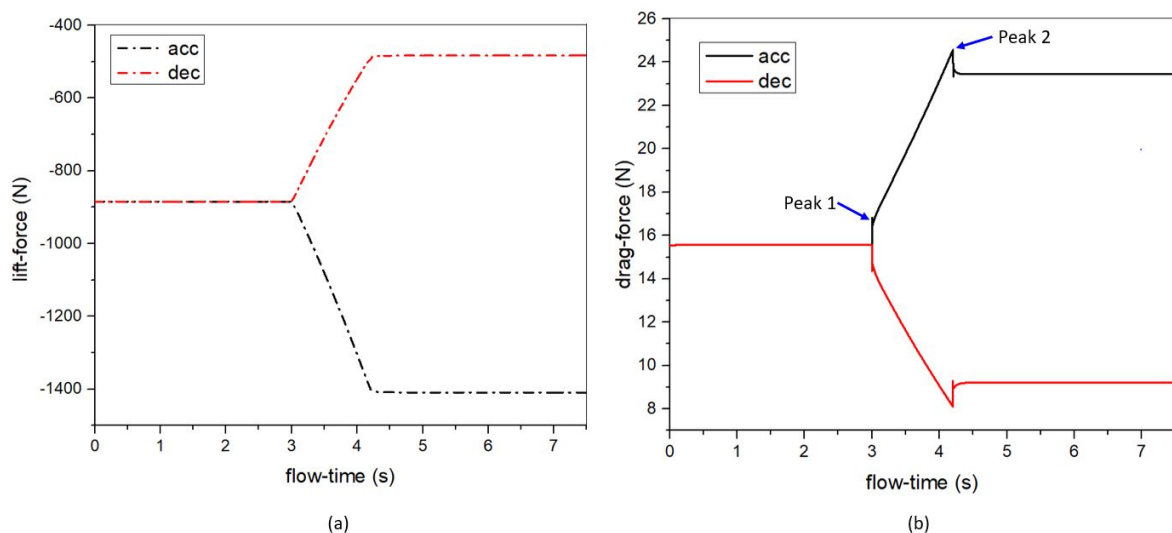


Figure 3-5: (a) Downforce generated by the airfoil accelerated with the piecewise linear velocity profile, (b) Drag force on the airfoil accelerated with the piecewise linear velocity profile.

The downforce generated by the wing and the drag force on the airfoil are monitored for the duration of the flow. Figure 3-5 shows the downforce and the drag force for the airfoil as a function of time. The drag force in the Figure 3-5(b) clearly exhibits two distinct local maxima, indicated as 'peak 1' and 'peak 2', which coincide with the time when acceleration (or

deceleration) starts and ends. After the 'peak 2', the drag force drops to a steady value for $t \geq 4.2s$. These peaks are a result of the added mass and the sudden commencement of the acceleration of the airfoil. Figure 3-6(b) exhibits the difference in the drag forces on the accelerating(or decelerating) airfoil when compared to the steady state drag forces on the airfoil at the same velocities as a result of the added mass. The accelerating airfoil experiences a drag force which is greater than the one experienced by the airfoil at steady-state velocities by $\sim 6\%$. To give a more physical picture, the added mass is the additional weight added to a system due to the fact that an accelerating(or decelerating) airfoil must move some volume of the surrounding fluid with it as it moves.

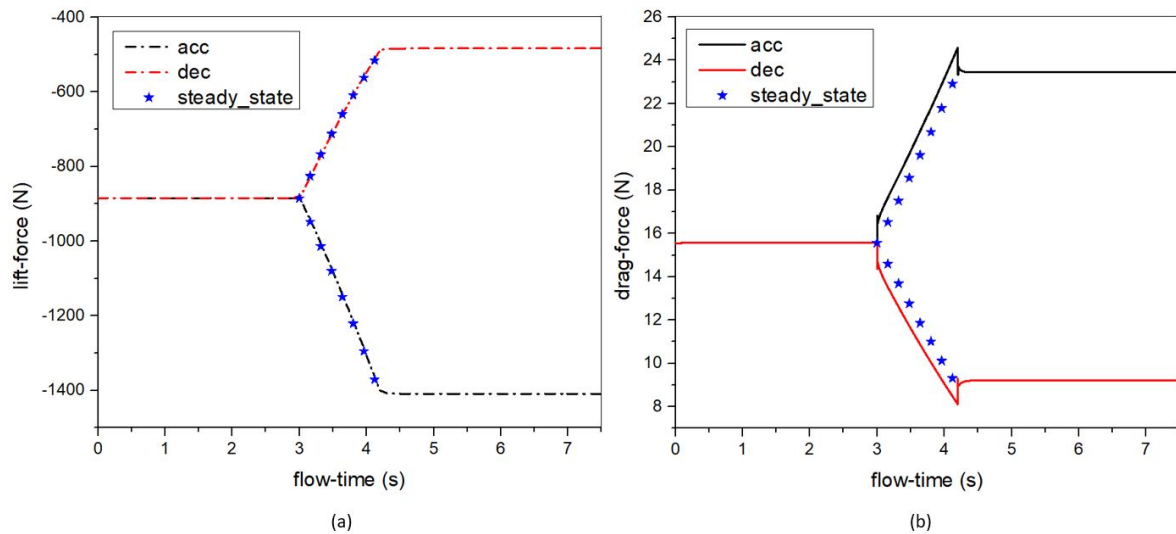


Figure 3-6: (a)Downforce generated by the accelerating airfoil with the piecewise linear velocity profile, (b)Drag force on the airfoil accelerated with the piecewise linear velocity profile. The downforce generated at the same steady state velocities as the accelerating(or decelerating) airfoil reveal no significant differences, while the drag force encountered by the accelerating(or decelerating) airfoil is higher(or lower) than that encountered by the airfoil at the same steady state velocities.

The downforce in Figure 3-5(a) exhibited no distinct peaks when the acceleration commences and ends, unlike the drag force. The comparison of the downforce generated by an accelerating(or decelerating) airfoil with that generated by the airfoil at steady state velocities in Figure 3-6(a) showed no significant differences between the two. Since the airfoil is accelerated in the x-direction, the added mass effects on the force can be seen only be seen in the x-direction, i.e., the drag force.

Typically, the steady state downforce for an airfoil is defined as,

$$F_L = \frac{1}{2}\rho V^2 C_L A \quad (3-6)$$

where ρ is the density of the fluid, V is steady state velocity, A is the rectangular planform area of the airfoil and C_L is the lift coefficient corresponding to the airfoil. From the Figure 3-6(a), it can be seen that, for the airfoil accelerated with the piecewise linear velocity profile, the downforce generated by the airfoil at the same steady state velocities are not significantly

different from that generated by the accelerating airfoil. For the airfoil accelerated with the piecewise linear velocity profile in Figure 2-1, the downforce can be modelled as,

$$F_L(t) = \frac{1}{2}\rho V(t)^2 C_L A \quad (3-7)$$

Typically, the steady state drag force on an airfoil is defined as,

$$F_D = \frac{1}{2}\rho V^2 C_D A \quad (3-8)$$

where ρ is the density of the fluid, V is steady state velocity, A is the frontal area corresponding to the airfoil and C_D is the drag coefficient corresponding to the airfoil. However, when the airfoil is accelerated through a fluid, the added mass effects must be added to the Equation 3-8. The modified equation for the drag is,

$$F_D(t) = F_{CD}(t) + F_{vm}(t) = \underbrace{\frac{1}{2}\rho V(t)^2 C_D A}_{F_{CD}(t)} + \underbrace{m_{am} a(t)}_{F_{am}(t)} \quad (3-9)$$

where F_{CD} is the steady state drag force and F_{am} is the virtual force as a result of the product of the added mass m_{am} and the acceleration of the airfoil $a(t)$. The added mass includes the mass of the airfoil and the mass of the fluid that accelerates with the airfoil as the airfoil is accelerated in the fluid. The peaks in the Figure 3-5 can be explained using the Equation 3-9, where the virtual force term, i.e., F_{am} is zero for $t \leq 3.0$ s and for $t > 4.2$ s.

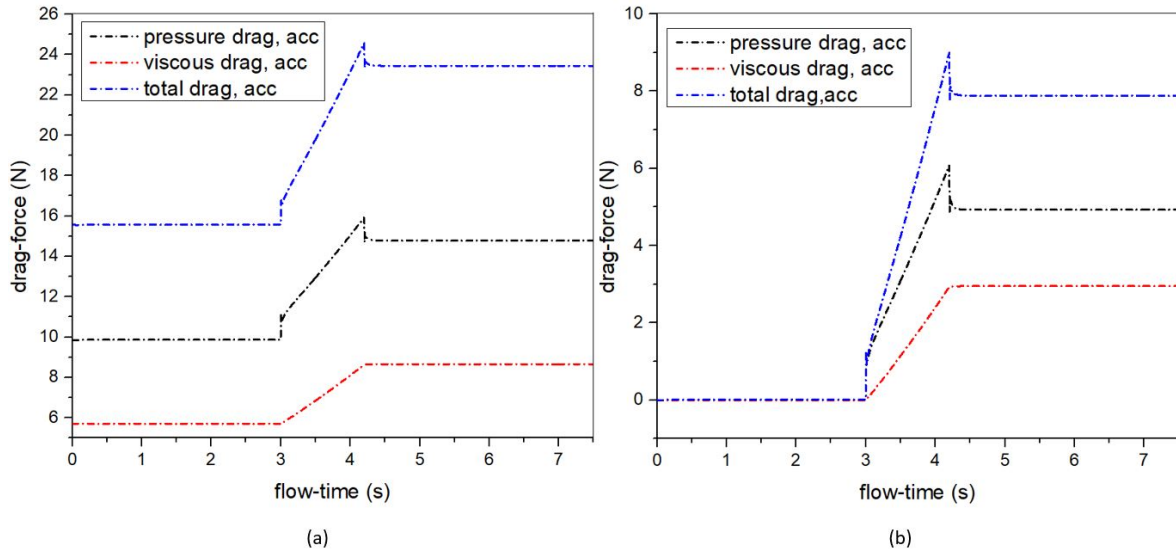


Figure 3-7: (a) Pressure drag and viscous drag contributions to total drag encountered by the airfoil accelerated with the piecewise linear velocity profile, (b) Pressure drag and viscous drag contributions to total drag encountered by the airfoil accelerated with the piecewise linear velocity profile, with baseline correction. The plots reveal that the peaks observed in the total drag force at the start and end of the acceleration are a result of the pressure drag.

The total drag force encountered by the accelerating airfoil can be split into two components; namely, the pressure drag and the viscous drag, as shown in the Figure 3-7. The pressure drag

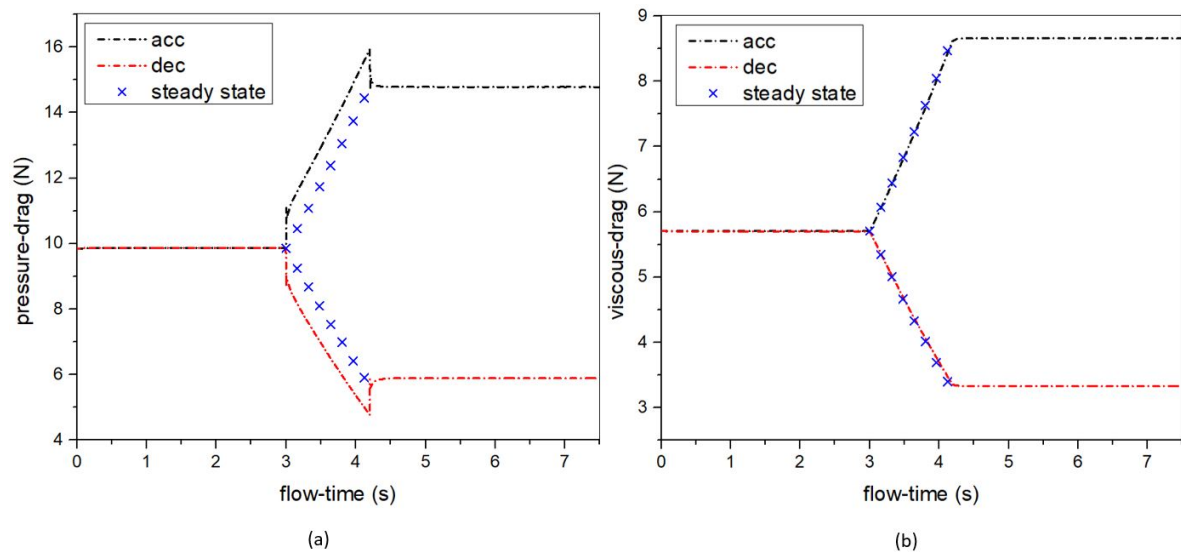


Figure 3-8: (a) Pressure drag on the airfoil accelerated (and decelerated) with the piecewise linear velocity profile. The pressure drag on the airfoil at the same steady state velocities as the accelerating (or decelerating) airfoil reveal that the drag force encountered by the accelerating (or decelerating) airfoil is higher (or lower) than that encountered by the airfoil at the same steady state velocities. (b) Viscous drag on the airfoil accelerated (and decelerated) with the piecewise linear velocity profile. The viscous drag at the same steady state velocities as the accelerating (or decelerating) airfoil reveal no significant differences.

is attributed to the pressure difference between the upstream and the downstream surfaces of the airfoil. The pressure drag is the resultant of resolved forces normal to the airfoil surface. The viscous drag can be attributed to the viscous shear of fluid over the airfoil surface. The viscous drag is the resultant of the resolved forces tangential to the surface of the airfoil. From the plots in the Figure 3-7, it can be seen that the peaks in the drag force encountered by the accelerating airfoil at the start and end of the acceleration are a result of the pressure drag. This is reflected in the Figure 3-8, where the pressure drag can be modelled using the Equation 3-9 and the viscous drag can be modelled using the Equation 3-8.

However, it remains to be seen whether the peaks in the drag force are a result of the piecewise linear velocity profile used, and the corresponding acceleration profile, where in there is a sudden increase in the magnitude of acceleration from zero to a peak value and a sudden drop in the magnitude from the peak value to zero. In order to smoothen the acceleration profile, a non-linear velocity profile is generated using the Fermi-Dirac Equation 2-2, which results in a smoother velocity profile. The resulting drag and downforces for the non-linear velocity profile for accelerating and decelerating airfoil are discussed in the upcoming Section 3-3-2.

3-3-2 Non-linear Smooth Velocity Profile

3-3-2-1 2-Dimensional Airfoil: Ground Clearance $h=0.179c$ & Aspect Ratio=1

Velocity & acceleration profile for the accelerating airfoil

The non-linear smooth velocity profile for accelerating the airfoil is generated using the Equation 2-2 to resemble the velocity profiles that are encountered on a racetrack. Typically, on a racetrack, a Formula One car accelerates out of a corner and decelerates into the corner, and these values of accelerations range from 2g to -5g. In order to match these values of accelerations, the airfoil with a unit chord length and ground height $h = 0.179c$ is accelerated (and decelerated) with two distinct velocity profiles, shown in Figure 3-9(a). The corresponding acceleration profiles are shown in Figure 3-9(b) with the peak value of acceleration (and deceleration) achieved at $t = 3.6s$. Based on the velocity profile generated, the chord Reynolds number varies from 2×10^6 to 4.5×10^6 for the accelerating airfoil. For the decelerating airfoil, the chord Reynolds number varies from 5.8×10^6 to 2×10^6 . The non-dimensional *Term 3* in the Equation 3-4 attains a peak of ~ 0.01 for the 2g acceleration scenario and ~ -0.02 for the 5g deceleration scenario.

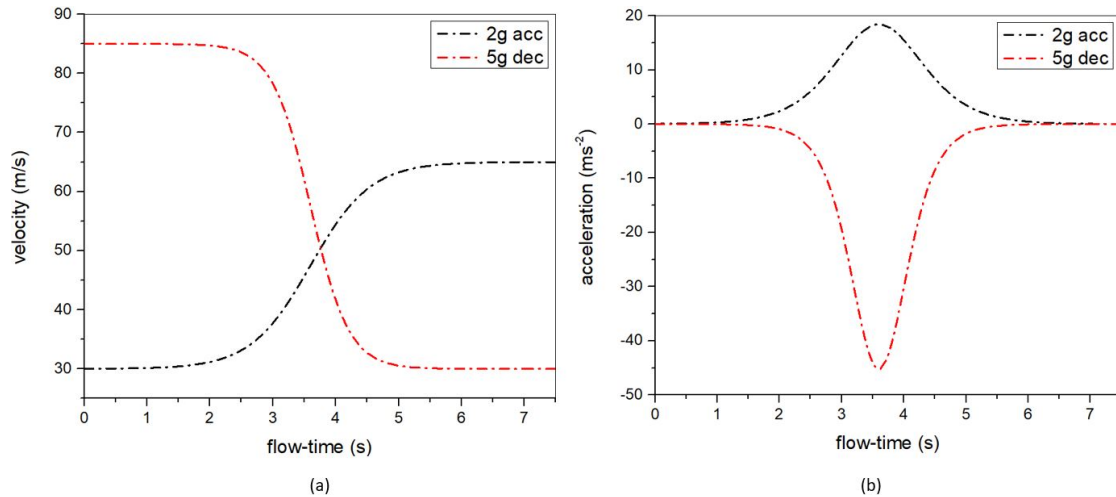


Figure 3-9: (a) Velocity profiles for accelerating and decelerating airfoil, (b) Acceleration profile for accelerating and decelerating airfoil

Downforce generated by the airfoil & the drag force on the airfoil

The downforce generated by the accelerating (and decelerating) airfoil, and the drag force it experiences is shown in Figure 3-10. The drag force on the accelerating (and decelerating) airfoil exhibits no local maxima (or minima) for a non-linear smooth velocity profile, unlike the drag force response for a piecewise linear velocity profile. Henceforth, for all further discussions, the airfoil is accelerated with a non-linear velocity profile generated using the Fermi-Dirac Equation 2-2.

$$C_{L/D} = \frac{2 \times Force}{\rho \times U(t)_{\infty}^2 \times Area} \quad (3-10)$$

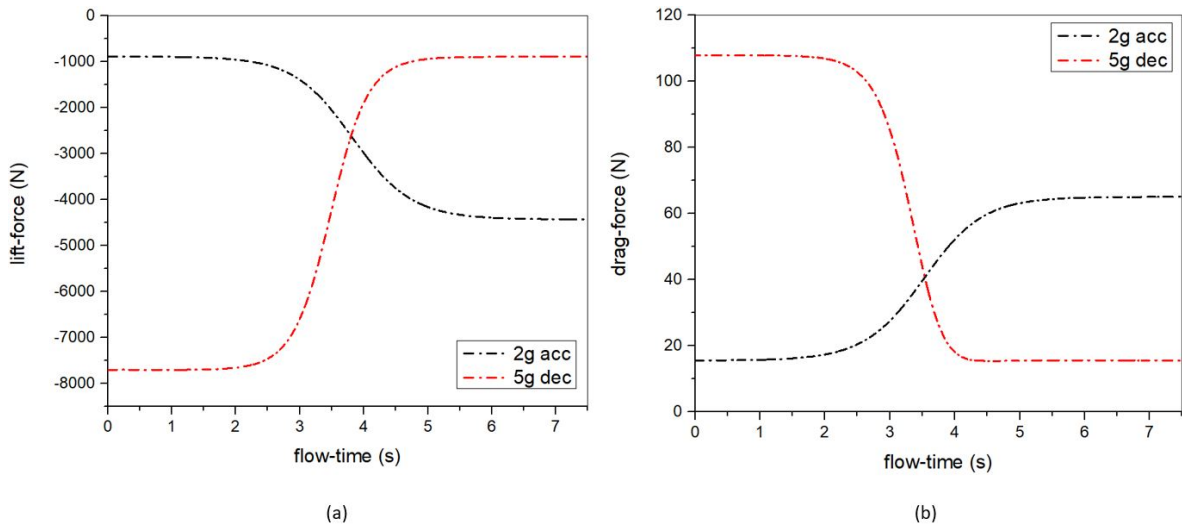


Figure 3-10: (a)Downforce generated by the airfoil accelerated with the non-linear velocity profile, (b)Drag force on the airfoil accelerated with the non-linear velocity profile

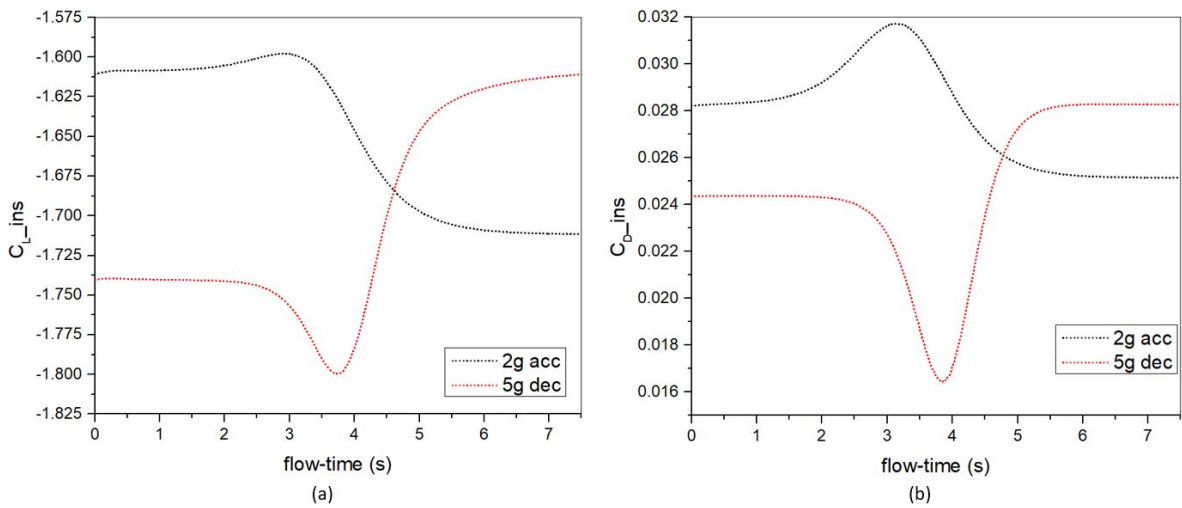


Figure 3-11: (a)Instantaneous downforce coefficient for the airfoil accelerated with the non-linear velocity profile, (b)Instantaneous drag coefficient for the airfoil accelerated with the non-linear velocity profile. The instantaneous force coefficients are obtained by non-dimensionalizing the forces with the instantaneous free stream velocity using the Equation 3-10

In order to quantify the influence of acceleration(or deceleration) on the downforce generated and the drag force on the airfoil, we non-dimensionalized the forces with the Equation 3-10. In the Equation 3-10, the rectangular planform area of the wing and the instantaneous free stream velocity U_{∞} are used to non-dimensionalize the force. The instantaneous force coefficients are plotted in the Figure 3-11 as a function of time. The force coefficients are further normalized using the force coefficient at $t = 0.0$ s, as shown in the Figure 3-12. The plots in Figure 3-12 reveal that the accelerating airfoil experiences a minimum which shows $\sim 1\%$ loss in downforce coefficient(i.e., $-C_L$), while the decelerating airfoil experiences a peak with $\sim 4\%$ gain in downforce coefficient(i.e., $-C_L$). Likewise, the accelerating airfoil experi-

ences a maximum in drag force coefficient by $\sim 10\%$ and the decelerating airfoil experiences a minimum, showing a drop in drag force coefficient by $\sim 30\%$. Detailed discussions on the influence of magnitude of acceleration(or deceleration) on the downforce and the drag force are performed in the upcoming Section 3-3-2-3.

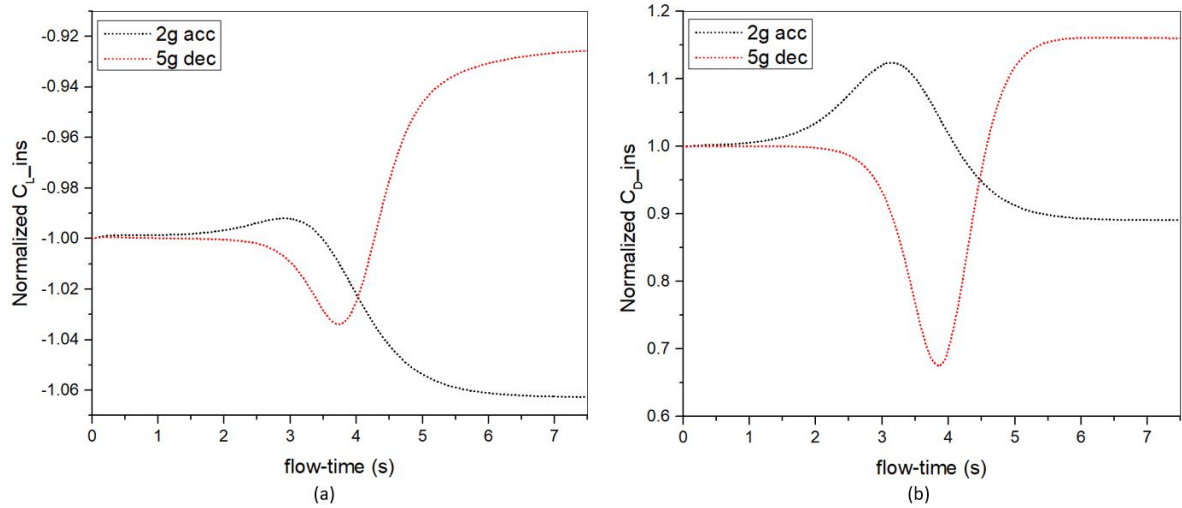


Figure 3-12: (a) Normalized downforce coefficient for the airfoil accelerated with the non-linear velocity profile, (b) Normalized drag coefficient for the airfoil accelerated with the non-linear velocity profile. The normalized force coefficients reveal that the accelerating airfoil undergoes a 1% loss in the downforce and experiences an additional drag force of 10%. Similarly, the decelerating airfoil experiences a 4% gain in the downforce and encounters a 30% reduction in the drag force.

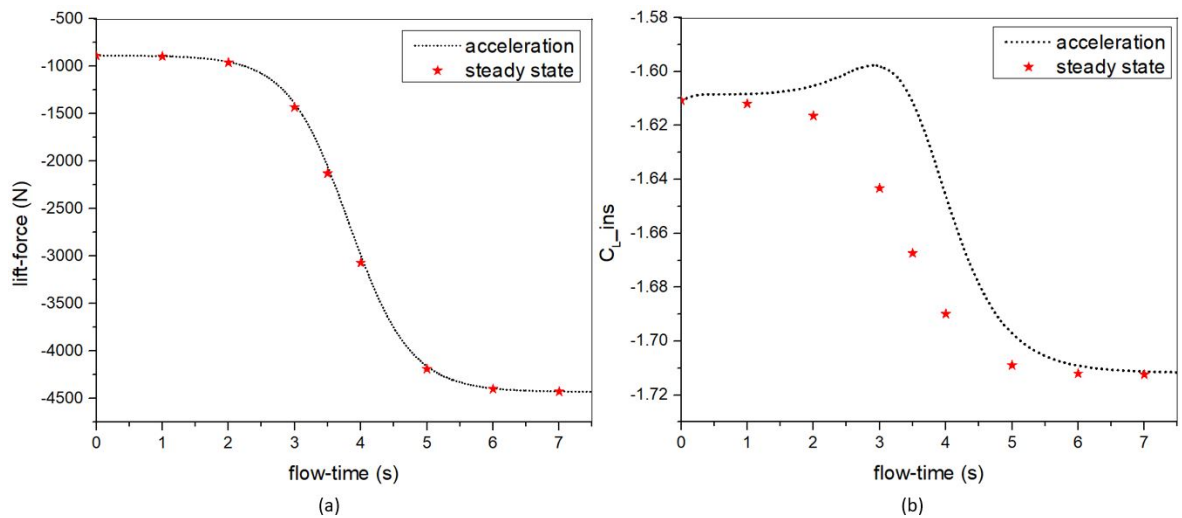


Figure 3-13: (a) Downforce generated by the accelerating airfoil at the angle of incidence 3.45° , (b) Downforce coefficient for the accelerating airfoil at the angle of incidence 3.45° . The downforce coefficients indicate that the accelerating airfoil experiences a 3% loss in downforce when compared to the airfoil at the same steady state velocity at $t = 3s$.

On comparison with the steady state forces in the Figures 3-13 and 3-14, the acceleration resulted in a loss of downforce and an increase in the drag force. Similarly, the deceleration

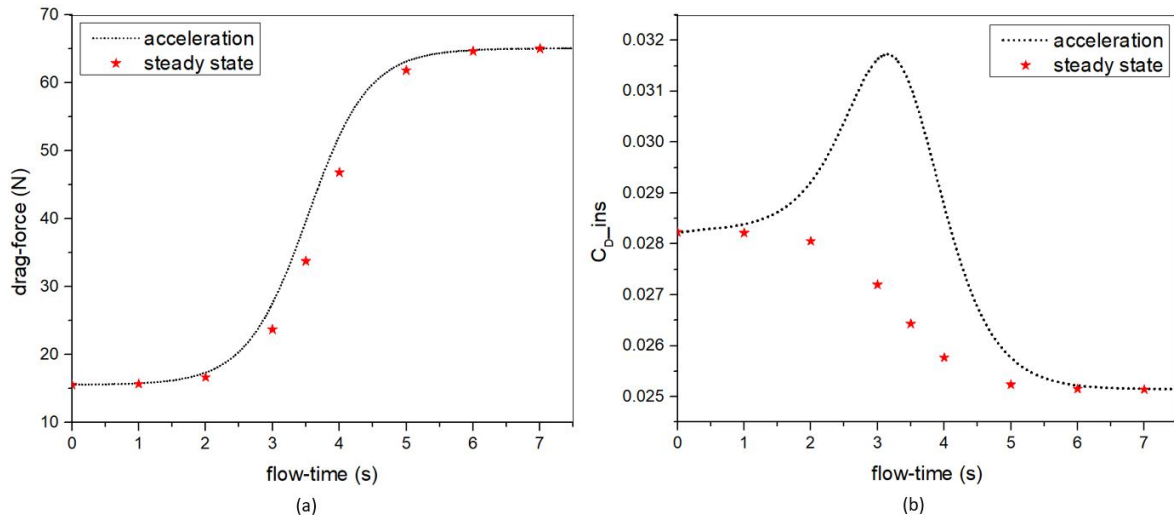


Figure 3-14: (a) Drag force on the accelerating airfoil at the angle of incidence 3.45° , (b) Drag force coefficient for the accelerating airfoil at the angle of incidence 3.45° . The drag force coefficients indicate that the accelerating airfoil experiences a 7% increase in the drag force when compared to the airfoil at the same steady state velocity at $t = 3s$.

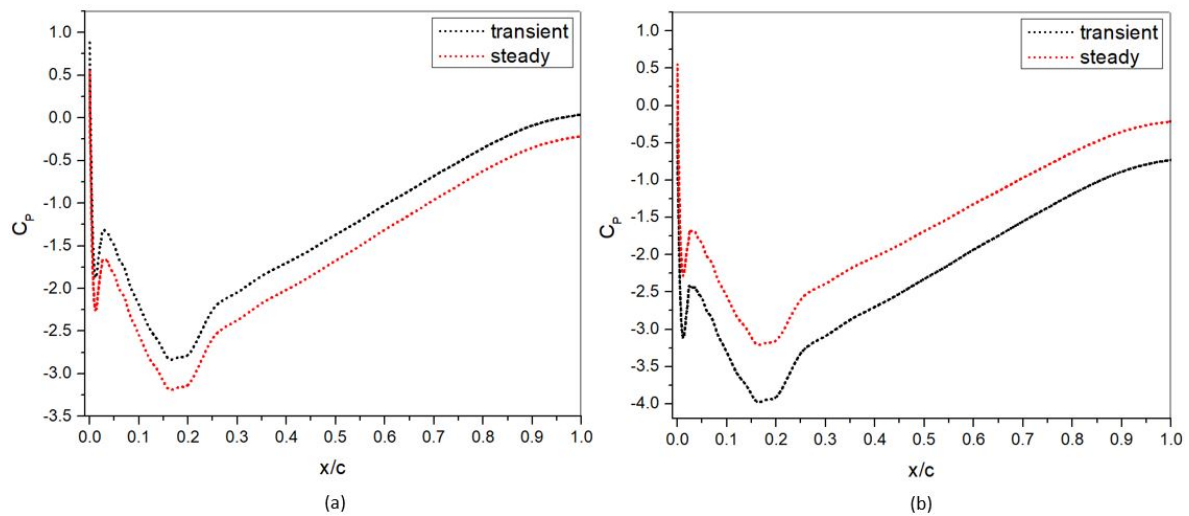


Figure 3-15: (a) Pressure distribution on the airfoil suction side at $t = 3s$ normalized with dynamic pressure $\frac{1}{2}\rho U_\infty^2$ for the accelerating airfoil. The pressure distribution on the suction side is not as low as the pressure distribution at the same velocity under steady state conditions, resulting in a loss of the downforce. (b) Pressure distribution on the airfoil suction side at $t = 4s$ normalized with dynamic pressure $\frac{1}{2}\rho U_\infty^2$ for the decelerating airfoil. The pressure distribution on the suction side is not as high as the pressure distribution at the same velocity under steady state conditions, resulting in a gain in the downforce.

results in an increase in the downforce and a decrease in the drag force. The reduced(or increased) downforce for the accelerating(or decelerating) airfoil can be attributed to the pressure differences on the airfoil surface.

In the case of the accelerating airfoil, the pressure distribution on the suction side at any given

velocity is not as low as the pressure distribution at the same velocity under the steady-state conditions. Similarly, the pressure distribution on the suction side of the decelerating airfoil at any given velocity is higher than the pressure distribution at the same velocity under steady-state conditions. The instantaneous pressure distribution on the accelerating and decelerating airfoil's suction at $t = 3$ s and $t = 4$ s is compared with the pressure distribution on the airfoil surface at the same steady state velocity is shown in the Figure 3-15.

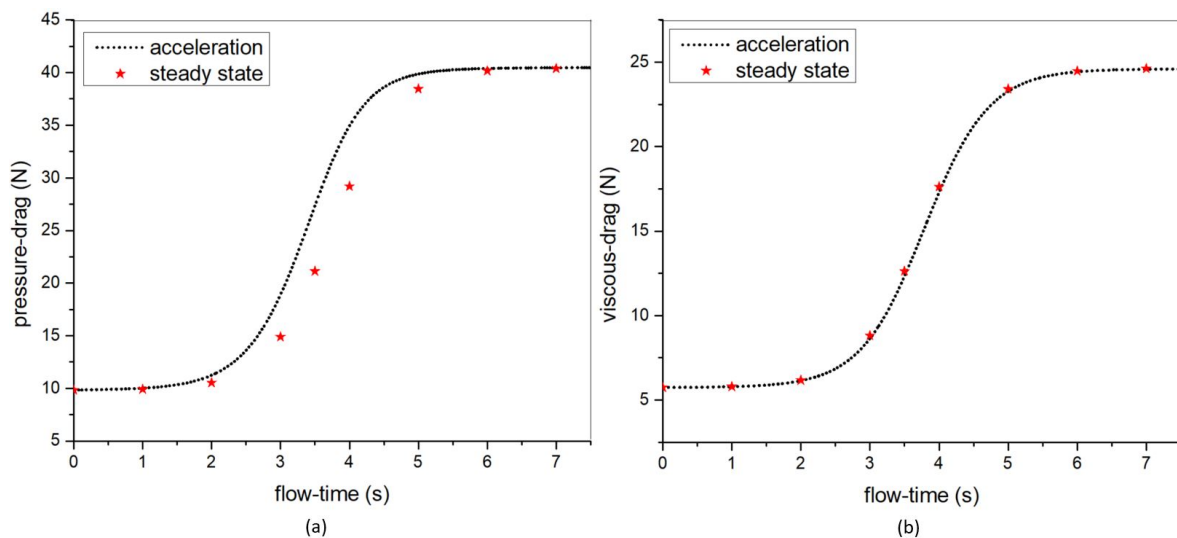


Figure 3-16: (a) Pressure drag and (b) Viscous drag force on the accelerating airfoil at the angle of incidence 3.45° compared with the drag on the airfoil at the same steady state velocities.

In the Figure 3-16, the pressure and viscous drag force on the accelerating airfoil is compared with the pressure and viscous drag at the same steady state velocities. It is evident that, the pressure drag on the accelerating airfoil is higher than that on the airfoil at the same steady state velocities and the viscous drag on the accelerating airfoil is the same as that on the airfoil at the same steady state velocities. The maxima (or minima) observed in the drag force coefficient curves for accelerating (or decelerating) airfoil in Figure 3-12 can be attributed to the added mass effects.

In his discussions, J.N. Newman states that in an ideal flow, a common approximation employed for the added mass coefficient of two-dimensional bodies is the displaced mass of a circle with the same projected width normal to the direction of acceleration [61]. However, it must be noted that the approximation stated by J.N. Newman is valid for two-dimensional bodies in a freestream, unlike the 2D airfoil which is in proximity to the wall (i.e., the ground). An approximate value of the force corresponding to the added mass effects is calculated using the method stated by J.N. Newman, which resulted in a virtual force of 2.0 N at $t = 3.6$ s. From the CFD results in Figure 3-14, it is evident that the virtual force due to the added mass effects at $t = 3.6$ s is ~ 6.0 N, which is higher than the approximation made using the method employed from J.N. Newman. This increased virtual force is consistent with the added mass coefficients in E.H. Kennard [62], where the value of added mass coefficients increase when a 2-dimensional body is translationally accelerated in proximity to a wall.

3-3-2-2 2-Dimensional Airfoil: Ground Clearance $h=0.179c$ & Aspect Ratio=1

Influence of the angle of incidence(AOI) on an accelerating airfoil

Since different racetracks have different downforce requirements, altering the angle of influence of the wing is a common practice followed in the world of motorsports. In order to study the effect of the angle of incidence on the accelerating airfoil, we repeat the same simulation above for the airfoil with increasing angle of incidence in steps of 2.5° . In addition to the default airfoil with an angle of incidence 3.45° , the airfoil with four new angles of incidence 5.95° , 8.45° , 10.95° and 13.45° is accelerated with the non-linear velocity profile in Figure 3-9(a), with the peak acceleration attained at $t = 3.6\text{s}$. As the wing moves through the air, the wing is inclined to the x-direction at some angle. The angle of incidence(AOI) is defined as the angle between the chord line and the x-axis, and has a significant effect on the lift generated by the wing. The effect of an increase in the angle of incidence(AOI) of the wing results in a greater amount of downforce generation, as shown in the Figure 3-17(a). Increasing the angle of incidence has a similar effect on the drag force on the airfoil, as shown in the Figure 3-17(b), where the amount of the drag force increases with increasing angle of incidence(AOI). The increased drag force is a result of the increased frontal area at higher angle of incidences(AOI) and increased flow separation.

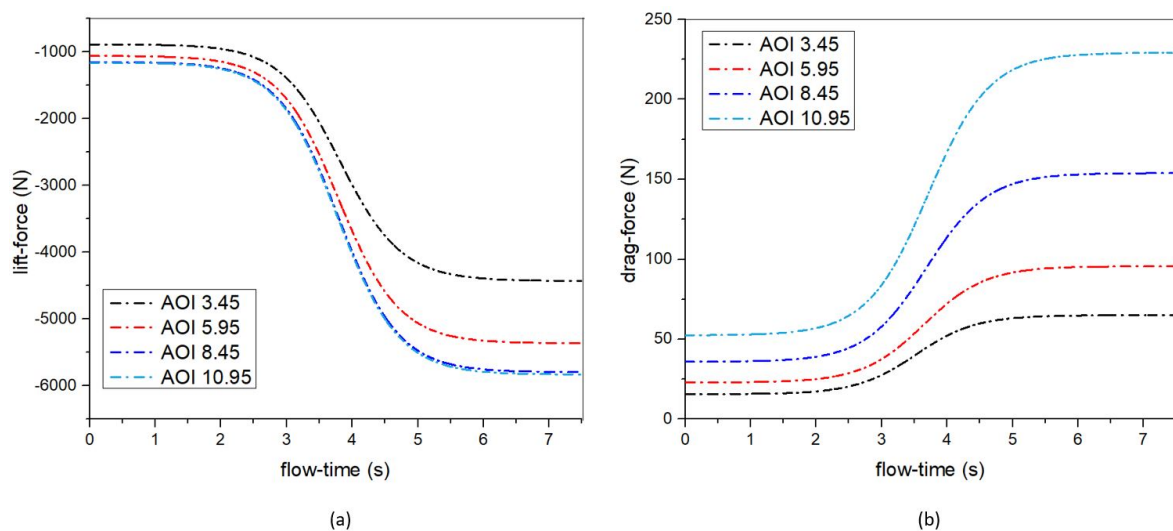


Figure 3-17: (a)Downforce generated by the accelerating airfoil at varying angle of incidences(AOI), (b)Drag force on the accelerating airfoil at varying angle of incidences(AOI). As the angle of incidence is increased, the amount of downforce generated by the airfoil increases. Increased angle of incidence results in an increase in the drag force

For the angle of incidence of 13.45° , vortex shedding is observed at the trailing edge of the airfoil. The flow separated by the airfoil recombines at the trailing edge on the pressure side and the suction side of the airfoil, which results in periodic eddies in the flow field as shown in the Figure 3-18, and induces mechanical vibrations as shown in the Figure 3-19(b). Vortex shedding is a vital phenomenon observed in multiple engineering applications.

At a given angle of incidence and trailing-edge thickness, the Strouhal Number for an airfoil

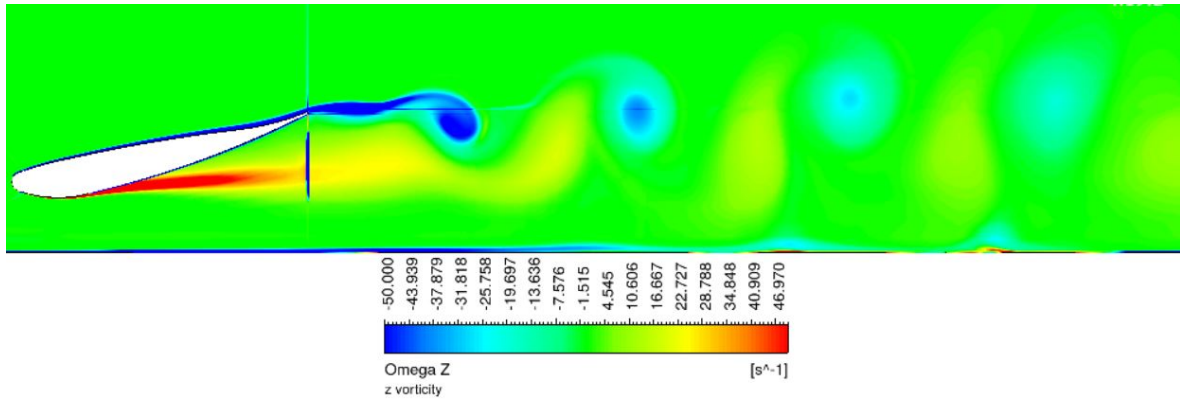


Figure 3-18: Vortex Shedding, indicated by the contours of z-component of vorticity, Ω_z , at the trailing edge of the airfoil at $h/c = 0.179$, as a result of the interaction between the two separated layers on the pressure and suction side of the airfoil

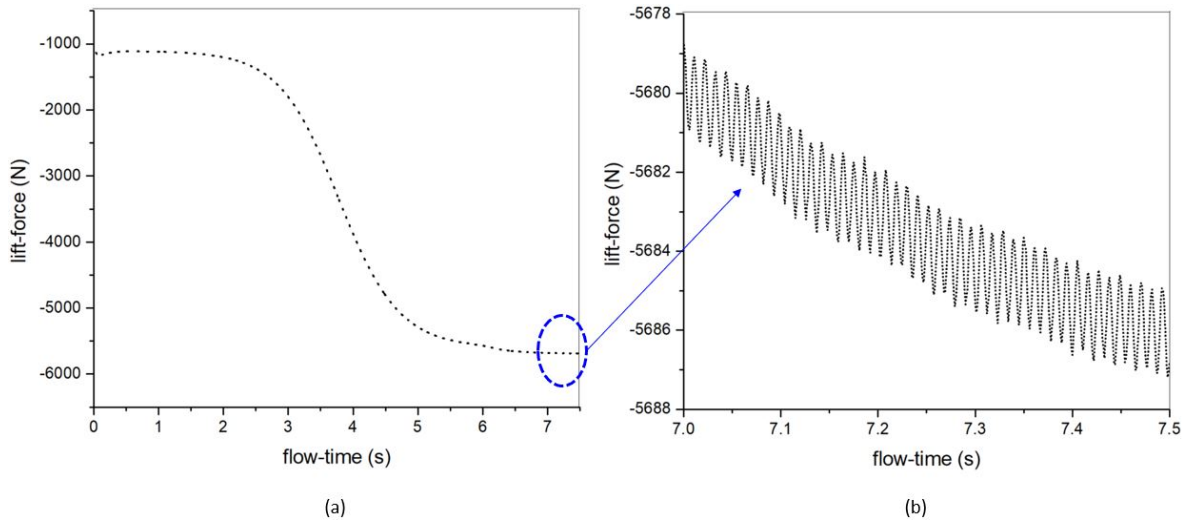


Figure 3-19: (a) Downforce generated by the accelerating airfoil at the angle of incidence, 13.45° and $h/c = 0.179$ for the 2g acceleration profile in Figure 3-9 (b) Downforce oscillations induced by the vortex shedding at trailing edge, with a frequency $f \sim 90$ Hz. For a constant Strouhal number, the shedding frequency varies linearly with the inflow velocity

is a constant and is given by the equation,

$$St = \frac{fc}{U} \tag{3-11}$$

where f is the frequency of shedding, U is the inflow velocity and c is the chord length of the airfoil. At high angles of incidences(AOI), if the shedding frequency of the airfoil interferes with the natural frequency of the racecar’s suspension, the imbalance caused by the vortex shedding can be felt by the other components on the car. In this instance, from the Figure 3-9(b), it is evident that the periodic variations in the downforce generated by the airfoil is minimal at the angle of incidence 13.45° . The frequency of the shedding depends on multiple factors, namely; the inflow velocity, the angle of incidence and the trailing-edge thickness of the airfoil. Since the main aim of the research is to investigate the influence of translational

acceleration (and deceleration) on the forces generated by the airfoil, detailed investigations on the factors that influence the vortex shedding frequency are not performed.

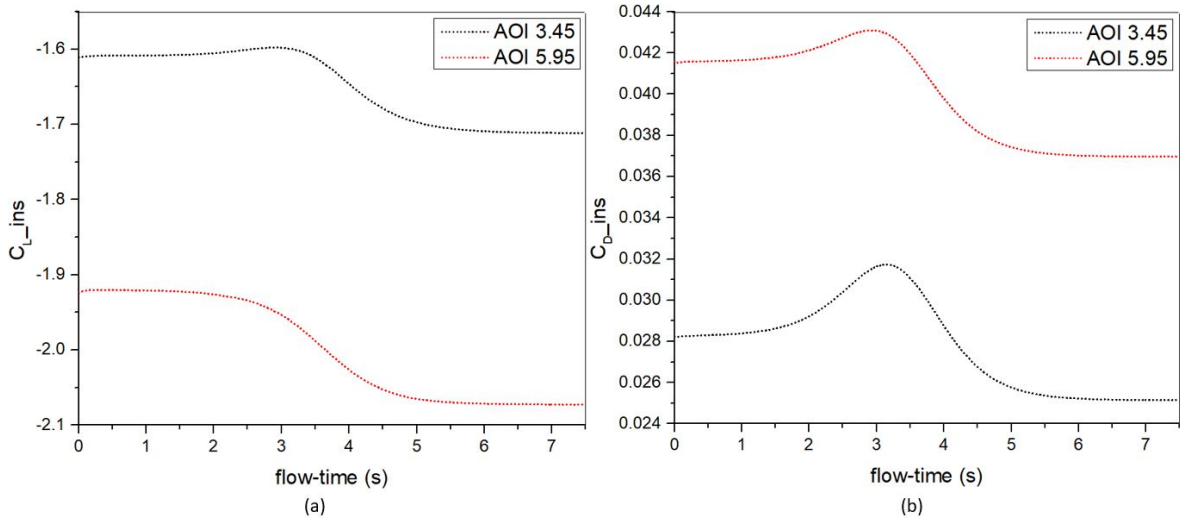


Figure 3-20: (a) Downforce coefficient for the accelerating airfoil at angles of incidences 3.45° and 5.45°, (b) Drag force coefficient for the accelerating airfoil at angles of incidences 3.45° and 5.45°

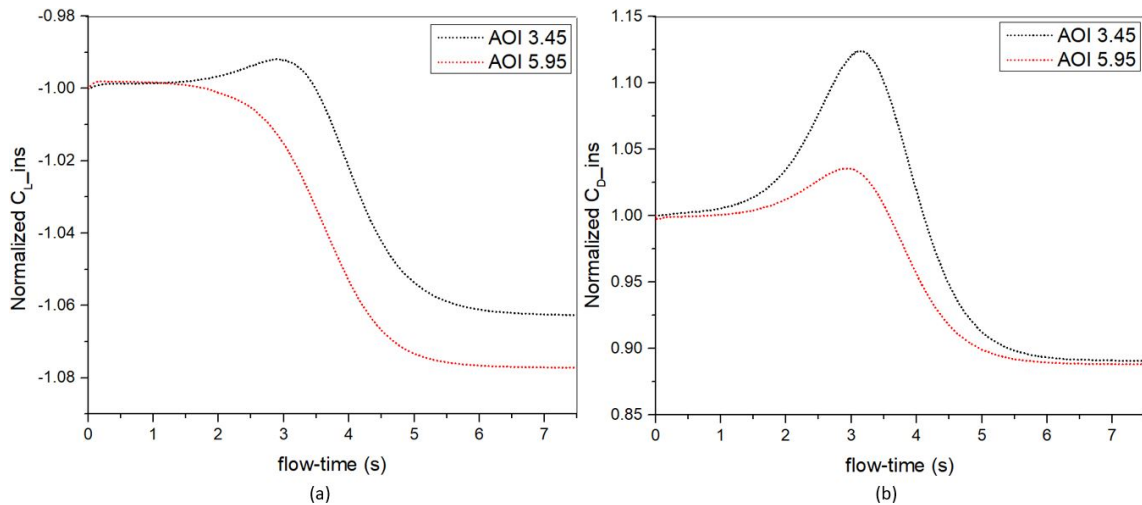


Figure 3-21: (a) Normalized downforce coefficient for the accelerating airfoil at angles of incidences 3.45° and 5.45°, (b) Normalized drag coefficient for the accelerating airfoil at angles of incidences 3.45° and 5.45°. The normalized force coefficients indicate that the accelerating airfoil at the angle of incidence 3.45° is influenced by the acceleration more than the accelerating airfoil at the angle of incidence 5.95°

To investigate the influence of the angle of incidence (AOI) on the downforce generated by the accelerating airfoil and the drag force it experiences, we study the behavior of the instantaneous force coefficients, i.e., the forces non-dimensionalized with the instantaneous free stream velocity using the Equation 3-10. We consider two angles of incidence for this study, 3.45° and 5.45°. The downforces and the drag forces in the Figure 3-17 for the angles of incidence

3.45° and 5.45° are non-dimensionalized using the Equation 3-10. The plots in Figure 3-20 reveal the variations in the instantaneous force coefficients for the accelerating airfoil at two different angles of incidence, 3.45° and 5.45° . These instantaneous force coefficients are then normalized with the force coefficient at $t = 0.0$ s in the Figure 3-21. The plots in the Figure 3-21 reveal that the accelerating airfoil at the angle of incidence 3.45° experiences a minimum indicated by the $\sim 1\%$ loss in downforce coefficient (i.e., $-C_L$), and the drag force coefficient on it reveals a maximum indicated by $\sim 10\%$ gain. Meanwhile, the accelerating airfoil at the angle of incidence 5.45° experiences no loss in downforce coefficient (i.e., $-C_L$) and the drag force coefficient reveals a maximum shown by $\sim 2\%$ increase.

In order to understand the differences in the behavior of the normalized downforce coefficient plots, we compare the steady state downforce generated by the airfoil at the same velocities as the accelerating airfoil at the angles of incidence 3.45° and 5.45° .

For the airfoil at the angle of incidence 3.45° , the downforce curves in Figure 3-13 reveal that, when compared to the steady state downforces generated by the airfoil at the same velocities as the accelerating airfoil, the accelerating airfoil experiences a loss of downforce. Similarly, for the airfoil at the angle of incidence 5.95° , the downforce curves in the Figure 3-22 reveal that, when compared to the steady state downforces generated by the airfoil at the same velocities as the accelerating airfoil, the accelerating airfoil experiences a loss of downforce. However, the loss of the downforce for an accelerating airfoil at the angle of incidence 5.95° is significantly lower than the airfoil accelerated at the angle of incidence 3.45° .

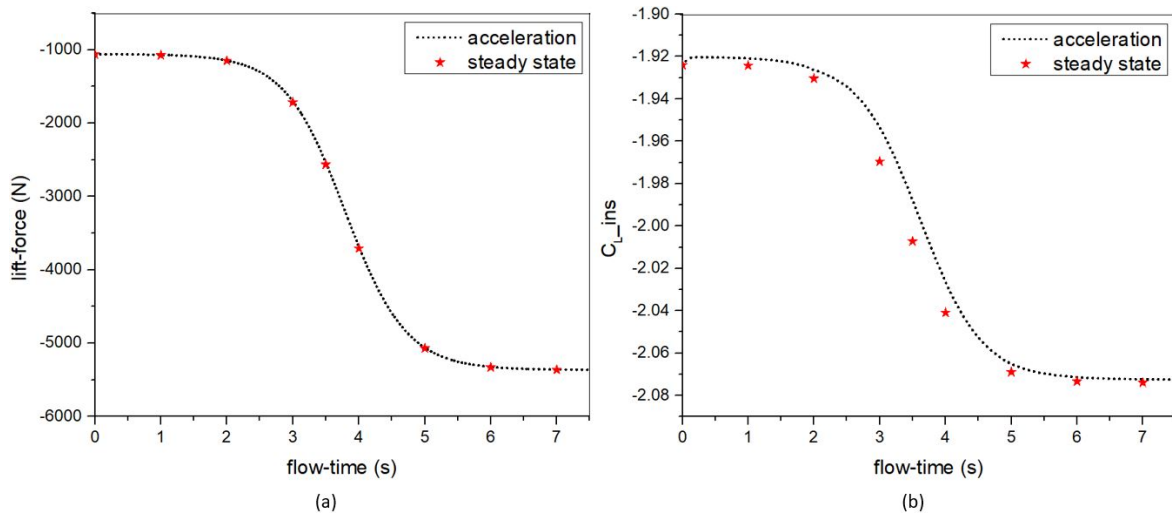


Figure 3-22: (a) Downforce generated by the accelerating airfoil at the angle of incidence 5.95° , (b) Downforce coefficient for the accelerating airfoil at the angle of incidence 5.95° . The downforce coefficients indicate that the accelerating airfoil experiences a 1% loss in downforce when compared to the airfoil at the same steady state velocity at $t = 3$ s

For the airfoil at the angle of incidence 3.45° , the drag force curves in the Figure 3-14 reveal that, when compared to the steady state drag forces on the airfoil at the same velocities as the accelerating airfoil, the accelerating airfoil experiences an increase in the drag force. Similarly, for the airfoil at the angle of incidence 5.95° , the drag force curves in the Figure 3-23 reveal that, when compared to the steady state drag forces on the airfoil at the same velocities as the accelerating airfoil, the accelerating airfoil experiences a loss of downforce.

However, the increase in the drag force for an accelerating airfoil at the angle of incidence 5.95° is significantly lower than the airfoil accelerated at the angle of incidence 3.45° .

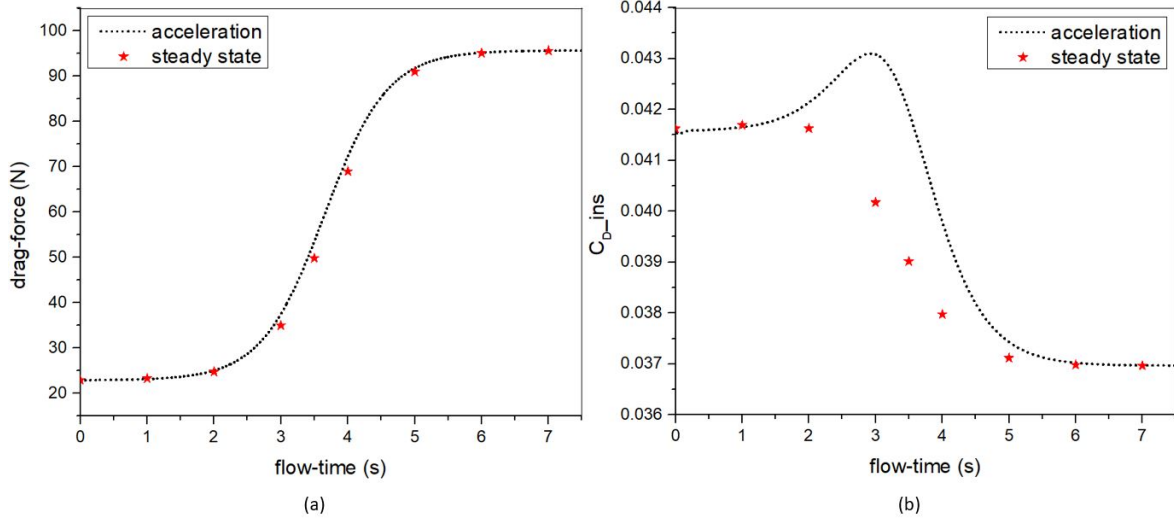


Figure 3-23: (a) Drag force on the accelerating airfoil at the angle of incidence 5.95° , (b) Drag force coefficient for the accelerating airfoil at the angle of incidence 5.95° . The drag force coefficients indicate that the accelerating airfoil experiences a 14% increase in the drag force when compared to the airfoil at the same steady state velocity at $t = 3$ s.

From the Figures 3-13, 3-22, 3-14 and 3-23, it is evident that the influence of the acceleration on the forces for airfoil at the angle of incidence 3.45° is higher than the airfoil at the angle of incidence 5.95° .

Further investigations into the influence of acceleration on the airfoils at the angles of incidences 3.45° and 5.95° are performed by comparing the local acceleration effects on the airfoils at the two different angles of incidences. From the Equation 1-14, the x-momentum equation for a 2-dimensional accelerating airfoil in the non-inertial frame is,

$$\rho \left(\underbrace{\frac{\partial u}{\partial t}}_{LA} + \underbrace{u \frac{\partial u}{\partial x} + v \frac{\partial u}{\partial y}}_{CA} \right) = -\frac{\partial p}{\partial x} + \mu \left(\frac{\partial^2 u}{\partial x^2} + \frac{\partial^2 u}{\partial y^2} \right) - \underbrace{\rho \frac{\partial V(x)}{\partial t}}_{TA} \quad (3-12)$$

In the equation above, the term “LA” corresponds to the local acceleration of the fluid element. The non-linear convection terms in the x-momentum equation above correspond to the convective acceleration encountered by the airfoil, i.e., “CA” and the term “TA” corresponds to the translational acceleration of the airfoil. Contours of convective acceleration (“CA”) are plotted for the 2-dimensional airfoil at the angles of incidences 3.45° and 5.95° and the convective acceleration encountered by the airfoil at $x/c = 0.0$, $x/c = 0.2$ and $x/c = 0.4$ is measured using probes as shown in the Figure 3-25. The instantaneous convective acceleration contour for the accelerating airfoil at the angle of incidence 3.45° is illustrated in the Figure 3-24 at $t = 3.0$ s. The convective acceleration contour for the accelerating airfoil at the angle of incidence 5.95° is similar to that in the Figure 3-24 with the magnitude of convective acceleration being different.

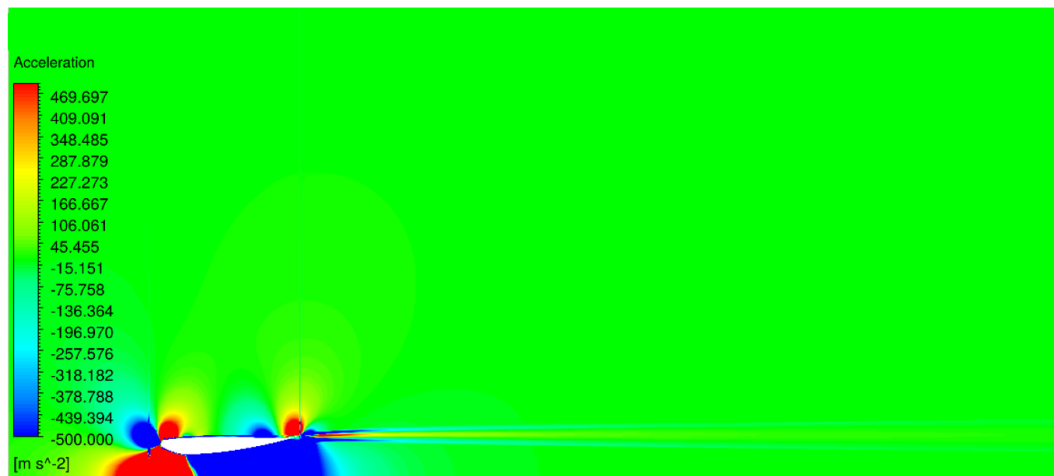


Figure 3-24: Convective acceleration contour for the translationally accelerating airfoil at the angle of incidence 3.45° at $t = 3.0$ s.

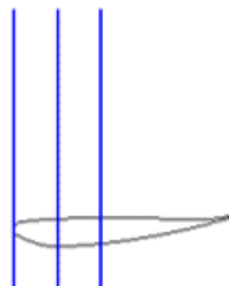


Figure 3-25: Locations of the probes used to measure the convective acceleration encountered by the translationally accelerating airfoil at $x/c = 0.0$, $x/c = 0.2$ and $x/c = 0.4$

Since the peak translational acceleration achieved by the accelerating airfoil is at $t = 3.6$ s, we measure the instantaneous convective acceleration encountered by the translationally accelerating airfoil at the locations in the Figure 3-25 at $t = 3.0$ s, $t = 3.6$ s and $t = 4.0$ s.

The Figures 3-26, 3-27, 3-28, 3-29, 3-30 and 3-31 illustrate the convective acceleration encountered by the translationally accelerating airfoils at the two different angles of incidences, 3.45° and 5.95° . On comparing the magnitude of convective accelerations encountered by the translationally accelerating airfoil at two different angles of incidence, it is evident that the translationally accelerating airfoil at the higher angle of incidence, i.e. 5.95° , encounters higher magnitude of convective acceleration when compared to that encountered by the translationally accelerating airfoil at the lower angle of incidence, i.e. 3.45° . As a result, the influence of the translational acceleration on the forces is less for the translationally accelerating airfoil at a higher angle of incidence, i.e., 5.95° when compared to the influence of the translational acceleration on the forces for the translationally accelerating airfoil at a lower angle of incidence, i.e., 3.45° . This is reflected in the normalized force coefficient plots for translationally accelerating airfoil at the two different angles of incidences, in the Figure 3-21.

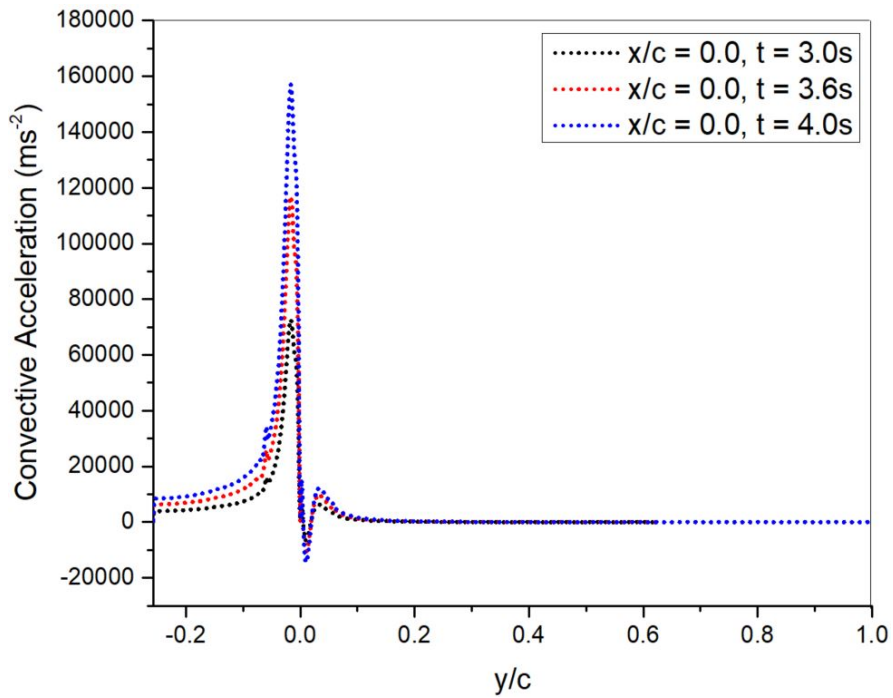


Figure 3-26: Instantaneous convective acceleration encountered by the translationally accelerating airfoil at the angle of incidence 3.45° at the probe location $x/c = 0.0$.

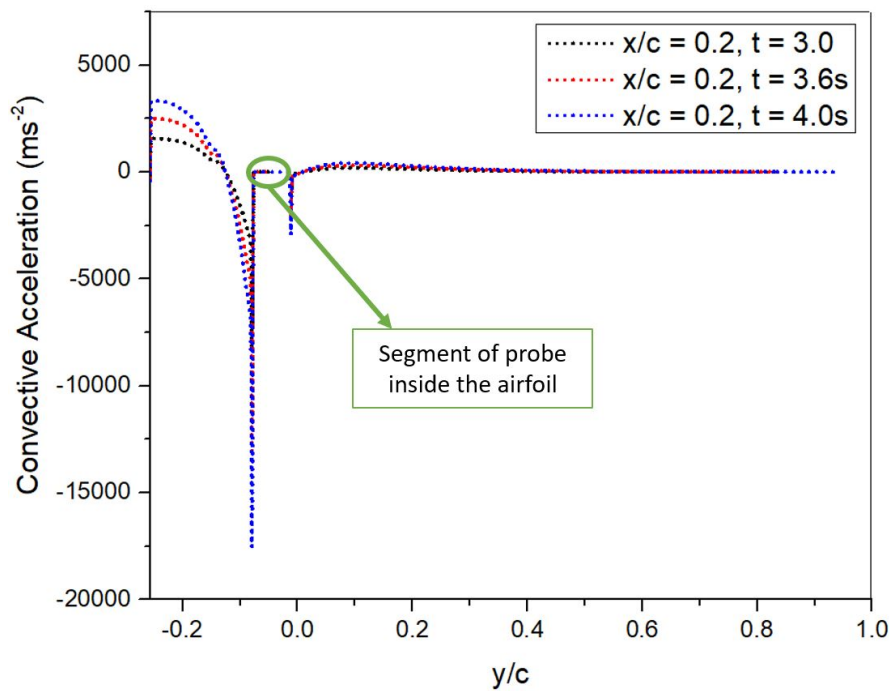


Figure 3-27: Variation of the non-dimensional term 3 in the Equation 3-4 during the course of acceleration

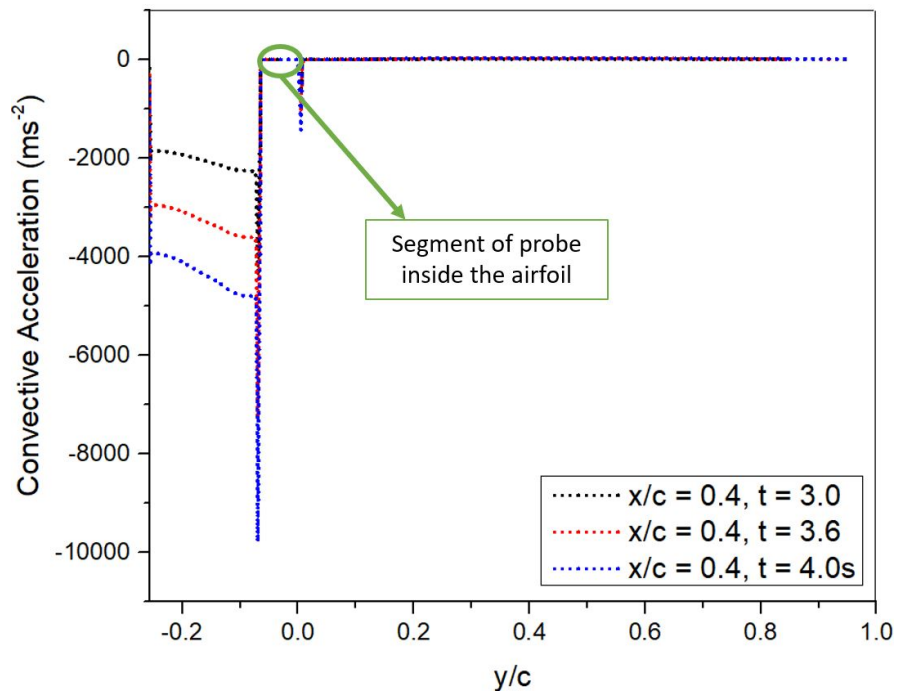


Figure 3-28: Instantaneous convective acceleration encountered by the translationally accelerating airfoil at the angle of incidence 3.45° at the probe location $x/c = 0.4$

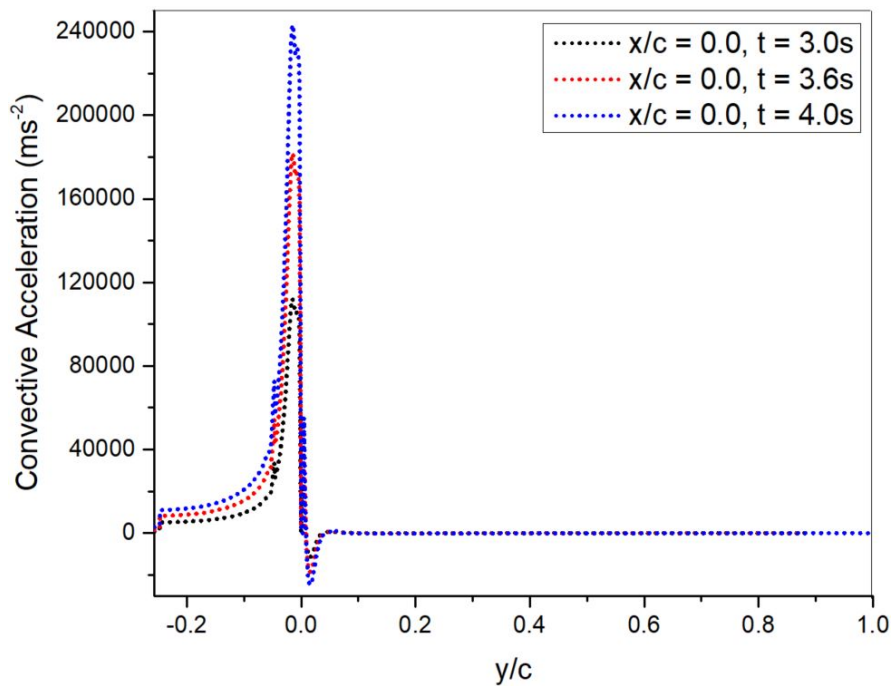


Figure 3-29: Instantaneous convective acceleration encountered by the translationally accelerating airfoil at the angle of incidence 5.95° at the probe location $x/c = 0.0$

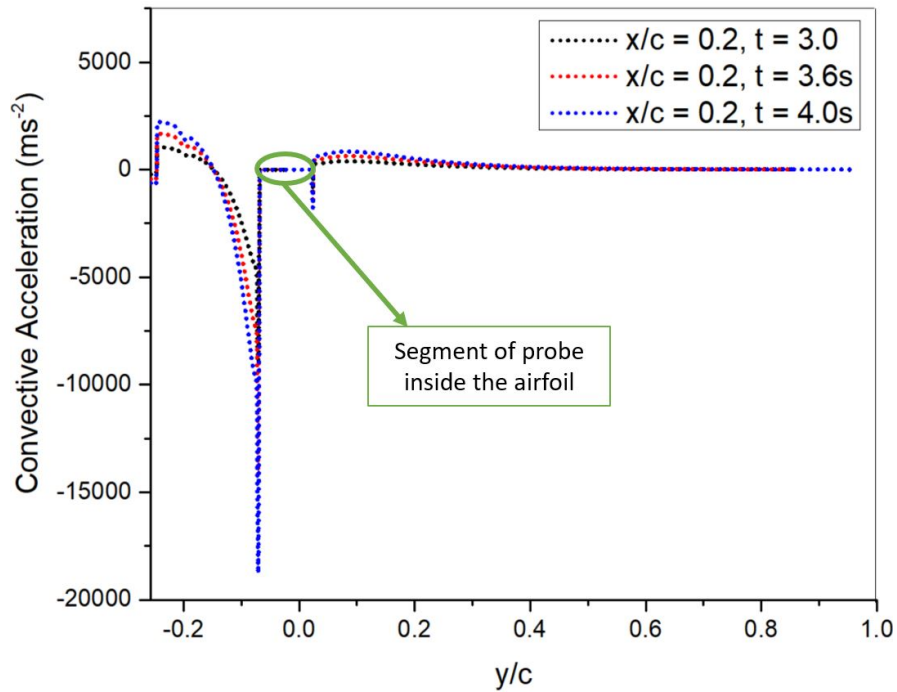


Figure 3-30: Instantaneous convective acceleration encountered by the translationally accelerating airfoil at the angle of incidence 5.95° at the probe location $x/c = 0.2$

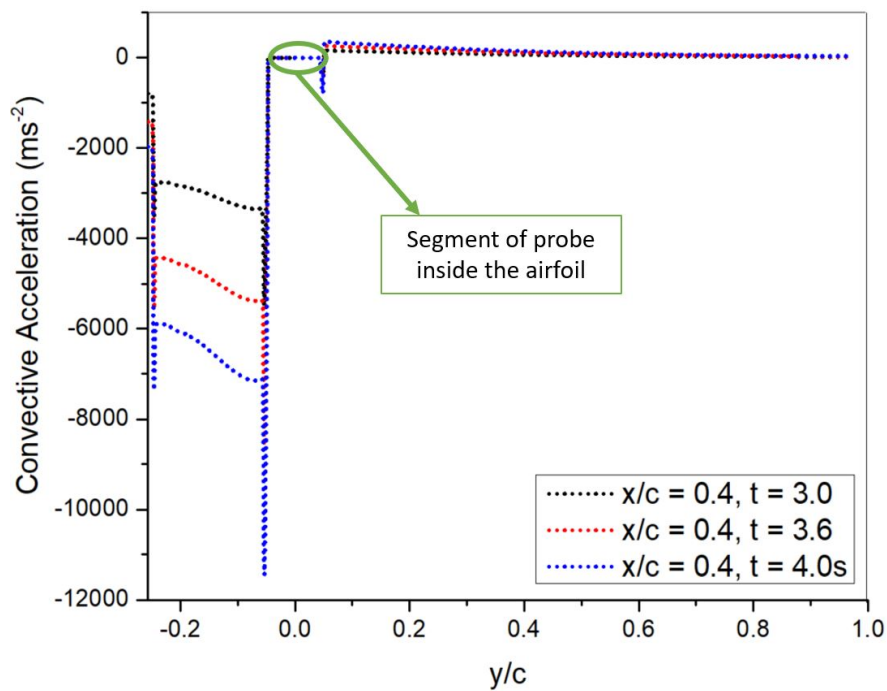


Figure 3-31: Instantaneous convective acceleration encountered by the translationally accelerating airfoil at the angle of incidence 5.95° at the probe location $x/c = 0.4$

3-3-2-3 2-Dimensional Airfoil: Ground Clearance $h=0.179c$ & Aspect Ratio=1

Influence of magnitude of acceleration(or deceleration) on the downforce and the drag force

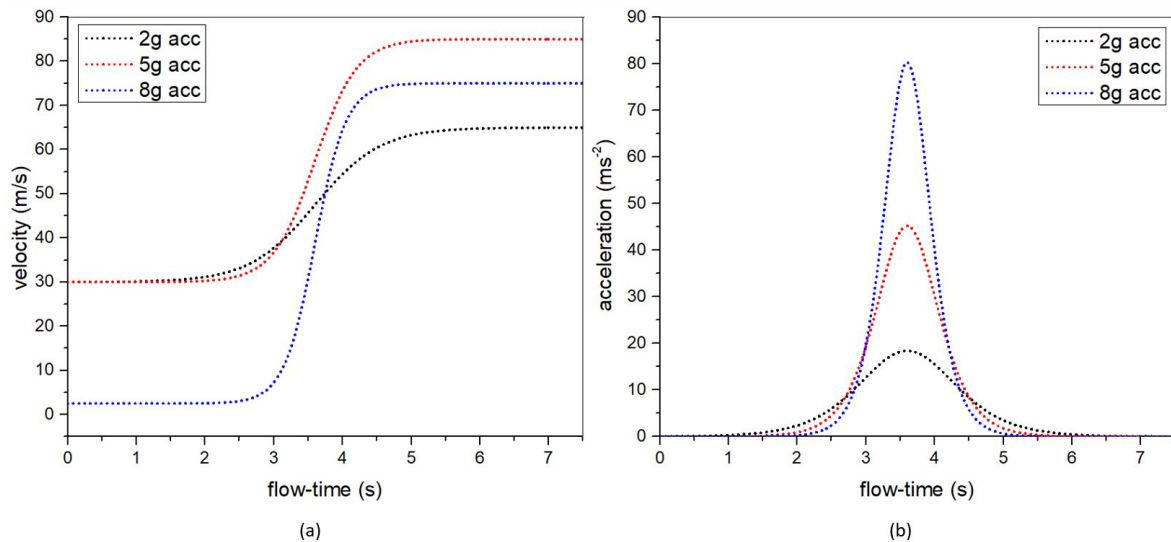


Figure 3-32: (a) Velocity profiles for the accelerating airfoil generated using the Equation 2-2, (b) Corresponding acceleration profiles for the accelerating airfoil.

To investigate the influence of the magnitude of acceleration on the aerodynamic forces, the 2-dimensional airfoil with a unit chord length, a ground height $h = 0.179c$, an angle of incidence 3.45° and an aspect ratio 1 is accelerated with three different velocity profiles in the Figure 3-32(a). In all the three instances, the airfoil is accelerated for a time $t = 7.5s$. In the Figure 3-32(a), it can be seen that initial velocities, i.e., $V(t = 0)$ for the '2g' and '5g' acceleration cases are identical, while the initial velocity for the '8g' acceleration case is lower than that in the '2g' and '5g' acceleration. A lower starting velocity was chosen for the '8g' acceleration case, since the final velocity, i.e., $V(t = 7.5)$ attained, needs to be a value which lies in the range of speed that a race car operates in, i.e., 0-330 kmph.

The three different non-linear velocity profiles are generated using the Equation 2-2 to resemble the velocity profiles encountered on a racetrack. The acceleration profiles corresponding to these acceleration profiles are shown in the Figure 3-32(b), with the peak acceleration values attained at $t = 3.6s$. Based on the peak values of acceleration achieved, the velocity profiles are classified into three different categories, namely: the 2g acceleration case ($\sim 20 m/s^2$), the 5g acceleration case ($\sim 50 m/s^2$) and the 8g acceleration case ($\sim 80 m/s^2$). The 2g and the 5g acceleration cases are something that a race car typically encounters on a racetrack, while the 8g acceleration case is something that is rarely encountered on a racetrack. For the 2g acceleration scenario, the chord Reynolds number for the accelerating airfoil varies from 2.0×10^6 to 4.4×10^6 . For the 5g acceleration scenario, the chord Reynolds number for the accelerating airfoil varies from 2.0×10^6 to 5.8×10^6 . For the 8g acceleration scenario, the chord Reynolds number for the accelerating airfoil varies from 1.7×10^5 to 5.1×10^6 .

The downforce generated by the accelerating profile and the drag force it experiences for all

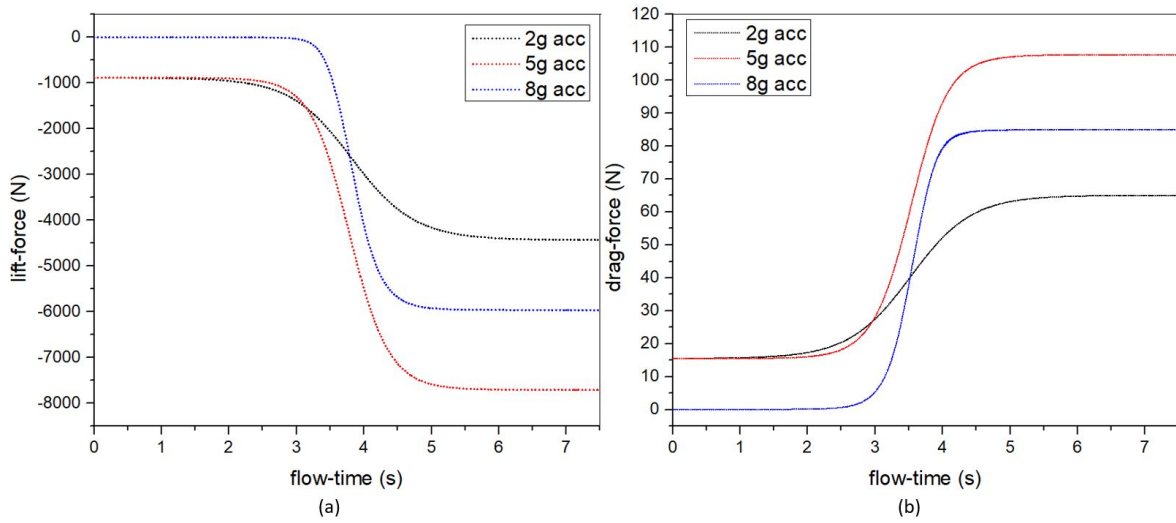


Figure 3-33: (a) Downforces generated by the accelerating airfoil for the three different velocity profiles in the Figure 3-32, (b) Drag force on the accelerating airfoil for the three different velocity profiles in the Figure 3-32

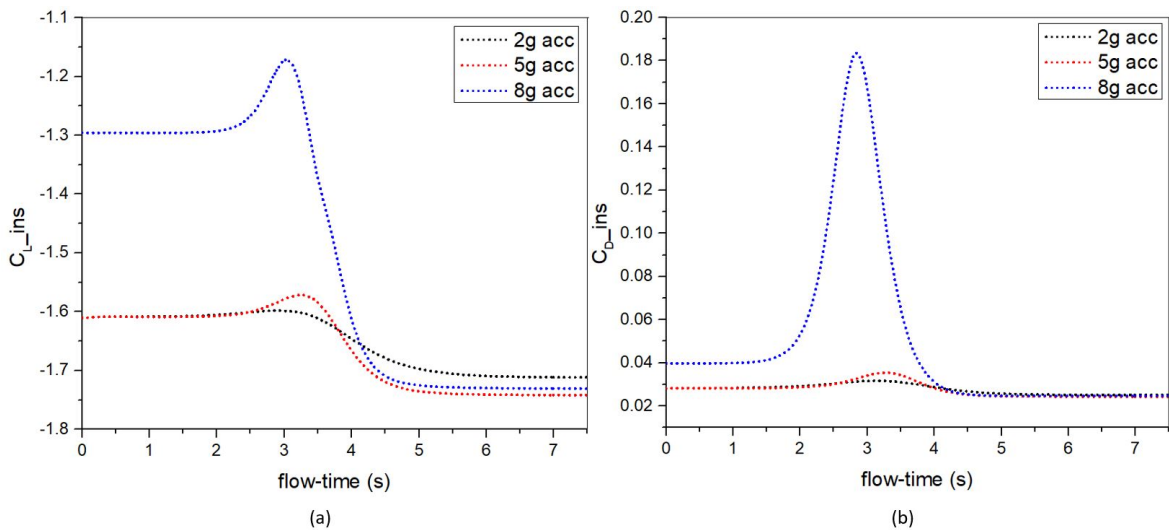


Figure 3-34: (a) Downforce coefficient for the accelerating airfoil for the three different velocity profiles in the Figure 3-32, (b) Drag force coefficient for the accelerating airfoil for the three different velocity profiles in the Figure 3-32. The force coefficient curves exhibit the influence of magnitude of acceleration for the accelerating airfoil.

the three different velocity profiles in the Figure 3-32(a), is shown in the Figure 3-33. The non-dimensionalized forces using the Equation 3-10 are plotted in the Figure 3-34.

The normalized force coefficients for the accelerating airfoil with the peak acceleration value of 2g, 5g and 8g are plotted in the Figures 3-35, 3-36 and 3-37 respectively. The Figure 3-35 reveals that the airfoil accelerated with a peak acceleration value of 2g undergoes a 1% loss in the downforce coefficient and encounters a 12% gain in the drag force coefficient. The Figure 3-36 reveals that the airfoil accelerated with a peak acceleration value of 5g undergoes a 3%

loss in the downforce coefficient and encounters a 25% gain in the drag force coefficient. The Figure 3-37 reveals that the airfoil accelerated with a peak acceleration value of 8g undergoes a 10% loss in the downforce coefficient and encounters a 450% gain in the drag force coefficient.

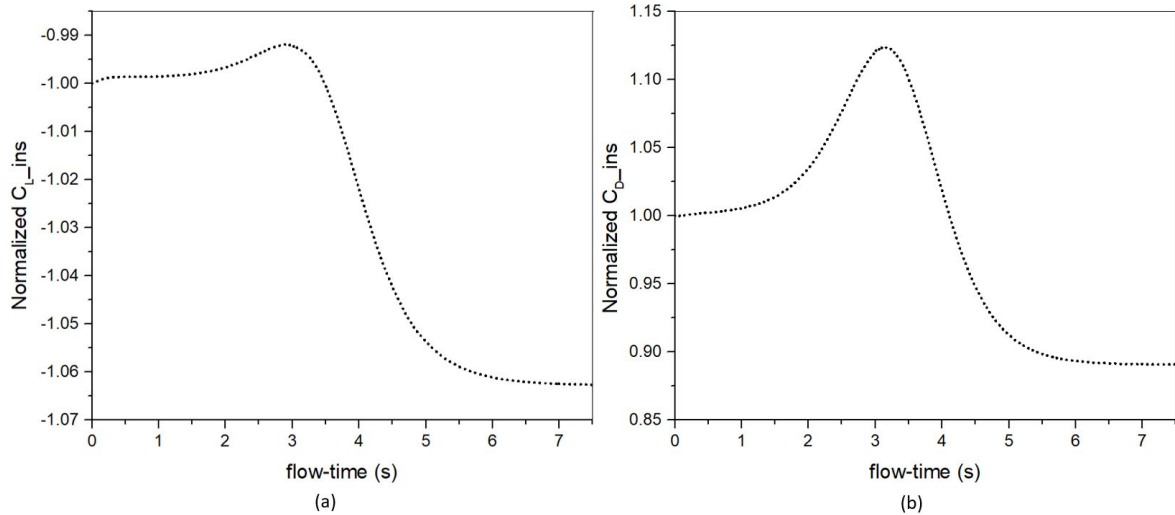


Figure 3-35: (a) Normalized downforce coefficient for the accelerating airfoil with the peak acceleration value 2g, (b) Normalized drag force coefficient for the accelerating airfoil with the peak acceleration value 2g. The normalized force coefficients indicate that the accelerating airfoil undergoes a 1% loss in the downforce and encounters a 12% gain in the downforce.

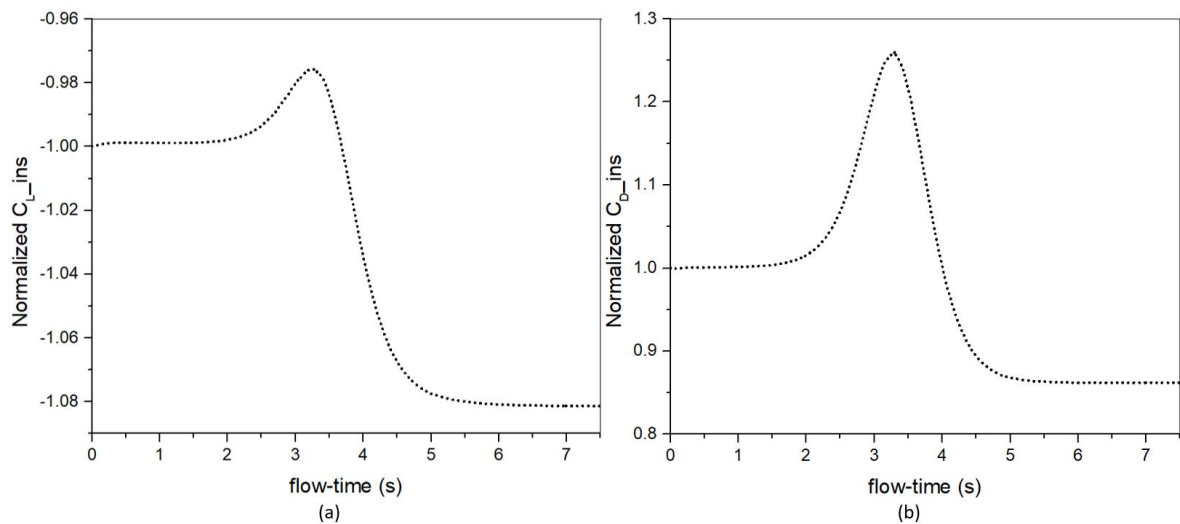


Figure 3-36: (a) Normalized downforce coefficient for the accelerating airfoil with the peak acceleration value 5g, (b) Normalized drag force coefficient for the accelerating airfoil with the peak acceleration value 5g. The normalized force coefficients indicate that the accelerating airfoil undergoes a 3% loss in the downforce and encounters a 25% gain in the drag force.

Further investigations on the influence of magnitude of the translational acceleration on the forces are carried out by comparing the magnitude of convective acceleration encountered by

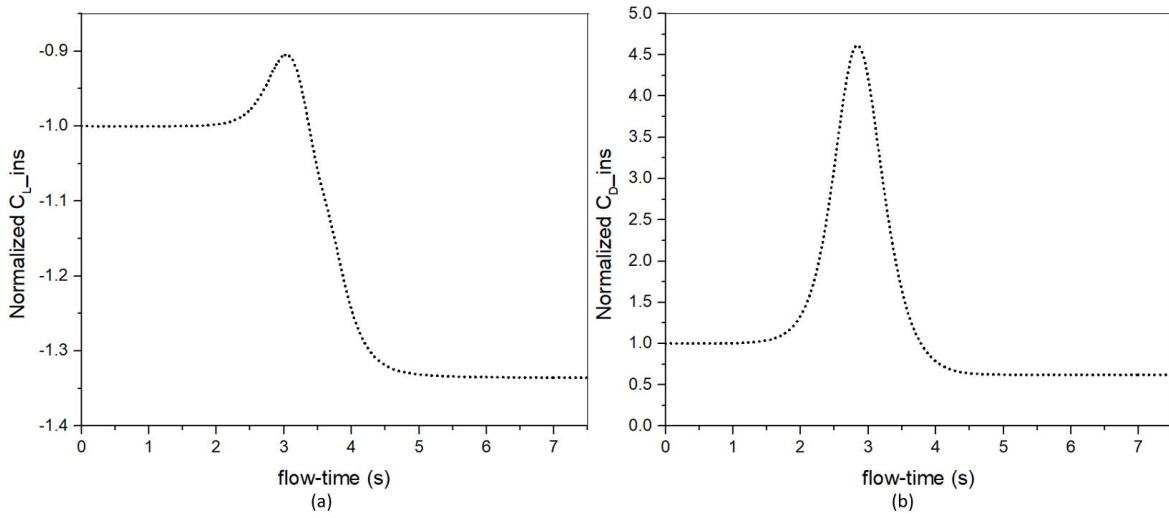


Figure 3-37: (a) Normalized downforce coefficient for the accelerating airfoil with the peak acceleration value 8g, (b) Normalized drag force coefficient for the accelerating airfoil with the peak acceleration value 8g. The normalized force coefficients indicate that the accelerating airfoil undergoes a 10% loss in the downforce and encounters a 450% gain in the drag force.

the accelerating airfoil. The convective acceleration encountered by the translationally accelerating airfoil is determined using the non-linear term in the Equation 3-12. The convective acceleration encountered by the accelerating airfoil at different values of peak acceleration is shown in the Figure 3-39.

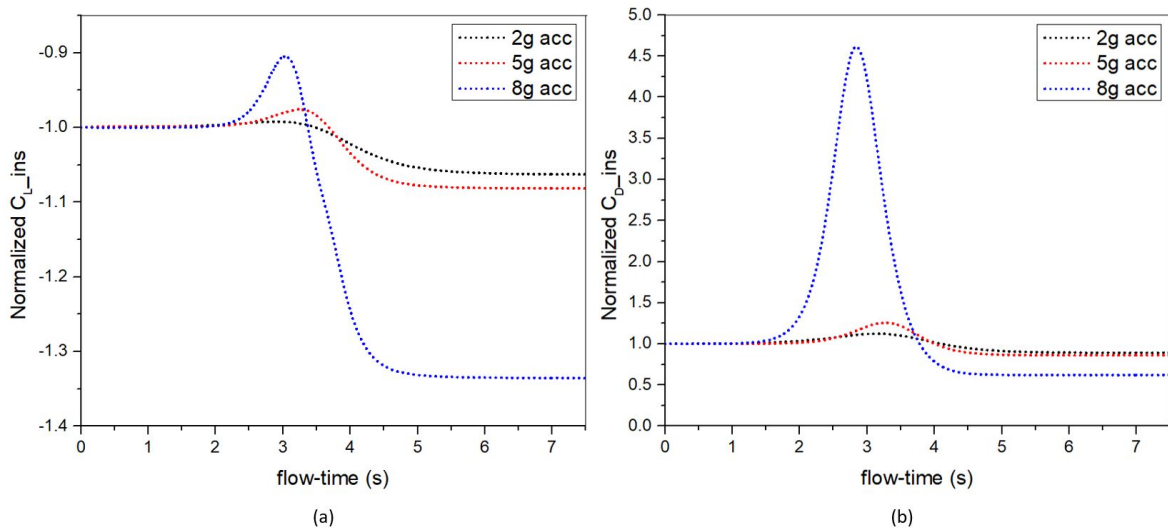
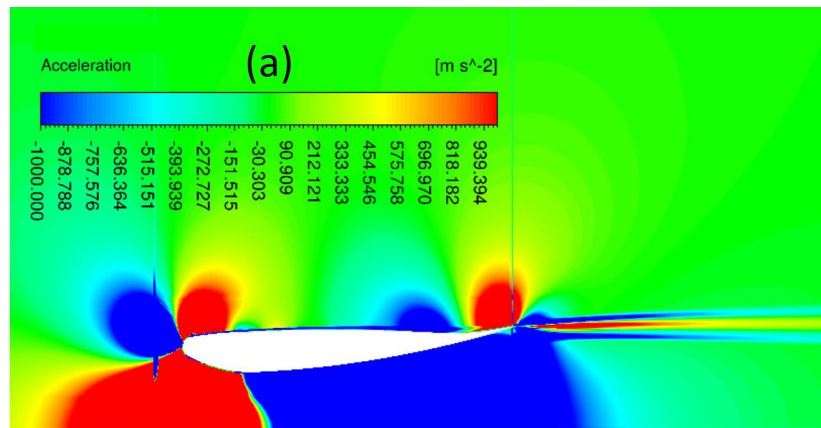
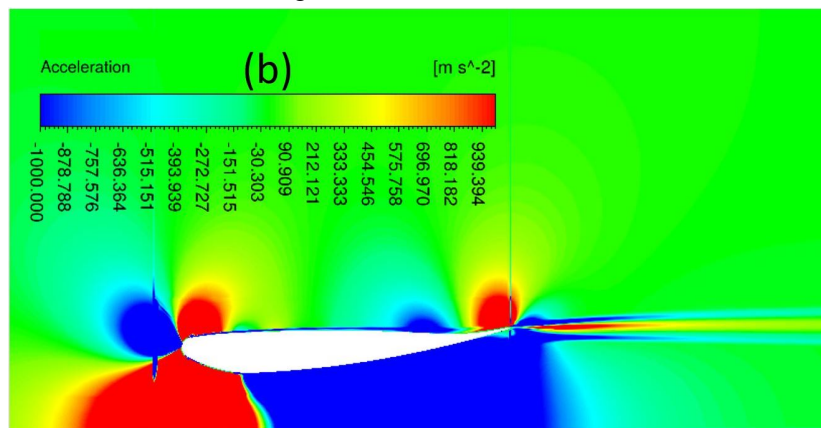


Figure 3-38: (a) Normalized downforce coefficient for the accelerating airfoil with varying peak acceleration values, (b) Normalized drag force coefficient for the accelerating airfoil with varying peak translational acceleration values. The normalized coefficient curves indicate that the higher the magnitude of acceleration, the higher is the influence of acceleration on the forces.

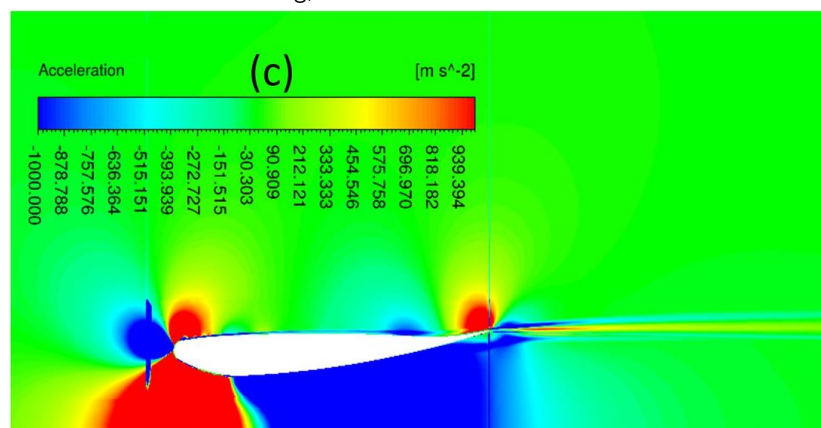
The contours in the Figure 3-39 reveal that, the magnitude of convective acceleration encountered by the airfoil accelerated with a 2g translational acceleration is higher than that



(a) Convective acceleration encountered by the accelerating airfoil at peak translational acceleration value $2g$, $t = 3.6s$



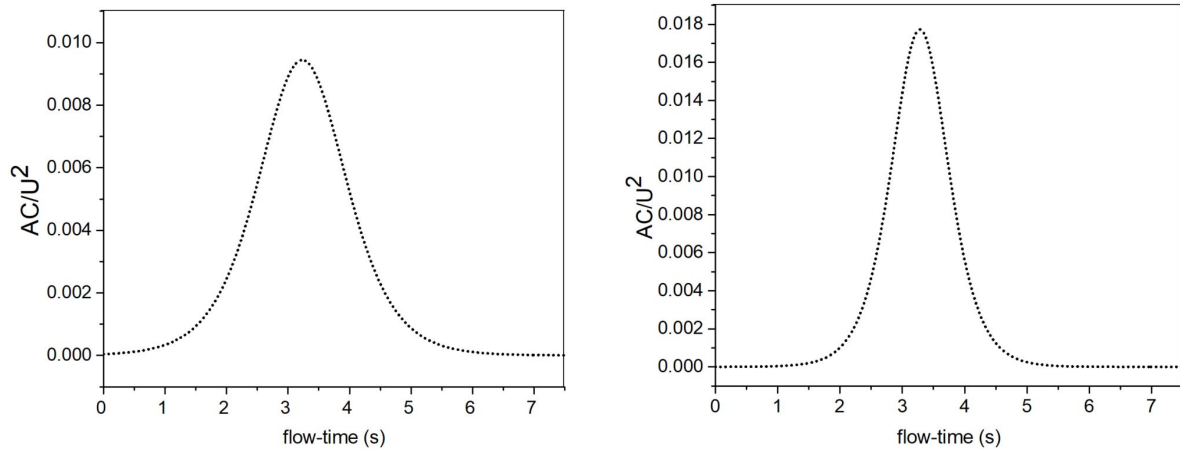
(b) Convective acceleration encountered by the accelerating airfoil at peak translational acceleration value $5g$, $t = 3.6s$



(c) Convective acceleration encountered by the accelerating airfoil at peak translational acceleration value $8g$, $t = 3.6s$

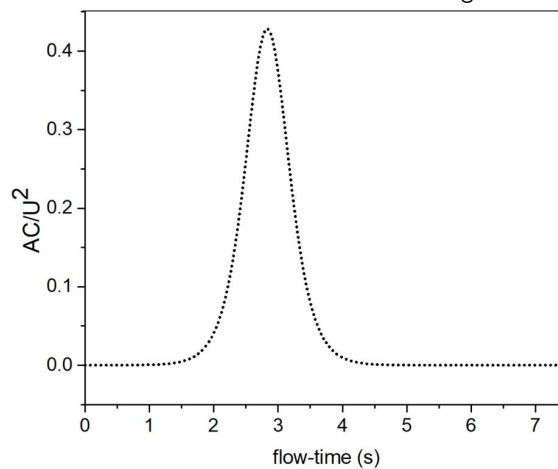
Figure 3-39: Convective acceleration contours encountered at three different peak values of translational acceleration. The lower the value of peak translational acceleration, the higher the magnitude of convective acceleration encountered by the translationally accelerating airfoil.

encountered by the airfoil accelerated with a 8g translational acceleration. As a result, the influence of the translational acceleration on the downforce and drag force for the translationally accelerating airfoil is lowest for the peak translational acceleration value 2g and highest for the peak translational acceleration value 8g. This is reflected in the normalized force coefficient curves in the Figure 3-38, where the influence of the acceleration on the forces is highest for the peak value of acceleration 8g and lowest for the peak value of acceleration 2g.



(a) Variation of the non-dimensional *Term 3* in the Equation 3-4 when the airfoil is subjected to a peak acceleration 2g

(b) Variation of the non-dimensional *Term 3* in the Equation 3-4 when the airfoil is subjected to a peak acceleration 5g



(c) Variation of the non-dimensional *Term 3* in the Equation 3-4 when the airfoil is subjected to a peak acceleration 8g

Figure 3-40: Variation of the non-dimensional *Term 3* in the Equation 3-4 when the airfoil is subjected to different values of peak translational acceleration. These plots reveal the magnitude of the *Term 3* when compared to the non-linear term corresponding to the convective acceleration encountered by the translationally accelerating airfoil, which is of order 1, from the Equation 3-4.

Further investigations on the behavior of the force coefficient curves in the Figure 3-38 in response to the different magnitudes of accelerations imposed is performed using the non-dimensional terms in the Equation 3-4. For the accelerating airfoil in the Section 3-3-2-3, the chord length scale C is 1m. The curves in the Figures 3-40a, 3-40b and 3-40c show the

variation of the *Term 3*, i.e., AC/U^2 over the course of acceleration.

The non-dimensional AC/U^2 in the Figure 3-40a reveal that, at the peak, the magnitude of AC/U^2 is ~ 100 times lower than the convective acceleration encountered by the accelerating airfoil. The non-dimensional AC/U^2 in the Figure 3-40b reveal that, at the peak, the magnitude of AC/U^2 is ~ 50 times lower than the convective acceleration encountered by the accelerating airfoil. The non-dimensional AC/U^2 in the Figure 3-40c reveal that, at the peak, the magnitude of AC/U^2 is ~ 2 times lower than the convective acceleration encountered by the accelerating airfoil. This is consistent with the normalized force coefficient curves in the Figure 3-38. The higher the convective acceleration encountered by the accelerating airfoil when compared to AC/U^2 , the lower is the influence of the translational acceleration on the forces.

Realistic velocity and acceleration profiles are employed to accelerate and decelerate the airfoil. We utilize the velocities captured at various locations on the track from the Figure 3-42 to arrive at the starting and end velocities. Based on the velocities in Figure 3-42, the racecar decelerates from a velocity of 85 m/s to 30 m/s as it approaches Turn 1 and then accelerates from a velocity of 30 m/s to 65 m/s as it accelerates from Turn 1. In order to match these values of the velocities and corresponding accelerations, the 3-dimensional airfoil with endplates is accelerated (and decelerated) with two distinct smooth velocity profiles, shown in Figure 3-43(a). The corresponding acceleration profiles are shown in Figure 3-43(b) with the peak value of acceleration (and deceleration) achieved at $t = 2.5$ s. Based on the velocity profile generated, the chord Reynolds number varies from 4.5×10^5 to 9.9×10^5 for the accelerating airfoil. For the decelerating airfoil, the chord Reynolds number varies from 13×10^5 to 4.5×10^5 . The non-dimensional *Term 3* in the Equation 3-4 attains a peak of $\sim 2.0 \times 10^{-3}$ for the 2g acceleration scenario and $\sim -4.5 \times 10^{-3}$ for the 5g deceleration scenario.

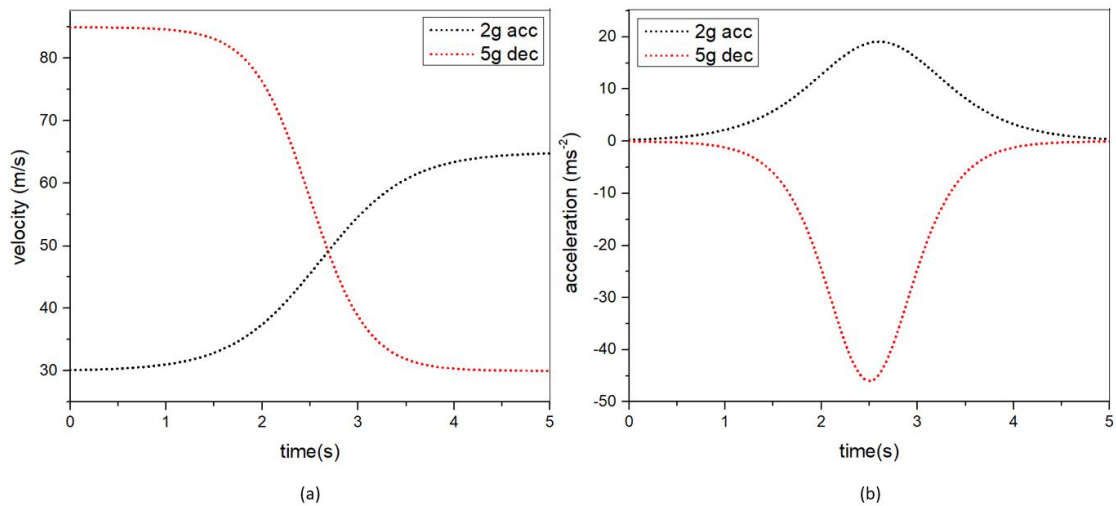


Figure 3-43: (a) Velocity profiles for accelerating and decelerating the 3-dimensional airfoil with endplates, (b) Acceleration profile for accelerating and decelerating 3-dimensional airfoil with endplates

3-4-1-1 Primary & Secondary Vortices for a Steady Flow

In this section, we go over the ability of the CFD model to capture the primary and secondary tip vortex structures, which are discussed in the Section 1-2-6-4. This is performed by comparing the streamwise vorticity component Ω_x , with the results from the experiment at a location $x/c = 1.2$, which is $0.2c$ downstream of the trailing edge of the wing. The chord Reynolds number of the 3D wing in ground effect is 4.5×10^5 . From Figure 3-44, it is evident that the SST $k-\omega$ model captures the main vortical structures that are observed in the experiment reasonably well. However, it must be noted that the peak vorticity of the counter-rotating primary vortex is underpredicted by the SST $k-\omega$ model. Also, since the exact location at which the endplates are attached to the wing-ends in the experiment is not available, some amount of discrepancy is to be expected.

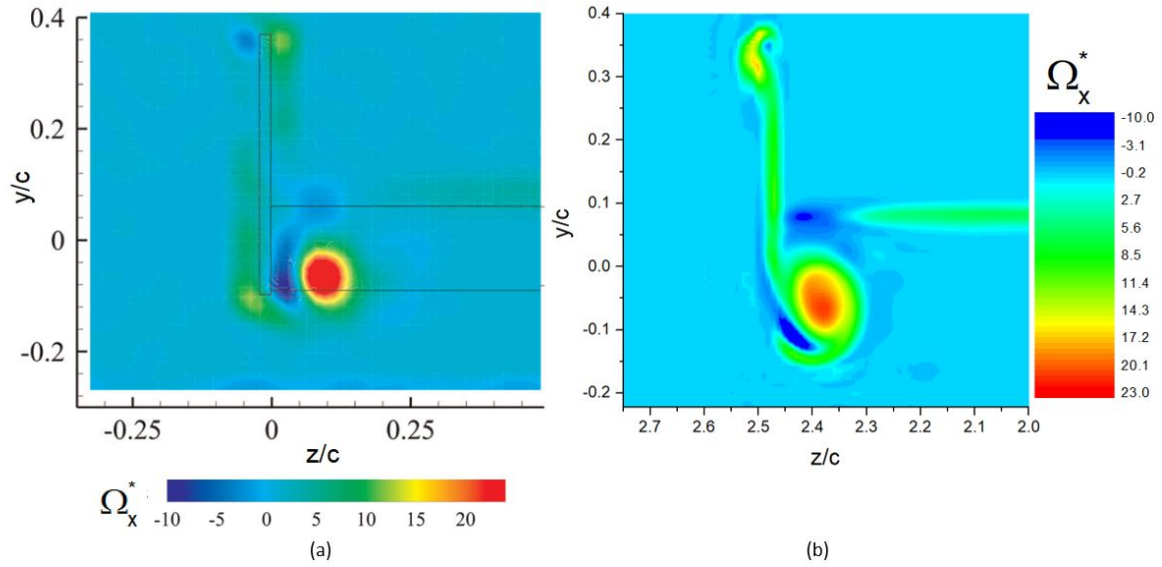


Figure 3-44: Non-dimensional streamwise vorticity, i.e., $(\Omega_x c)/U_\infty$ contours for $h/c = 0.224$ at $x/c = 1.2$ for a streamwise Reynolds number of 4.5×10^6 : (a) Experimental results [6] (b) CFD results for the SST $k-\omega$ model. The SST $k-\omega$ model captures main vortical structures reasonably well, when compared to the vortical contours captured experimentally.

3-4-2 Downforce generated by the airfoil & the drag force on the airfoil

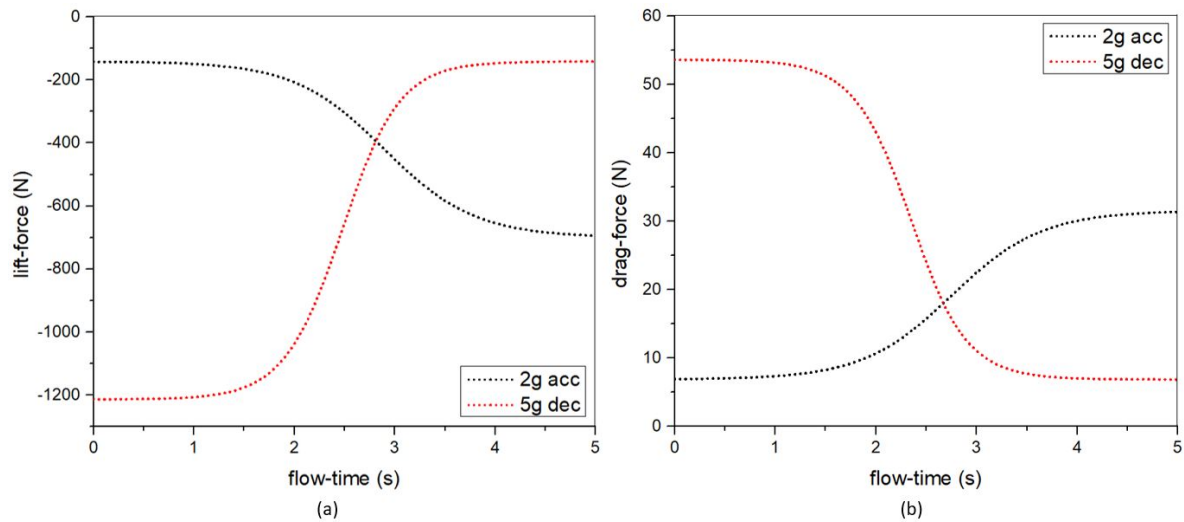


Figure 3-45: (a)Downforce generated by the airfoil accelerated with the non-linear smooth velocity profile, (b)Drag force on the airfoil accelerated with the non-linear smooth velocity profile

The downforce generated by the accelerating (and decelerating) airfoil, and the drag force it experiences, are shown in Figure 3-45. From the figure, it is evident that, on acceleration, the absolute value of the downforce and the drag force. Similarly, on deceleration, the absolute value of the downforce and the drag force decrease. Since the dynamic pressure increases (or decreases) during acceleration (or deceleration), these trends in forces are expected. In order

to determine the influence of translational acceleration on the forces, the forces in the Figure 3-45 are non-dimensionalized with the instantaneous velocity using the Equation 3-10, thus eliminating the trivial effect of the changing dynamic pressure.

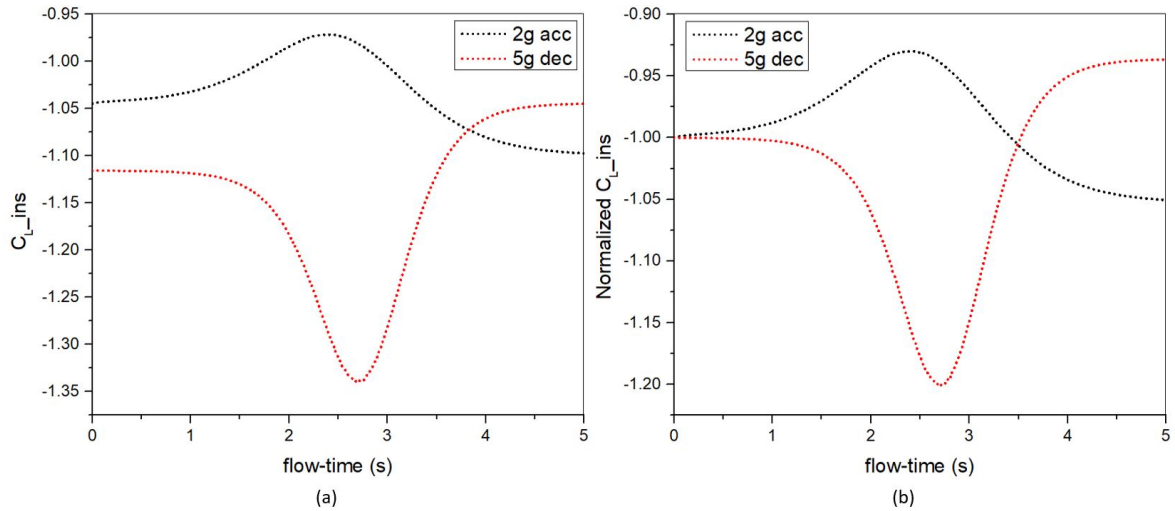


Figure 3-46: (a) Instantaneous downforce coefficient for the 3D airfoil translationally accelerated with the smooth non-linear velocity profile, generated using the Equation 3-10, (b) Same data as (a), but normalized with the instantaneous force coefficient at $t = 0.0s$

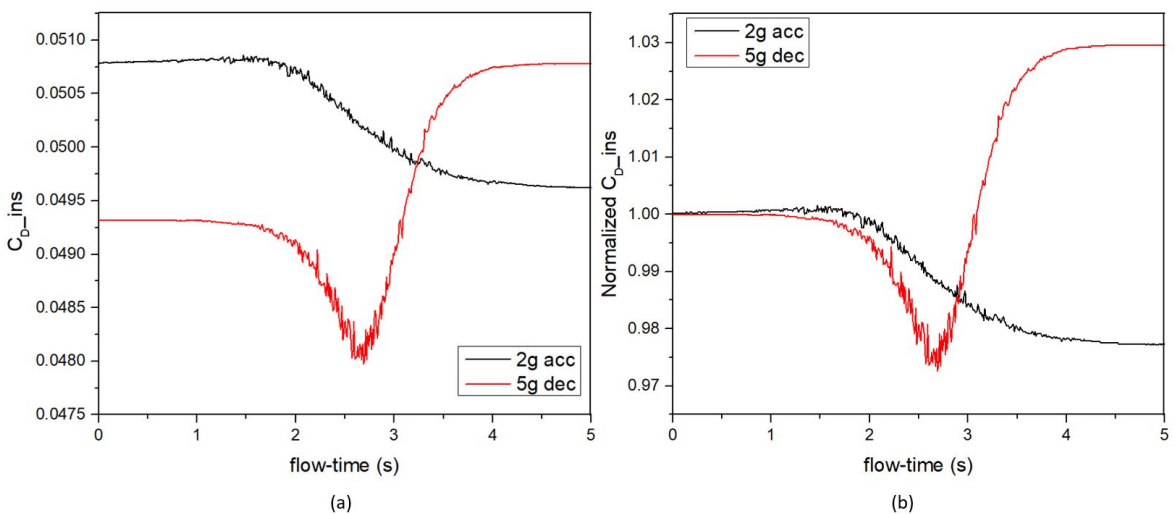


Figure 3-47: (a) Instantaneous drag force coefficient for the 3D airfoil translationally accelerated and decelerated with the smooth non-linear velocity profile, generated using the Equation 3-10, (b) Same data as (a), but normalized with the instantaneous force coefficient at $t = 0.0s$

The Figures 3-46(a) and 3-47(a) show the instantaneous force coefficients for the translationally accelerating and decelerating airfoil, respectively, which are calculated using the Equation 3-10. These instantaneous force coefficients are then normalized with the instantaneous force coefficient at $t = 0.0s$ in Figures 3-46(b) and 3-47(b). From Figure 3-46, it is evident that when the 3D airfoil is subjected to translational acceleration, the downforce coefficient (i.e., $-C_L$) experiences a minimum, with a $\sim 6\%$ loss compared to the value at $t = 0.0s$. Similarly,

when the 3D airfoil is subjected to translational deceleration, the downforce coefficient(i.e., $-C_L$) experiences a maximum, shown by the $\sim 20\%$ gain. The plots in the Figure 3-47 show that, when the 3D airfoil is subjected to translational acceleration, the drag force(i.e., C_D) coefficient encounters a slight maximum, indicated by the $\sim 0.1\%$ gain. Likewise, when the 3D airfoil is subjected to translational deceleration, the drag force coefficient(i.e., C_D) experiences a minimum, shown by the $\sim 2.5\%$ loss.

Further investigation on the influence of translational acceleration and deceleration of the 3D airfoil is performed by comparing the instantaneous force coefficients with the force coefficients at the same steady state velocities, as shown in the Figures 3-48 and 3-49.

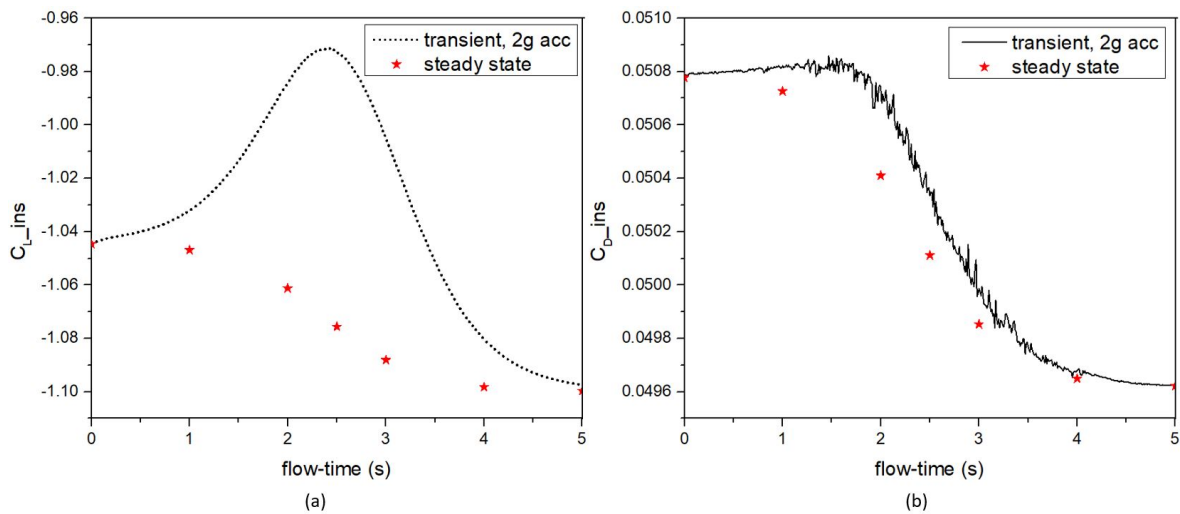


Figure 3-48: (a) Instantaneous downforce coefficient and (b) Instantaneous drag force coefficient for the translationally accelerated 3D airfoil compared with the downforce coefficients at the same steady state velocities. The translationally accelerating airfoil generates less downforce than when compared to that generated at the same steady state velocities. The drag force experienced by the translationally accelerated airfoil is higher than that experienced at the same steady state velocities

From the Figure 3-48(a), it is evident that when the 3D airfoil is subjected to translational acceleration, the downforce generated by the airfoil is lower than the downforce generated at the same steady state velocities and this difference is maximum ($\sim 9\%$) when the peak value of translational acceleration is achieved at $t = 2.5$ s. The Figure 3-48(b) reveals that translationally accelerating airfoil experiences higher drag force when compared to that experienced at the same steady state velocities. Similarly, from the Figure 3-49(a), it can be seen that the 3D airfoil decelerated translationally generates more downforce than that generated by the airfoil at the same steady state velocities and this difference is maximum at the peak value of translational deceleration. Likewise, the Figure 3-49(b) shows that, the translationally decelerating airfoil encounters lower drag force than that encountered by the airfoil at the same steady state velocities.

The loss(or gain) of downforce for the translationally accelerating(or decelerating) airfoil when compared to the steady state downforce generated by the airfoil can be attributed to the pressure difference on the suction side of the airfoil, as indicated in the Figure 3-50. For the translationally accelerating airfoil, the pressure distribution on the suction side

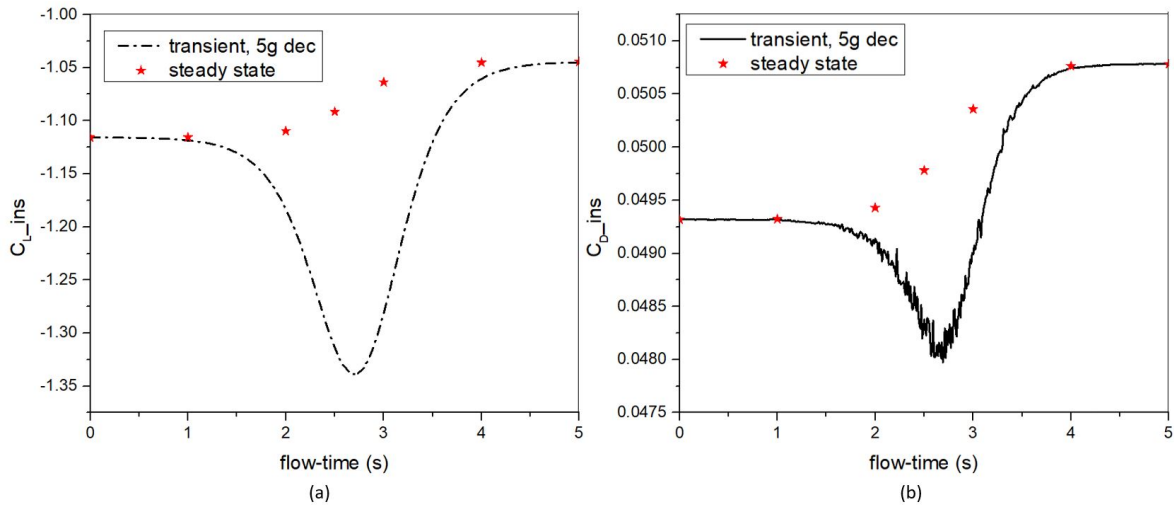


Figure 3-49: (a)Instantaneous downforce coefficient and (b)Instantaneous drag force coefficient for the translationally decelerated 3D airfoil compared with the downforce coefficients at the same steady state velocities. The translationally decelerating airfoil generates more downforce than when compared to that generated at the same steady state velocities. The drag force experienced by the translationally accelerated airfoil is lower than that experienced at the same steady state velocities.

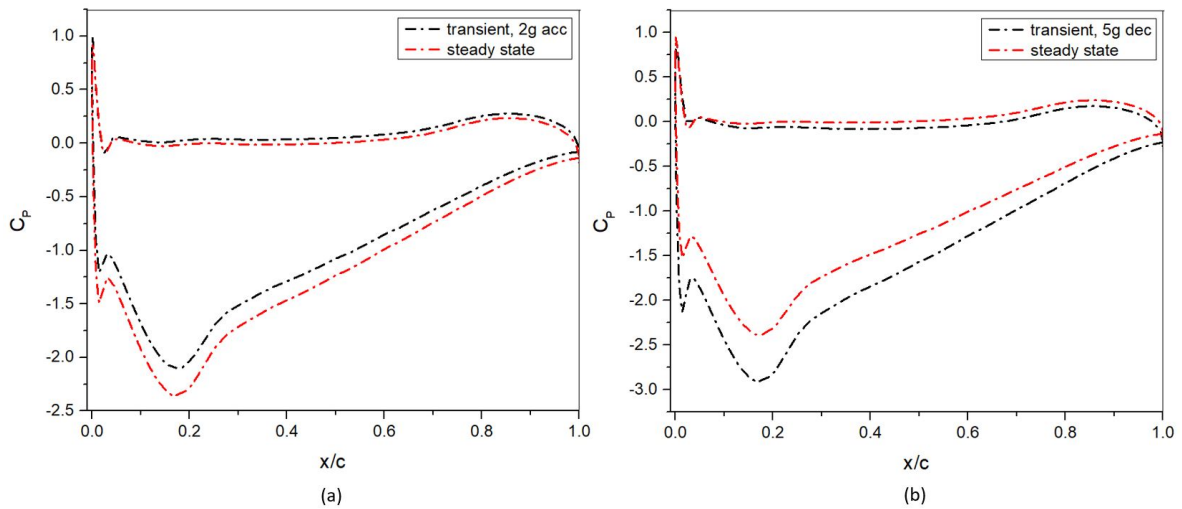


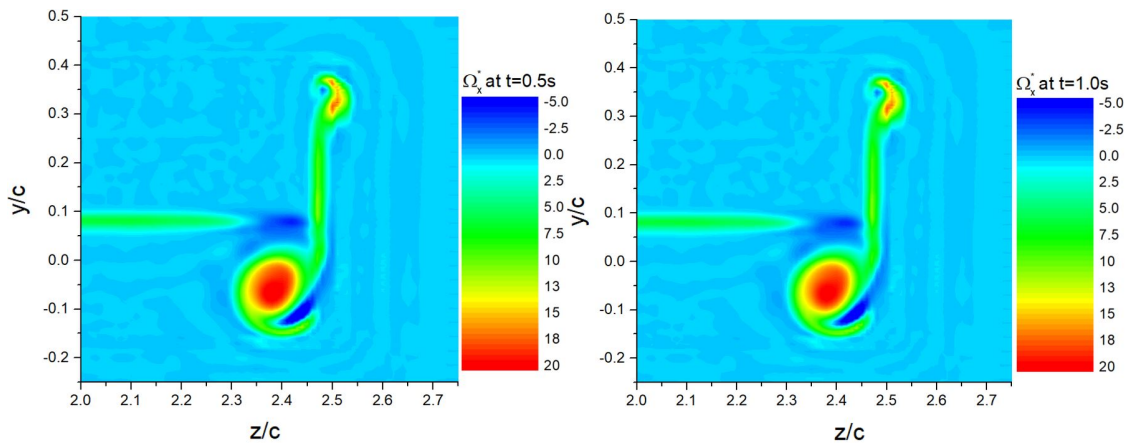
Figure 3-50: Pressure distribution on the airfoil in the mid-plane (i.e., $z=0$) at $t = 2.5s$ normalized with instantaneous dynamic pressure $\frac{1}{2}\rho U_\infty^2$ for the translationally accelerating airfoil. The pressure distribution on the suction side is not as low as the pressure distribution at the same velocity under steady state conditions, resulting in a loss of the downforce. (b)Pressure distribution on the airfoil in the mid-plane (i.e., $z=0$) at $t = 2.5s$ normalized with instantaneous dynamic pressure $\frac{1}{2}\rho U_\infty^2$ for the translationally decelerating airfoil. The pressure distribution on the suction side is not as high as the pressure distribution at the same velocity under steady state conditions, resulting in a gain in the downforce.

of the airfoil at any given velocity is not as low as the pressure distribution at the same velocity under the steady-state conditions. Similarly, the pressure distribution on the suction

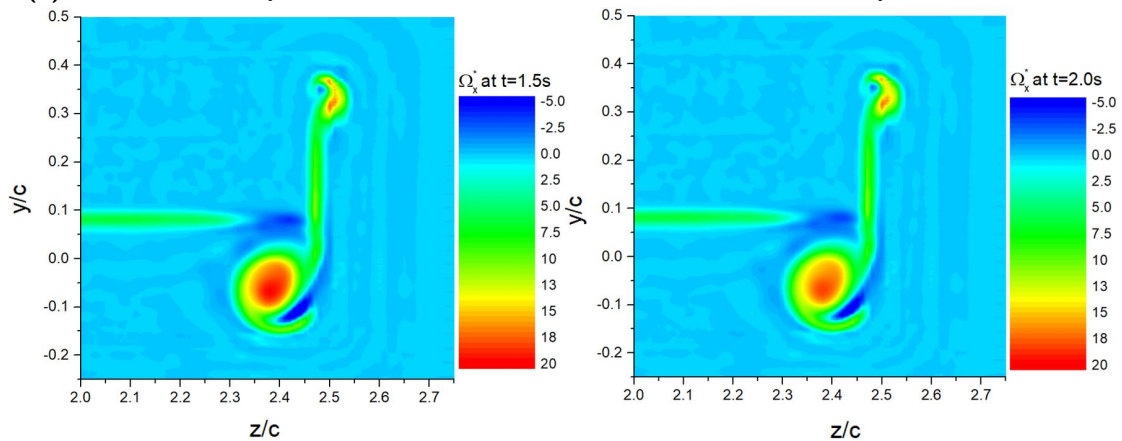
side of the translationally decelerating airfoil at any given velocity is lower than the pressure distribution at the same velocity under steady-state conditions. A more detailed discussion on the mechanism that contributes to the variation in downforce when the wing is accelerated(or decelerated) translationally is performed in the Section 3-5-2.

The higher(or lower) drag force experienced by the translationally accelerating(or decelerating) airfoil when compared to the drag force experienced at the same steady state velocities, as shown in the Figures 3-48(b) and 3-49(b), can be attributed to added mass effects. Furthermore, in this instance, it can be seen from the Figure 3-46 and 3-47 that, the influence of translational acceleration on the forces is lower than that observed for the translational deceleration. This can be attributed to the higher magnitude of non-dimensional *Term 3*, i.e., $\frac{AC}{U^2}$ from Equation 3-4 for the translationally decelerating airfoil(4.5×10^{-3}) when compared to that of the translationally accelerating airfoil(2.0×10^{-3}).

3-4-2-1 Streamwise Vorticity: Translationally Accelerating and Decelerating Airfoil



(a) Streamwise vorticity non-dimensionalized with instantaneous free stream velocity at $t = 0.5s$ and $1.0s$



(b) Streamwise vorticity non-dimensionalized with instantaneous free stream velocity at $t = 1.5s$ and $2.0s$

Figure 3-51: The trends in contours of streamwise vorticity non-dimensionalized with instantaneous free stream velocity from $t = 0.0 s$ to $2.0 s$ at $x/c = 1.2$, when airfoil is accelerated translationally

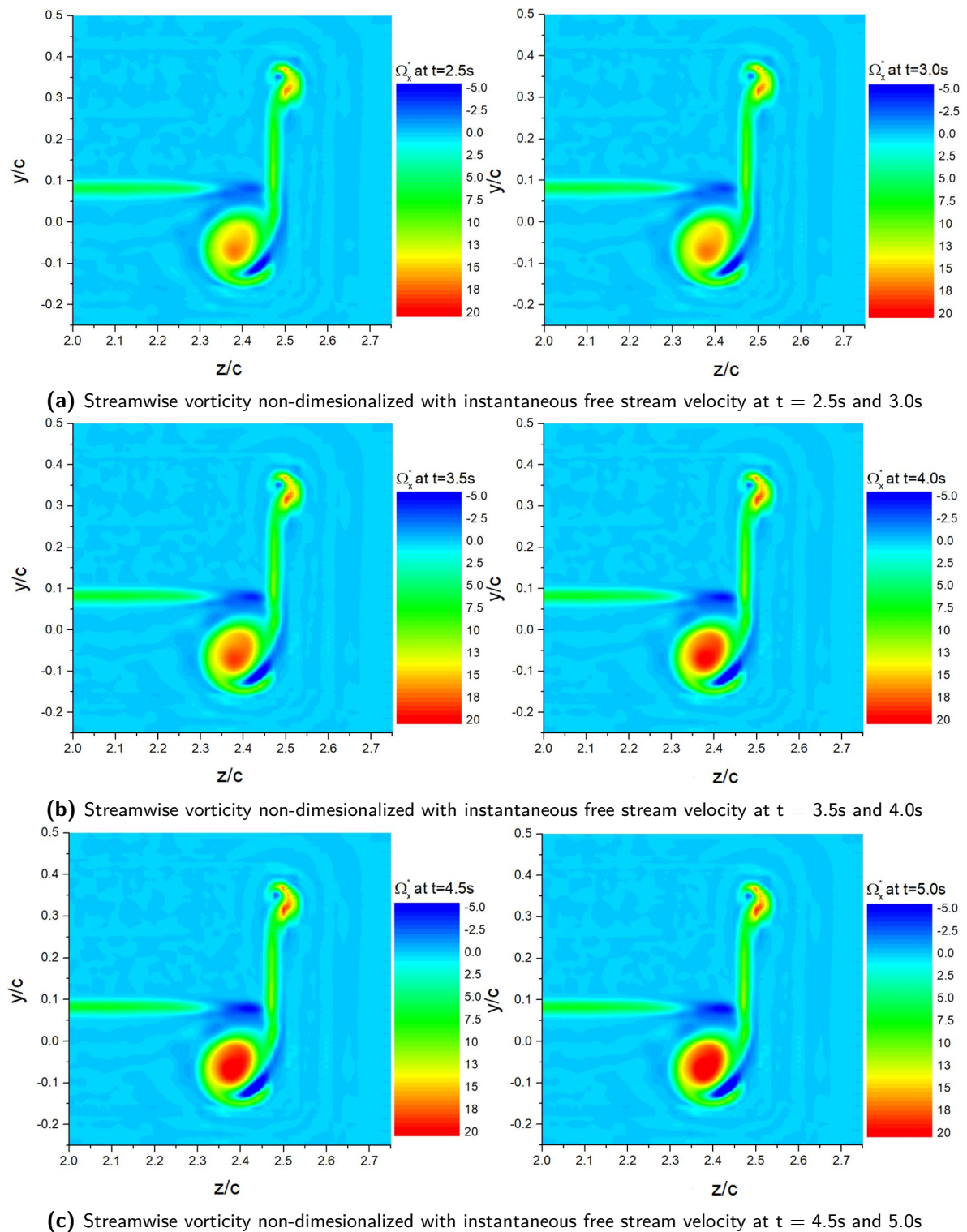


Figure 3-52: The trends in contours of streamwise vorticity non-dimensionalized with instantaneous free stream velocity from $t = 2.5\text{ s}$ to 5.0 s at $x/c = 1.2$, when the airfoil is accelerated translationally

From the section above, it is evident that the translationally accelerated(or decelerated) airfoil experiences a temporary loss(or gain) in the downforce coefficient. Below, we investigate the flow phenomenon that may be vital for this change in downforce coefficient. The Figures 3-51 and 3-52 illustrate the contours of the streamwise vorticity downstream of the wing at $x/c = 1.2$ when the airfoil is subjected to translational acceleration. As discussed in the Section 1-2-6-4, the primary vortex is formed due to the pressure difference between the two sides of the endplate on the suction side of the airfoil. Since the vortex core is a region where the pressure has a local minimum, this vortex contributes to the downforce of the wing. From the Figures 3-51 and 3-52, it is evident that there is a loss in the strength of the primary vortices as the airfoil is subjected to translational acceleration which contributes to a reduced instantaneous downforce coefficient, as shown in the Figure 3-46.

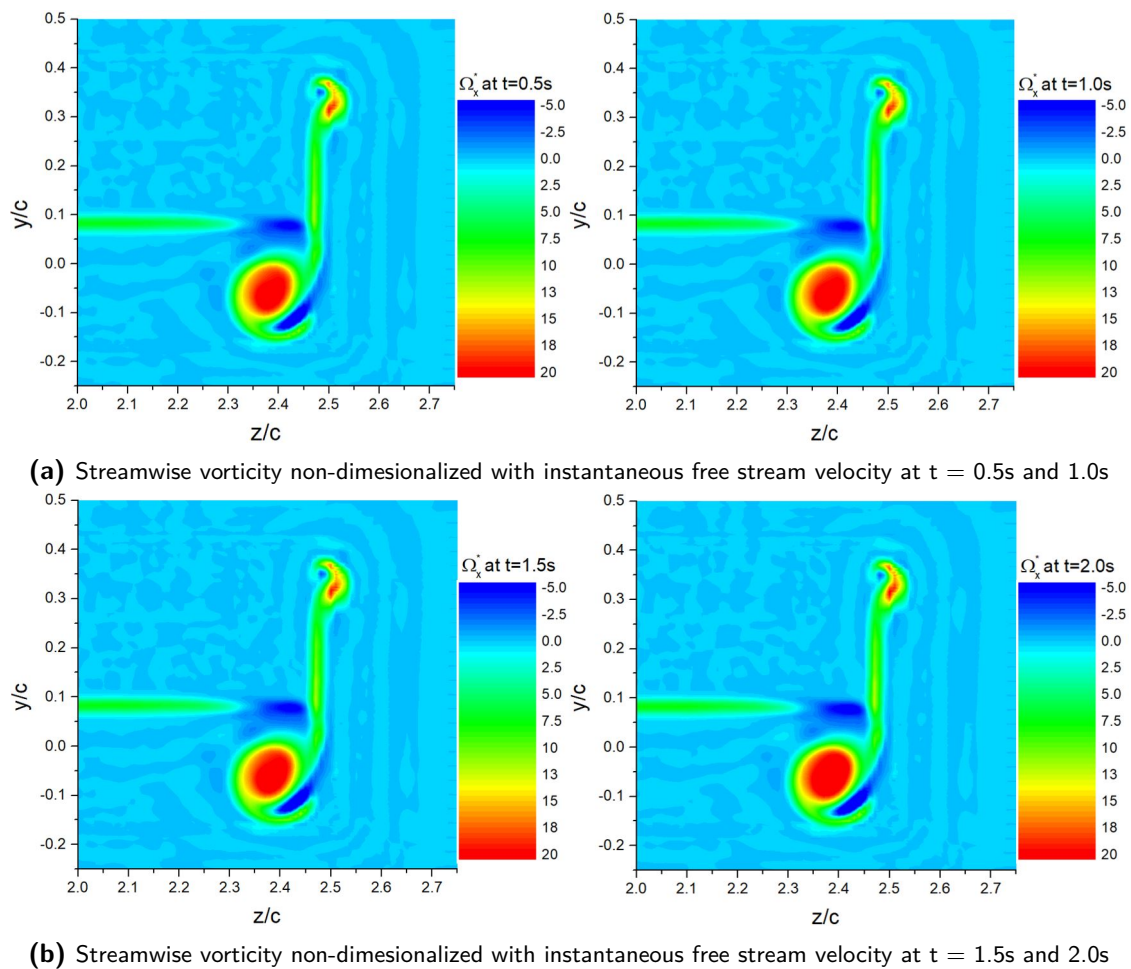
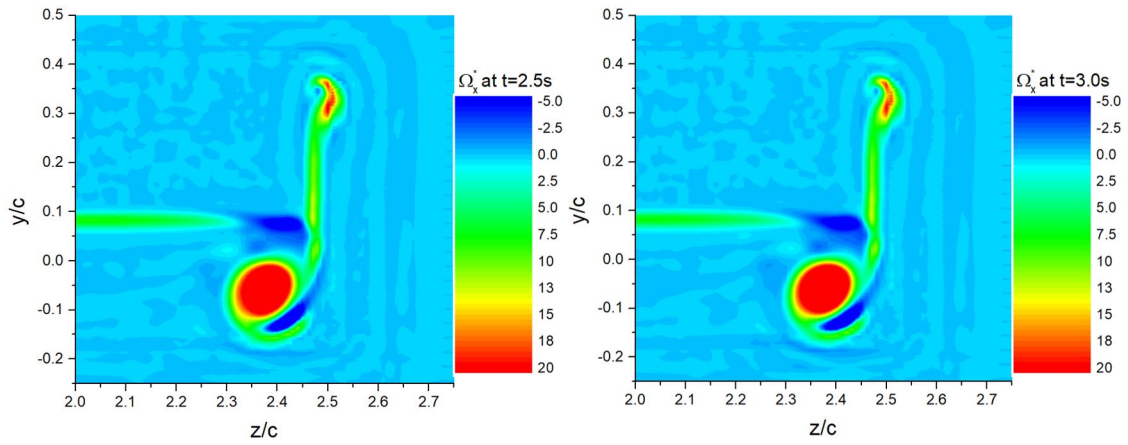


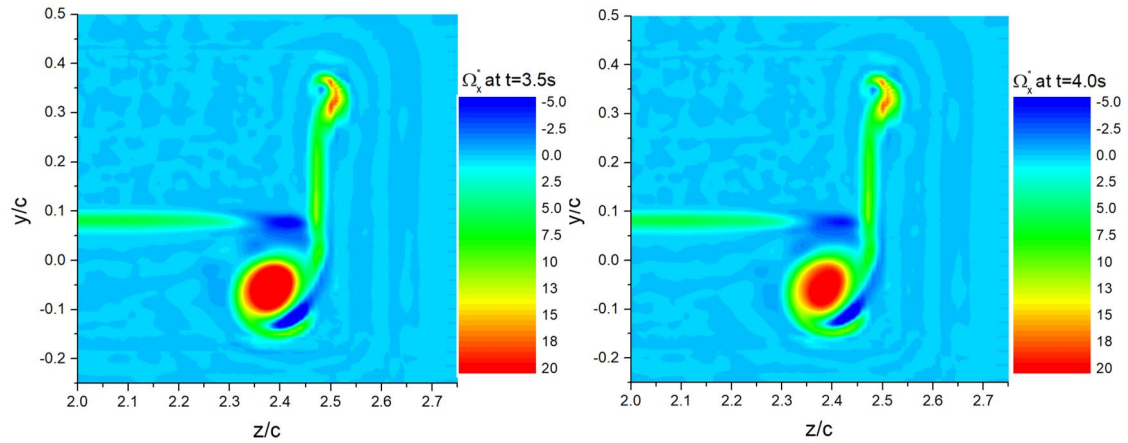
Figure 3-53: The trends in contours of streamwise vorticity non-dimensionalized with instantaneous free stream velocity from $t = 0.0$ s to $2.0s$ at $x/c = 1.2$, when airfoil is decelerated translationally

The Figures 3-53 and 3-54 illustrate the contours of the streamwise vorticity downstream of the wing at $x/c = 1.2$ when the airfoil is subjected to translational deceleration. From the Figures 3-51 and 3-52, it is evident that there is an increase in the strength of the primary vortices as the airfoil is subjected to translational acceleration which contributes to

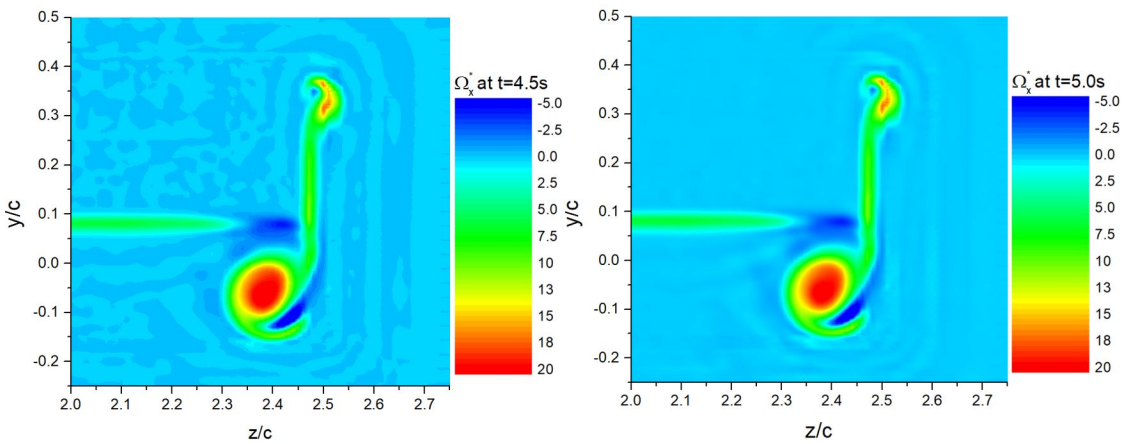
an increased instantaneous downforce coefficient, as shown in the Figure 3-46.



(a) Streamwise vorticity non-dimesionalized with instantaneous free stream velocity at $t = 2.5s$ and $3.0s$



(b) Streamwise vorticity non-dimesionalized with instantaneous free stream velocity at $t = 3.5s$ and $4.0s$



(c) Streamwise vorticity non-dimesionalized with instantaneous free stream velocity at $t = 4.5s$ and $5.0s$

Figure 3-54: The trends in contours of streamwise vorticity non-dimesionalized with instantaneous free stream velocity from $t = 2.5 s$ to $5.0 s$ at $x/c = 1.2$, when the airfoil is accelerated translationally

3-4-2-2 Behavior of the Flow Separation Point

The response of the location of the separation point to the translational acceleration is investigated by studying the instantaneous x-wall shear stress at different times. Figure 3-55 reveals the instantaneous x-wall shear stress at the mid-plane (i.e., $z = 0$) of the translationally accelerating airfoil. At $t = 0.0s$, the figure reveals flow separation at the trailing edge of the airfoil on the suction side owing to the streamwise adverse pressure gradient encountered. From the figure, it is evident that when the airfoil is subjected to translational acceleration, the location of the separation point shifts downstream with time, until there is no flow separation. The Figure 3-56 reveals the instantaneous x-wall shear stress at the mid-plane (i.e., $z = 0$) of the translationally decelerating airfoil. At $t = 0.0s$, the figure reveals no flow separation at the trailing edge of the airfoil on the suction side. From the figure, it is evident that when the airfoil is subjected to translational deceleration, the location of the separation point shifts upstream with time.

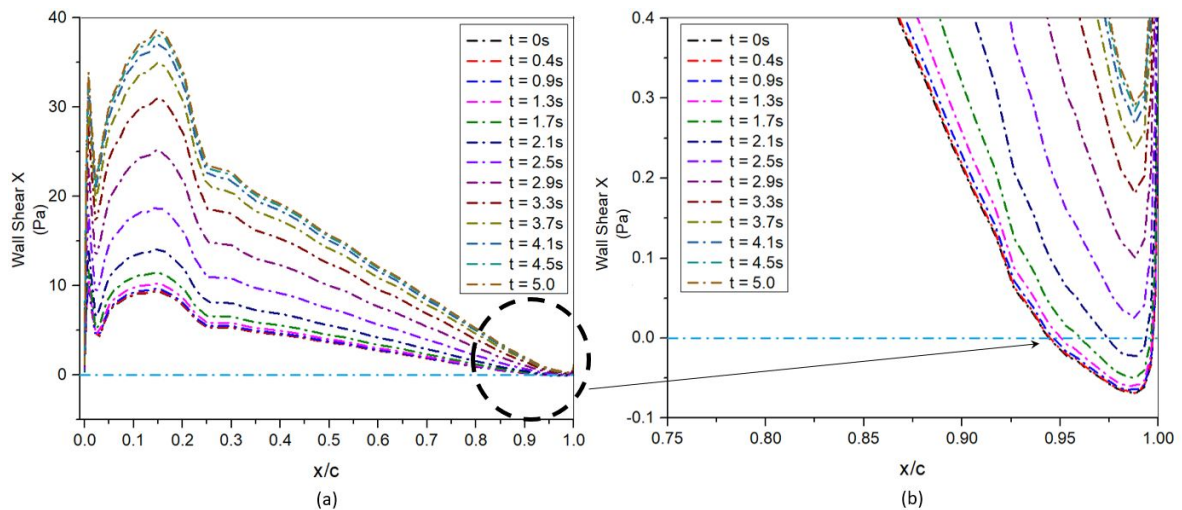


Figure 3-55: Response of the location of separation point to translational acceleration. The location of the separation point is indicated by the change in sign of the x-wall shear stress. (a) Instantaneous x-wall shear stress on the airfoil suction side at the mid-plane (i.e., $z = 0$), (b) Enhanced image of the encircled region. The enhanced image of the x-wall shear stress reveals that, the location of the separation point moves downstream with time when the airfoil is accelerated translationally, until there is no flow separation.

From the Figures 3-55 and 3-56, it is evident that, the location of separation point moves downstream with increasing chord Reynolds number, and the location of separation point moves upstream with decreasing chord Reynolds number.

Furthermore, the location of the separation point of the translationally accelerated and decelerated airfoil compared to that at same steady state velocities is shown in the Figure 3-57. Figure 3-57(a) shows the instantaneous x-wall shear stress for the translationally accelerating airfoil in the mid-plane ($z = 0$) at $t = 2.1s$ compared with the x-wall shear stress at the same steady state velocity. From the figure, it is evident that the translational acceleration has no significant on the location of the separation point. Similarly, the Figure 3-57(b) reveals the instantaneous x-wall shear stress for the translationally decelerating airfoil in the mid-plane ($z = 0$) at $t = 4.0s$ compared with the x-wall shear stress at the same steady state velocity, and

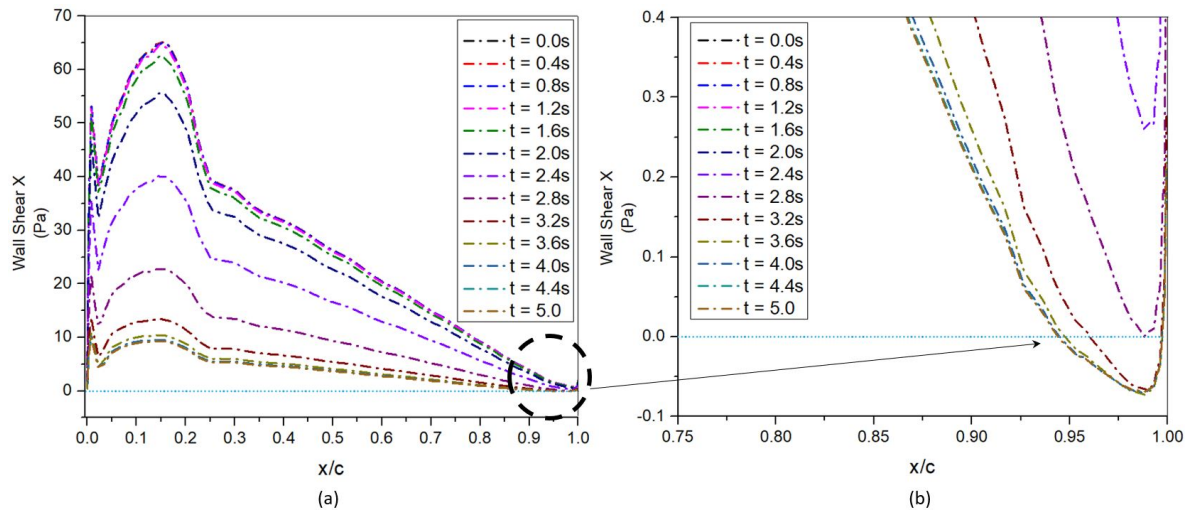


Figure 3-56: Response of the location of separation point to translational deceleration. The location of the separation point is indicated by the change in sign of the x-wall shear stress.(a) Instantaneous x-wall shear stress on the airfoil suction side at the mid-plane(i.e., $z = 0$), (b) Enhanced image of the encircled region. The enhanced image of the x-wall shear stress reveals that, the location of the separation point moves upstream with time when the airfoil is decelerated translationally from the onset of separation.

again the location of separation point is not influenced by the translational deceleration.

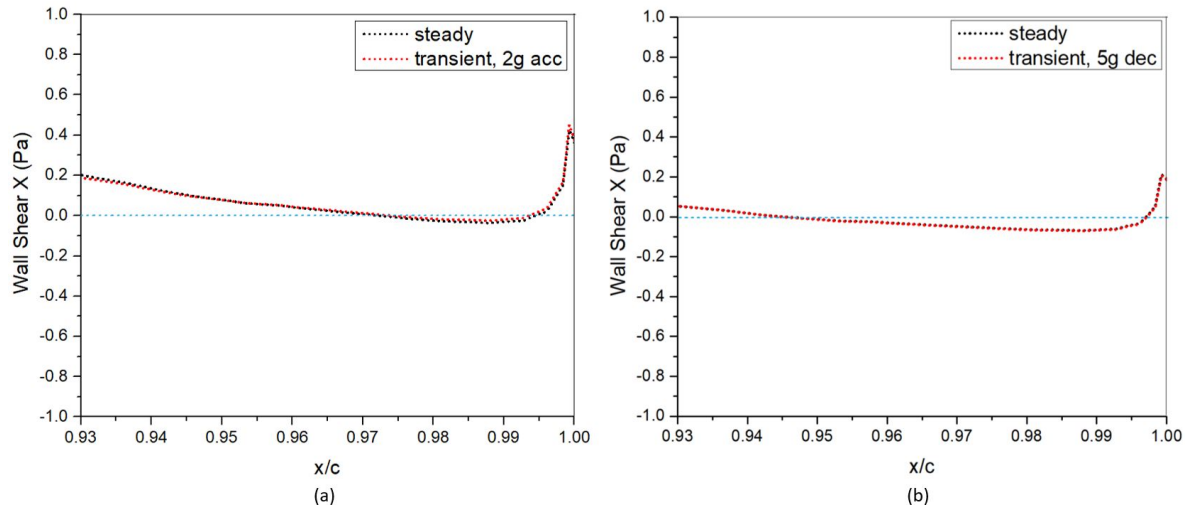


Figure 3-57: Instantaneous x-wall shear stress in the mid-plane for (a) Translationally accelerating airfoil at $t = 2.1s$ compared with the x-wall shear stress at the same steady state velocity, (b) Translationally decelerating airfoil at $t = 4.0s$ compared with the x-wall shear stress at the same steady state velocity. The location of the separation point for the translationally accelerating(or decelerating) airfoil, at any time t , is identical to that of the airfoil at the same steady state velocity.

3-4-3 Influence of the magnitude of acceleration on the downforce and drag force of the translationally accelerating & decelerating airfoil

In this section, the influence of the magnitude of the acceleration on the downforce and drag force of the 3D airfoil is investigated. The 3D airfoil is translationally accelerated and decelerated with two distinct velocity profiles, i.e., “8g acc” and “8g dec” shown in the Figure 3-58, where the peak value of translational acceleration (and deceleration) is achieved at $t = 2.5$ s. For the 3D airfoil accelerated translationally with the “8g acc” velocity profile, the chord Reynolds number varies from 0.4×10^5 to 1.2×10^6 . For the 3D airfoil accelerated translationally with the “8g dec” velocity profile, the chord Reynolds number varies from 1.2×10^6 to 0.4×10^5 . The downforce and the drag force of the 3D airfoil for these cases of translational acceleration and deceleration is then compared with the “2g acc” and “5g dec” results in the Section 3-4-2. The initial and final velocities are chosen such that they lie in the operating range of racecar speeds. The time for which the airfoil is accelerated (and decelerated) translationally is kept the same at $t = 5.0$ s. Furthermore, it must be noted that this magnitude of translational acceleration (or deceleration) lies outside the range of magnitude of acceleration (or deceleration), i.e., $\sim 2g$ to $-5g$, that a racecar undergoes on the racetrack.

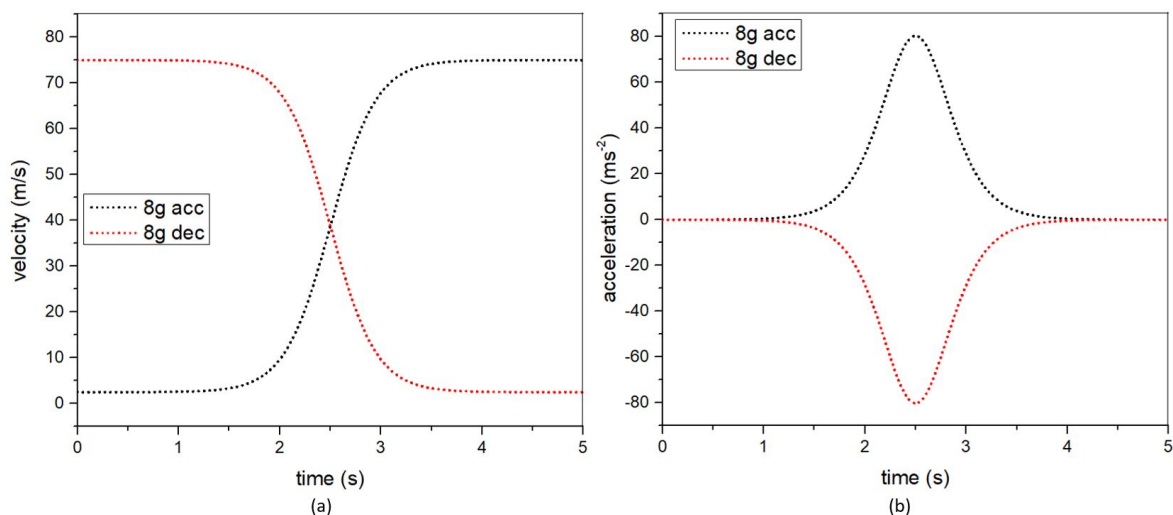


Figure 3-58: (a) Velocity profiles for accelerating and decelerating the 3-dimensional airfoil with endplates, (b) Acceleration profile for accelerating and decelerating 3-dimensional airfoil with endplates

The downforce generated by the translationally accelerated and decelerated airfoil is shown in the Figure 3-59(a). Figure 3-59(b) shows the drag force on the translationally accelerating and decelerating airfoil.

The forces in the figure above are then non-dimensionalized with the instantaneous free stream velocity to determine the influence of translational acceleration (and deceleration) on the forces using the Equation 3-10, as shown in the Figures 3-60 and 3-61.

Figures 3-60 and 3-61 reveal that, the translationally accelerating 3D airfoil experiences a minimum, indicated by $\sim 20\%$ loss in the downforce coefficient and a maximum, shown by the 20% increase in the drag force coefficient. Similarly, the translationally decelerating 3D

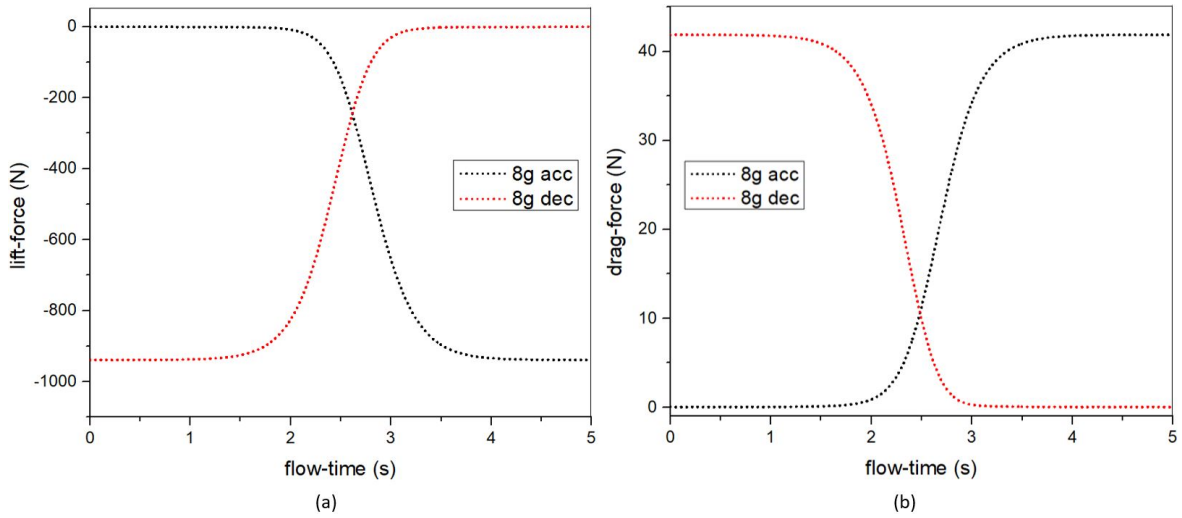


Figure 3-59: (a)Downforce generated by the translationally accelerating and decelerating 3D airfoil, (b)Drag force on the translationally accelerating and decelerating 3D airfoil

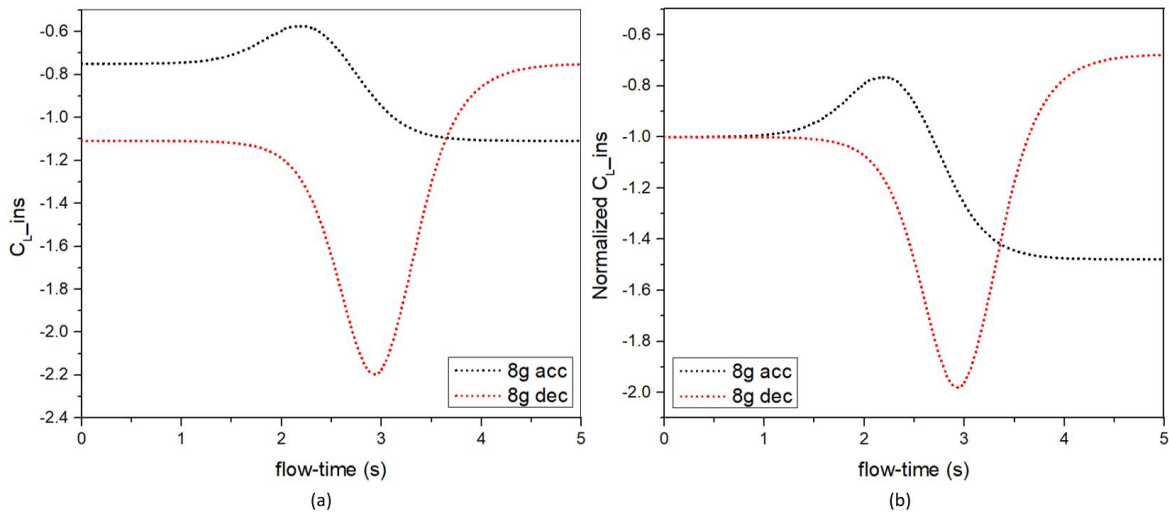


Figure 3-60: (a)Instantaneous downforce coefficient for the 3D airfoil translationally accelerated with the smooth non-linear velocity profile, generated using the Equation 3-10, (b)Normalized instantaneous downforce coefficient for the 3D airfoil translationally accelerated with the smooth non-linear velocity profile, generated using the Equation 3-10.

airfoil undergoes a maximum, given by the $\sim 100\%$ gain in the downforce coefficient and a minimum, shown by the $\sim 60\%$ drop in drag force coefficient. Furthermore, these plots reveal that the influence of the 8g magnitude translational acceleration (and deceleration) is higher than in the Figures 3-46 and 3-47.

In order to investigate these differences in the influence of translational acceleration (and deceleration) on the forces, we compare the magnitudes of the non-dimensional *Term 3* from the Equation 3-4, i.e., AC/U^2 for the different scenarios of acceleration and deceleration discussed above. The plots in Figure 3-62 show the variation of the term AC/U^2 during the course of translational acceleration and deceleration of the 3D airfoil. The plots reveal that

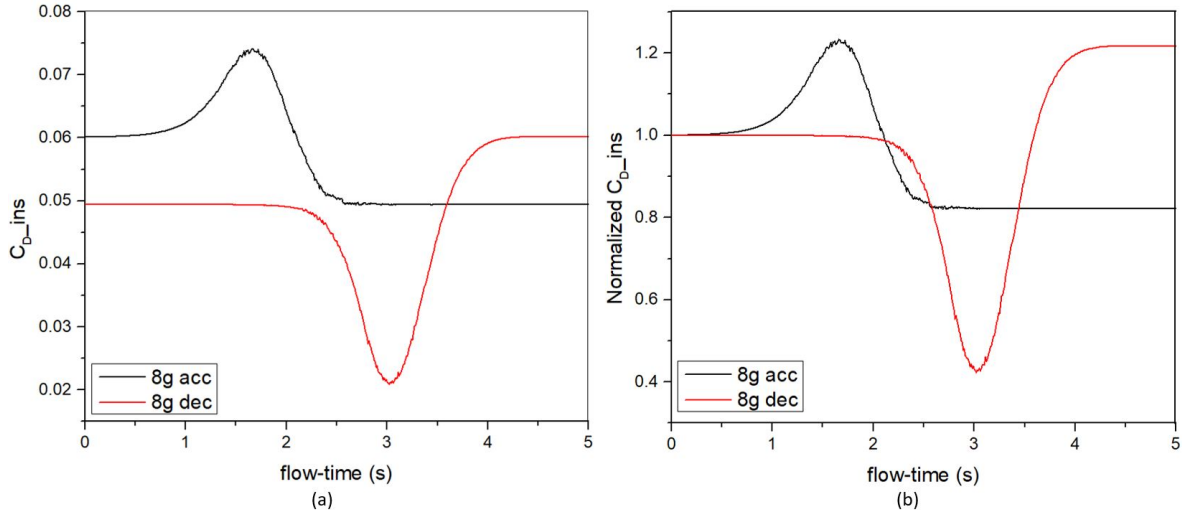
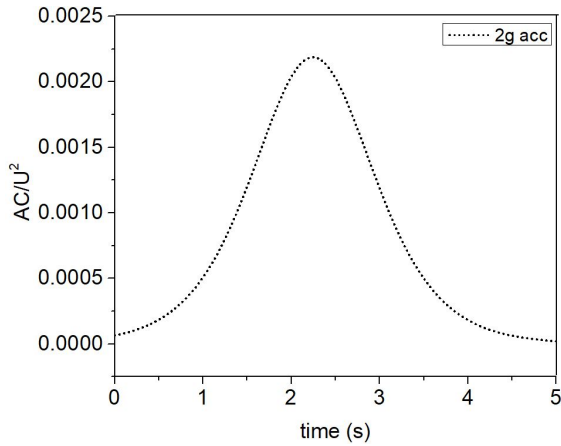


Figure 3-61: (a) Instantaneous drag force coefficient for the 3D airfoil translationally accelerated and decelerated with the smooth non-linear velocity profile, generated using the Equation 3-10, (b) Normalized instantaneous drag force coefficient for the 3D airfoil translationally accelerated and decelerated with the smooth non-linear velocity profile, generated using the Equation 3-10.

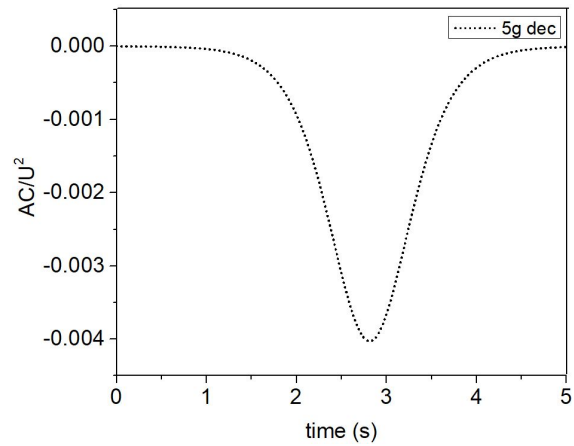
the impact of the translational acceleration (and deceleration) on the forces is highest for the “8g acc” and “8g dec” scenarios, and this is reflected in the normalized force coefficient plots in Figures 3-46, 3-47, 3-60 and 3-61, where the “8g acc” has a higher influence on the forces than the “2g acc” translational acceleration scenario and the “8g dec” has a higher influence on the forces than the “5g dec” translational deceleration scenario. Furthermore, the time at which the peak value of the non-dimensional term AC/U^2 is attained in Figure 3-62 is consistent with the time at which the peak values of the instantaneous force coefficient was attained in Figures 3-47 and 3-61.

Further investigations on the magnitude of the convective acceleration of flow experienced by the 3D airfoil is carried out by measuring the streamwise component of the convective acceleration at $x/c = 0.2$ in the mid-plane ($z = 0$) for the different translational acceleration and deceleration scenarios discussed above. An illustration of the streamwise convective acceleration of the flow encountered by the translationally accelerating 3D airfoil in the mid-plane ($z = 0$) can be seen in the Figure 3-63, which shows the instantaneous streamwise acceleration for the 3D airfoil accelerated with the “8g acc” velocity profile at $t = 1.6s$. From Figure 3-63, it is evident that the magnitude of streamwise convective acceleration, i.e., $\frac{\partial u}{\partial x}$ of the fluid is $O(10)$.

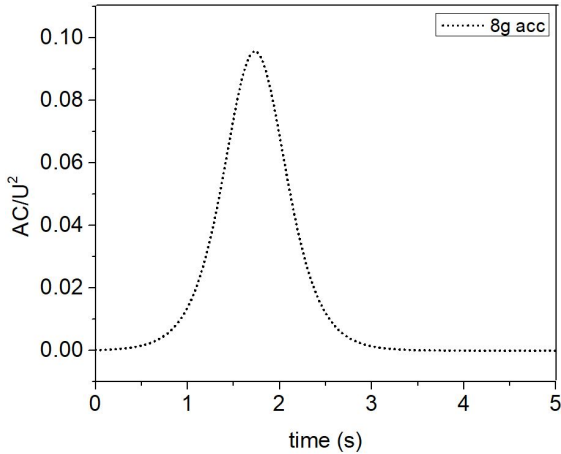
The plots in the Figure 3-64 and 3-65 capture the magnitude of the instantaneous streamwise acceleration encountered by the translationally accelerating and decelerating 3D airfoil in the mid-plane ($z = 0$) at a time t when the term AC/U^2 is at its peak, measured at $x/c = 0.2$ for the different scenarios of acceleration and deceleration. The plot in Figure 3-64a indicates that the magnitude of the streamwise acceleration of the flow encountered by the airfoil is $O(10^4)$, which is $O(10^3)$ greater than the magnitude of its translation acceleration, which is $O(10)$ at $t \sim 2.5s$. This is consistent with the plot 3-62a, where the scaling analysis reveals that the magnitude of the non-dimensional translational acceleration term, i.e., AC/U^2 is $O(10^3)$ lower than that of the convective acceleration term. The plot in Figure 3-64b shows



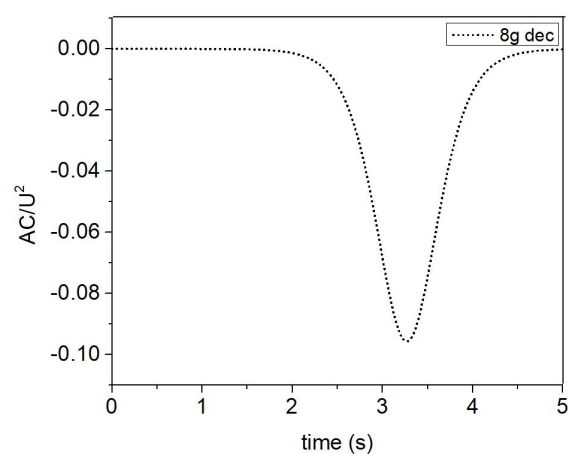
(a) Variation of the non-dimensional *Term 3* in the Equation 3-4 when the 3D airfoil is subjected to a peak translational acceleration 2g



(b) Variation of the non-dimensional *Term 3* in the Equation 3-4 when the 3D airfoil is subjected to a peak translational deceleration 5g



(c) Variation of the non-dimensional *Term 3* in the Equation 3-4 when the 3D airfoil is subjected to a peak translational acceleration 8g



(d) Variation of the non-dimensional *Term 3* in the Equation 3-4 when the 3D airfoil is subjected to a peak translational deceleration 8g

Figure 3-62: Variation of the non-dimensional *Term 3* in the Equation 3-4 when the 3D airfoil is subjected to different values of peak translational acceleration and deceleration. These plots reveal the magnitude of the *Term 3* when compared to the non-linear term corresponding to the convective acceleration encountered by the translationally accelerating airfoil, which is of order 1, from the Equation 3-4.

that, the magnitude of the streamwise acceleration of the flow encountered by the airfoil is $O(10^4)$, which is $O(10^3)$ greater than the magnitude of its translation deceleration, which is $O(10)$ at $t \sim 2.8$ s. This is consistent with the plot 3-62b, where the scaling analysis reveals that the magnitude of the non-dimensional translational deceleration term, i.e., AC/U^2 is $O(10^3)$ lower than that of the convective acceleration term.

Similarly, the plot in Figure 3-65a indicates that the magnitude of the streamwise acceleration of the flow encountered by the airfoil is $O(10)$, which is $O(10)$ greater than the magnitude of its translation acceleration, which is $O(1)$ at $t \sim 1.6$ s. This is reflected in the plot 3-62c, where the scaling analysis reveals that the magnitude of the translational acceleration term, i.e., AC/U^2

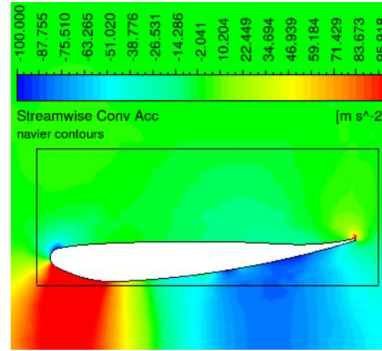
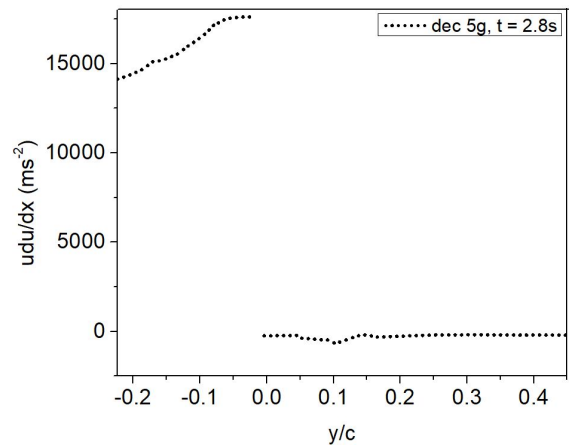
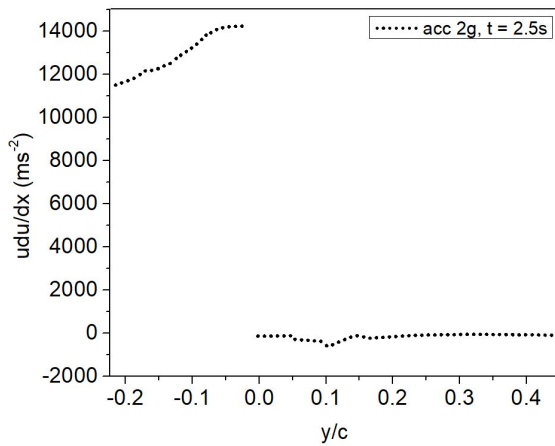


Figure 3-63: Instantaneous streamwise convective acceleration, i.e., $u \frac{\partial u}{\partial x}$ contour in the mid-plane ($z = 0$) for the 3D airfoil accelerated translationally with the “8g acc” velocity profile at $t = 1.6s$.



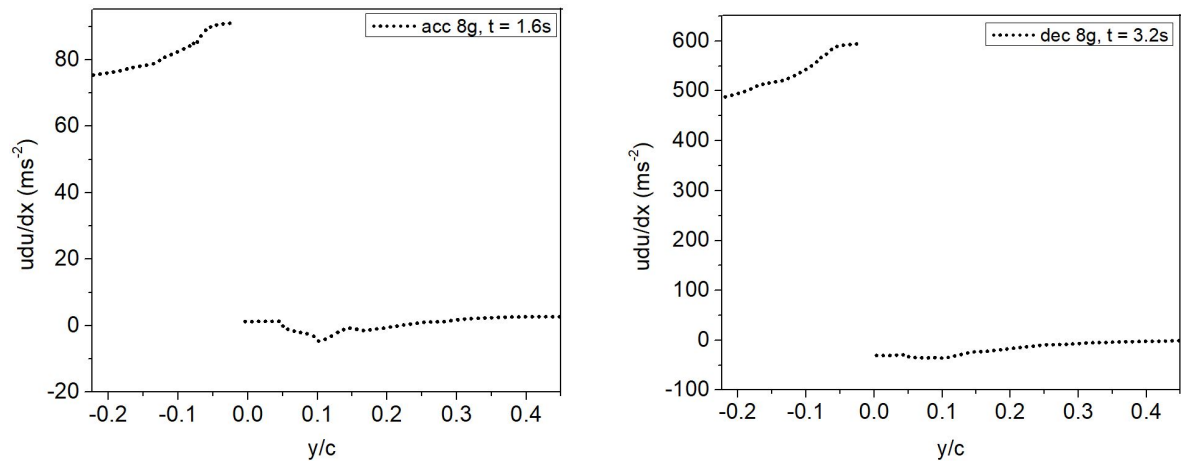
(a) Magnitude of instantaneous streamwise convective acceleration of the flow encountered by the 3D airfoil accelerated translationally with the “2g acc” velocity profile measured in the mid-plane ($z = 0$) and $x/c = 0.2$ at $t \sim 2.5s$

(b) Magnitude of instantaneous streamwise convective acceleration of the flow encountered by the 3D airfoil decelerated translationally with the “5g dec” velocity profile measured in the mid-plane ($z = 0$) and $x/c = 0.2$ at $t \sim 2.8s$

Figure 3-64: Magnitude of instantaneous streamwise convective acceleration of the flow encountered by the translationally accelerating and decelerating 3D airfoil in the mid-plane ($z = 0$), $x/c = 1.2$ at a time t when the term AC/U^2 at its peak.

is $O(10)$ lower than that of the convective acceleration term. The plot in Figure 3-65b shows that, the magnitude of the streamwise acceleration of the flow encountered by the airfoil is $O(10^2)$, which is $O(10)$ greater than the magnitude of its translation deceleration, which is $O(10)$ at $t \sim 3.2s$. This is reflected in the plot 3-62d, where the scaling analysis reveals that the magnitude of the non-dimensional translational deceleration term, i.e., AC/U^2 is $O(10^{-1})$.

These investigations have revealed that the magnitude of the translational acceleration (and deceleration) compared to the convective acceleration of the flow encountered by the 3D airfoil is higher for the “8g acc” and “8g dec” scenarios than for the “2g acc” and “5g dec”, which is why the influence of the former acceleration (and deceleration) is higher on the forces than the latter. Also, the magnitudes of velocities in the “8g acc” and “8g dec” scenarios are lower



(a) Magnitude of instantaneous streamwise convective acceleration of the flow encountered by the 3D airfoil accelerated translationally with the “8g acc” velocity profile measured in the mid-plane($z = 0$) and $x/c = 0.2$ at $t \sim 1.6$ s

(b) Magnitude of instantaneous streamwise convective acceleration of the flow encountered by the 3D airfoil decelerated translationally with the “8g dec” velocity profile measured in the mid-plane($z = 0$) and $x/c = 0.2$ at $t \sim 3.2$ s

Figure 3-65: Magnitude of instantaneous streamwise convective acceleration of the flow encountered by the translationally accelerating and decelerating 3D airfoil in the mid-plane($z = 0$), $x/c = 1.2$ at a time t when the term AC/U^2 at its peak.

than that in the “2g acc” and “5g dec” scenarios, which resulted in higher values of AC/U^2 for the former scenarios.

3-5 Translational Acceleration: Validation with the Experimental Results

3-5-1 Velocity & Acceleration profile for the accelerating airfoil

This section reviews the validation of the CFD model with the experimental results for the translationally accelerated airfoil in water in the RowBot facility at the Aero & Hydrodynamics Lab, TU Delft. A 3D airfoil with chord length $c = 111$ mm and a ground clearance $h = 30$ mm (i.e. $h/c = 0.270$) was accelerated translationally with the velocity profile in the Figure 3-66. The airfoil, initially at rest, is accelerated to a final velocity of 500 mm/s in $t = 0.45$ s. The chord Reynolds number of the airfoil varies from 0 to $\sim 56 \times 10^3$. In order to resemble this velocity profile for the simulation, a smooth velocity profile is generated using the Equation 2-2, as shown in the Figure 3-67(a). However, it must be noted that the smoothing function has its limitations, with the final velocity of 500 mm/s attained at $t = 1.0$ s instead of $t \sim 0.45$ s as in the experiment. For the peak translational acceleration of 1400 mm/s^2 , the value of the non-dimensional term AC/U^2 is approximately 2.4.

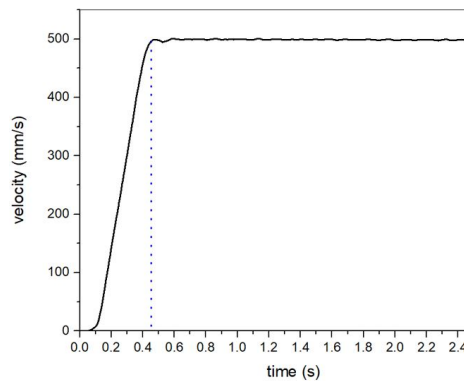


Figure 3-66: Velocity profile with which the airfoil is accelerated translationally in the experiment

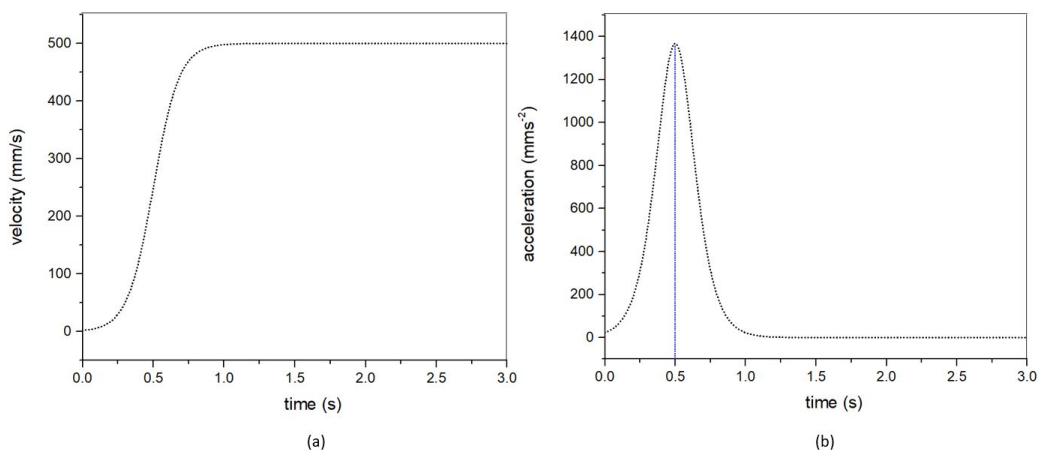


Figure 3-67: (a) Velocity profile with which the airfoil is accelerated translationally in the simulation to validate the CFD model, (b) Acceleration profile as the airfoil is accelerated translationally in the simulation to validate the CFD model, with peak acceleration attained at $t = 0.5$ s

3-5-2 Downforce generated by the airfoil & the drag force on the airfoil

A 2-dimensional airfoil was chosen to perform the numerical investigation to reduce the computational efforts. The 2D airfoil with chord length $c = 111$ mm, ground clearance $h/c = 0.270$ and aspect ratio 4.92 is accelerated translationally with the velocity profile in the Figure 3-67(a), with water as the working fluid. The downforce generated by the translationally accelerated 2D airfoil, and the drag force it experiences, is shown in the Figure 3-68.

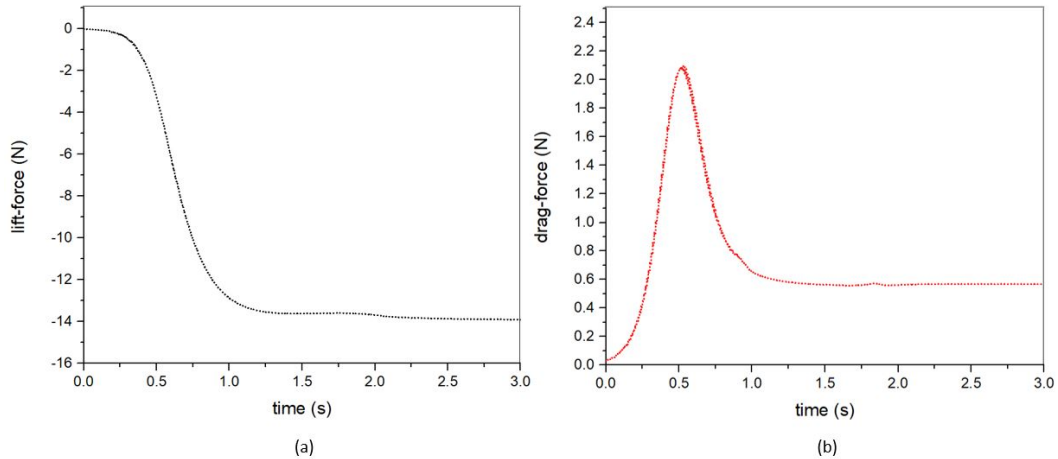


Figure 3-68: (a) Downforce generated by the 2D airfoil accelerated translationally with the velocity profile in Figure 3-67, (b) Drag force experienced by the translationally accelerated 2D airfoil with the velocity profile in Figure 3-67

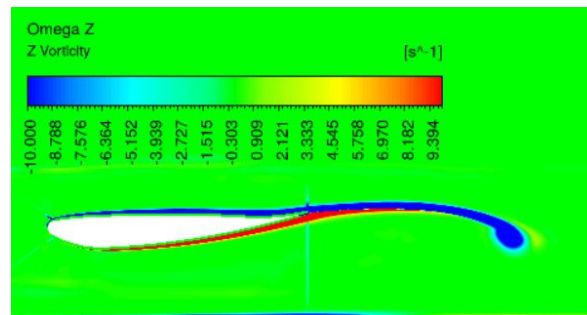


Figure 3-69: Starting vortex, indicated by the contour of instantaneous z-vorticity component, i.e, Ω_z at $t = 0.7$ s

From the plot in the Figure 3-68(b), it is evident that the drag force experienced by the 2D airfoil attains a peak value of 2.1 N, which coincides with the time at which peak translational acceleration is achieved by the airfoil, post of which it gradually drops to a steady state value of 0.6 N. This peak in the drag force can be attributed to added mass effects. Furthermore, from the plot in Figure 3-68(a), it can be seen that the steady state downforce value of 14 N is achieved by the 2D airfoil at a time $t > 1.0$ s. This is due to the influence of the starting vortex, shown in the Figure 3-69. The starting vortex, provides an upwash which decreases the effective angle of incidence of the flow and this, in turn, reduces the lift force generated by the airfoil. This phenomenon is known as the Wagner effect [63], which states that an

airfoil starting from rest must travel several chord lengths before attaining steady state lift values which are beyond the influence of the starting vortex.

As the airfoil with a non-zero angle of incidence moves steadily through a fluid, it has a circulation of the fluid around it, and this value of circulation, Γ , is given by the Kutta condition.

$$\Gamma = \pi c U \sin\alpha \quad (3-13)$$

where c is chord of the airfoil, U is velocity of the airfoil and α is the angle of incidence of the airfoil.

The lift per unit span as a result of the circulation around the airfoil in steady motion is given by the Kutta-Joukowski theorem.

$$L = \rho U \Gamma \quad (3-14)$$

where ρ is the density of the fluid. In the Equation 3-14, $\Gamma > 0$ for the circulation in the clockwise direction.

In the simulation, initially the airfoil is at rest, i.e., $U = 0$ and hence there is no circulation around it. Since Kelvin's circulation theorem states that circulation is neither created nor destroyed, as the airfoil is brought into motion, it must leave behind a vortex which is equal and opposite to the one around it. This vortex is known as the starting vortex and has a value of Γ .

The circulation of the airfoil must change to satisfy the Kutta condition, as it is accelerated. At the trailing edge of the airfoil, a vortex that is equal and opposite will tend to be shed into the wake, which delays the change in downforce due to the acceleration (similar to the Wagner effect) [64].

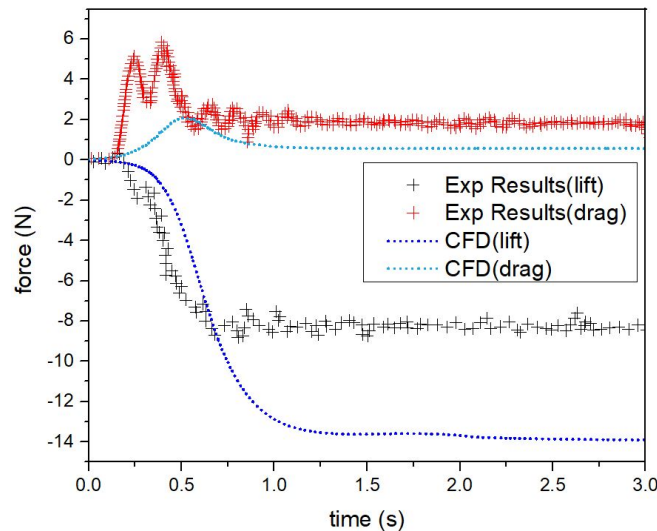


Figure 3-70: Starting vortex, indicated by the contour of instantaneous z-vorticity component, i.e., Ω_z at $t = 0.7s$

The Figure 3-70 shows the forces obtained for the translationally accelerated 2D airfoil, i.e., CFD results along with the forces obtained from the experiment. Although the magnitude of the forces are different, the trends in forces obtained from the experiment are similar to that of the CFD results.

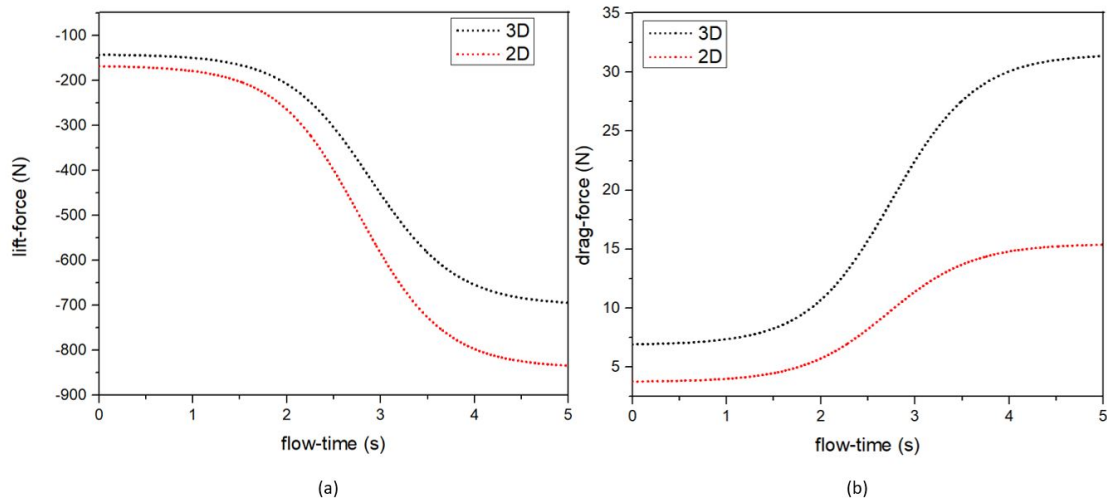


Figure 3-71: (a) Downforce generated by the 2D and 3D airfoil accelerated translationally with the “2g acc” velocity profile, (b) Drag force on the 2d and 3D airfoil accelerated translationally with the “2g acc” velocity profile. The downforce generated by the translationally accelerated airfoil is higher than that by the 3D airfoil, whereas the drag force experienced by the translationally accelerating 2D airfoil is lower than the 3D airfoil.

The difference in the magnitude of the forces between the experiment and the numerical simulation can be attributed to 2D v/s 3D effects. The Figure 3-71, shows the forces obtained for the 2D airfoil and 3D of chord length $c = 223.4$ mm, ground clearance $h/c = 0.224$ and aspect ratio 4.92 accelerated translationally with the “2g acc” velocity profile in the Section 3-4-1. These forces are consistent with the results in the Figure 3-70, where the aerodynamic forces, i.e, the downforce and the drag force, are higher for the 2D airfoil when compared to that for the 3D wing.

Conclusions

4-1 Summary

The present study is aimed at improving the correlation between the wind-tunnel tests carried out for the racecars and the on-track behavior of the racecar, where the racecar accelerates and decelerates, unlike the wind-tunnel tests where the experiments are carried out at constant velocities.

In Chapter 1, a comprehensive literature on the principle of downforce generation and its significance in motorsports is reviewed. The fundamentals of ground effect aerodynamics, the boundary layer, vortices and accelerating flow were also discussed. Furthermore, experimental observations along with the numerical investigations of wings in ground effect is briefly discussed. An important finding from the previous researchers was the increased drag force, when a flat plate was subjected to accelerating motion. Furthermore, previous studies revealed that an airfoil in the free stream subjected to accelerating and decelerating motion generated lift forces which were different from that at the same steady state velocities. These studies are extended to a racecar wing in ground effect, where a numerical investigation is performed on the translationally accelerating and decelerating airfoils in ground effect.

In Chapter 2, the sequential steps that are involved in the numerical modelling process, namely: the geometrical setup, flow scenarios, computational domain, meshing, the boundary conditions and turbulence modelling are reviewed along with the solutions methods that are implemented. Furthermore, the results of a turbulence model validation study performed are also briefly discussed. The SST $k-\omega$ turbulence model returned satisfactory force coefficients, while capturing all the relevant flow physics, and hence this model was used in the sequel.

ANSYS-Fluent 19R2 was employed to perform the CFD simulations, and the results obtained are the topic of discussion in Chapter 3. The mesh independence study performed revealed that as the number of points on the airfoil circumference increased, the CFD simulation was able to capture the pressure distribution on the airfoil surface, which agreed with results from the experiment. Based on these results, for all further simulations, the number of points on the airfoil circumference was set at 600 and a wall $y^+ \sim 1$ was maintained.

A scaling analysis was performed to determine the important parameters that influence the flow for a translationally accelerating airfoil. The scaling analysis revealed that the two non-dimensional numbers that govern the flow for a translationally accelerating airfoil are the chord Reynolds and Froude number. For the magnitudes of acceleration that a racecar undergoes on the racetrack, the Froude number is shown to be insignificant. Based on these findings, it is expected that an airfoil accelerating (or decelerating) exhibits quasi-stationary behavior only when the Froude number is insignificant. In such instances, the aerodynamic forces are entirely dependent on the chord Reynolds number. These expectations were tested using numerical simulations. In these numerical simulations, two different velocity profiles were employed for translationally accelerating (and decelerating) the airfoil, namely; the piecewise linear profile and smooth non-linear profile. The forces obtained for the airfoil accelerated with the piecewise linear profile exhibited false peaks, which were a result of the acceleration profile not being smooth. Furthermore, the added mass effects that resulted in an increase in the drag force were narrowed down to increased pressure drag. The peaks in the forces that were observed in the results for the airfoil accelerated translationally with the piecewise linear velocity profile were eliminated when a smooth velocity profile was employed to translationally accelerate the airfoil.

Although no peaks in the forces were observed for the airfoil accelerated translationally with the smooth non-linear velocity profile, the instantaneous force coefficients revealed that the airfoil experienced a temporary loss of downforce coefficient and encountered a temporary increase in the drag coefficient. Likewise, the translationally decelerating airfoil experienced a temporary gain in the downforce coefficient and encounters a temporary reduction in drag coefficient. The temporary increase and decrease in drag coefficient was attributed to added mass effects. Meanwhile, the temporary loss of downforce coefficient of the translationally accelerating airfoil was attributed to the pressure distribution on the suction side, which at any given time was not as low as the pressure distribution at the same velocity under the steady-state conditions. Similarly, for the translationally decelerating airfoil, the pressure distribution on the suction side of the decelerating airfoil at any given time was to be higher than the pressure distribution at the same velocity under steady-state conditions, which resulted in a temporary gain in the downforce coefficient.

An angle of incidence study was performed to study its effect on the forces of a translationally accelerating airfoil, which revealed that the higher the angle of incidence, the lower is the effect of the translational acceleration on the aerodynamic forces. This was narrowed down to the magnitude of convective acceleration of the fluid encountered by the translationally accelerating airfoil at a higher angle of incidence being greater than that encountered by the translationally accelerating airfoil at a lower angle of incidence. The imposed translational acceleration of the airfoil thus has a smaller effect.

An investigation into the impact of the magnitude of the acceleration on the aerodynamic forces of the translationally accelerating (and decelerating) airfoil was carried out, which revealed that the higher the magnitude of the translational acceleration (or deceleration) of the airfoil when compared to that of the convective acceleration of the flow encountered by the airfoil, the higher was the influence of translational acceleration on the forces. The magnitude of the temporary loss/gain in the aerodynamic forces of a translationally accelerating airfoil was highly dependent on the magnitude of translational acceleration (or deceleration). These findings are consistent with the expectations from scaling analysis, i.e., the influence of the translational acceleration (or deceleration) on the forces appear stronger when the magnitude

of translational acceleration(or deceleration) is increased.

The investigations on the location of the flow separation point revealed that, when the airfoil was subjected to translational acceleration, the location of the separation point moved downstream with time. Likewise, for the translationally decelerating airfoil, the location of the separation point shifted upstream with time.

Investigations into the strength of the primary vortex revealed that the primary vortex undergoes a temporary loss in strength when the airfoil was accelerated translationally, indicated by the instantaneous streamwise vorticity contours and this was reflected in the instantaneous downforce coefficient curve where it underwent a temporary loss in downforce. Similarly, when the airfoil was accelerated translationally, the primary vortex experienced a temporary increase in its strength, which was consistent with the instantaneous downforce coefficient curve where it underwent a temporary gain in downforce.

4-2 Recommendations

- The sequence of motions that are involved as a racecar travels through a corner are deceleration, cornering and acceleration. While decelerating and accelerating motions of an airfoil(or wing) are covered in the present study, the cornering motion is of high relevance as well. Understanding the aerodynamic forces as the wing is subjected to cornering motion and slip angles, combined with the results from the present study, will help in improving the correlation between the aerodynamic forces from the wind tunnel experiments and on-track behavior.
- The present investigation was carried out for a single element wing. This study needs to be extended to multi-element wings to investigate the influence of translational acceleration and deceleration on the interaction between vortical structures. The interaction between vortices is important from a fundamental perspective and is vital for car body aerodynamics. Furthermore, it can aid in improving the correlation between the wind tunnel experiment and on-track behavior of the racecar, as modern cars employ multi-element wings.
- The present study is aimed at realistic values of accelerations and velocities that a race car can attain on a racetrack, which resulted in low values of the Froude number. From a fundamental perspective, it would be interesting to observe the influence of acceleration on the aerodynamic forces when the airfoil is subjected to high Froude number accelerations, i.e., high magnitudes of acceleration and low velocity magnitudes.

Appendix A

Tyrrell Wing Profile

The coordinates used for generating the inverted airfoil are below.

Suction surface		Pressure surface	
x/c	y/c	x/c	y/c
0	0	0	0
0.001	-0.0076	0.001	0.0079
0.002	-0.0107	0.002	0.0109
0.0049	-0.0168	0.0051	0.0173
0.0099	-0.0228	0.0101	0.0232
0.0149	-0.0266	0.0151	0.0271
0.0199	-0.0294	0.0201	0.03
0.0249	-0.032	0.0251	0.0313
0.0298	-0.0345	0.0301	0.0322
0.0348	-0.0369	0.0351	0.033
0.0398	-0.0393	0.0401	0.0338
0.0448	-0.0416	0.0451	0.0346
0.0498	-0.0438	0.0501	0.0354
0.0548	-0.046	0.0551	0.0361
0.0598	-0.0481	0.0601	0.0369
0.0698	-0.052	0.0701	0.0382
0.0797	-0.0557	0.0801	0.0395
0.0897	-0.0591	0.0902	0.0407
0.0997	-0.0622	0.1002	0.0417
0.1197	-0.0676	0.1202	0.0436
0.1396	-0.0718	0.1402	0.0451
0.1596	-0.075	0.1602	0.0463
0.1796	-0.0769	0.1802	0.0472
0.1996	-0.0778	0.2002	0.048
0.2496	-0.0762	0.2501	0.0498

0.2996	-0.0732	0.3001	0.0515
0.3496	-0.0692	0.3501	0.0527
0.3996	-0.0645	0.4001	0.0534
0.4496	-0.059	0.4501	0.0537
0.4996	-0.0526	0.5001	0.0535
0.5497	-0.0454	0.5501	0.0529
0.5997	-0.0373	0.6001	0.0518
0.6497	-0.0285	0.65	0.0503
0.6997	-0.0188	0.7	0.0482
0.7498	-0.0083	0.75	0.0456
0.7998	0.0031	0.8	0.0438
0.8498	0.0152	0.85	0.0443
0.8999	0.0282	0.9	0.0479
0.9199	0.0336	0.92	0.0502
0.9399	0.0392	0.94	0.053
0.9599	0.0449	0.96	0.0562
0.9799	0.0507	0.98	0.0599
0.99	0.0537	0.99	0.0619
1	0.0567	1	0.064

Table A-1: Single element wing coordinates at an angle of incidence 3.45°

Appendix B

Eddy viscosity models

This appendix is intended to give a brief overview of the RANS eddy viscosity models available in the ANSYS Fluent.

Focusing on industrial aircraft aerodynamics, a one equation model which has a transport eddy viscosity was developed by Spalart et al.[30] The transport equation for eddy viscosity(μ_t) is solved for by the relatively simple Spalart-Allmaras model and has shown to give good results for boundary layers subjected to adverse pressure gradients. Although the complexity of the Spalart-Allmaras model is less, the model behaves poorly for cases where flow separation occurs[65] and is hence ruled out of scope for this research. A higher accuracy model is desired for automotive aerodynamics as there exists a variation in geometries of complex bluff bodies which result in different separation and wake patterns.

A brief description of the theory behind the standard, RNG and the realizable k - ϵ models is looked into. All three models solve two additional transport equations for the turbulent kinetic energy k and the turbulence dissipation rate ϵ . The differences between the three models are listed below.

- the method with which turbulent viscosity is calculated.
- the turbulent Prandtl numbers, which govern the turbulent diffusion of k and ϵ
- the generation and destruction terms in the ϵ transport equation.

The realizable k - ϵ model has been extensively validated for a variety of flows[66, 36] which include rotating homogeneous shear flows, channel and boundary layer flows, free flows including jets and mixing layers, and separated flows. The realizable k - ϵ model was found to offer better performance than the standard k - ϵ model for all the cases. Also, previous works[32, 52, 8, 48] have indicated that the realizable k - ϵ model was able to offer good correlations with the aerodynamic forces obtained from the wind tunnel experiments for the case of an inverted wing in ground effect.

A brief description of the theory behind the standard and the SST $k-\omega$ models is looked into. All three models solve two additional transport equations for the turbulent kinetic energy k and the specific dissipation rate ω . The differences in approach for the SST $k-\omega$ model from the standard $k-\omega$ model are listed below.

- gradual switch from the standard $k-\omega$ model in the inner region of the boundary layer to a high Reynolds number variant of the $k-\epsilon$ model in the outer region of the boundary layer.
- in order to account for the transport effects of the principal turbulent shear stress, the turbulent viscosity is modified.

The SST $k-\omega$ model has been found to be more accurate and reliable for a wide variety of flows, which include flows where adverse pressure gradients are encountered and flow over airfoils, when compared to the standard $k-\omega$ model[59]. Previously, numerical investigation on influence of cornering on wings in ground effect[12] and numerical investigation on aerodynamics of inverted three element wing[49] have employed the SST $k-\omega$ model. The SST $k-\omega$ model was found capable to predict flow separation and offer reasonable predictions in the wake region of the wing in ground effect.

The $k-k_L-\omega$ transition model is employed by ANSYS Fluent to predict the development of the boundary layer and determine the onset of transition from laminar to turbulent regime[67]. Three additional transport equations for turbulent kinetic energy k_t , laminar kinetic energy k_L and the inverse turbulent timescale ω are solved. The laminar and turbulent fluctuations of the mean flow are included in the expressions for the eddy viscosity and thermal diffusivity. Numerical investigations on flows over single and multi-element wings[50] revealed that the $k-k_L-\omega$ transition model was capable of capturing the presence of a laminar separation bubble on the wing and returned reasonable prediction for the lift and drag forces compared to the data from wind tunnel experiments.

The transition SST model is based on combining the transport equations of the SST $k-\omega$ along with two other transport equations, one for the intermittency γ and one for the transition onset criteria, in terms of momentum-thickness Reynolds number Re_θ .

A more comprehensive review of these turbulence models can be found in the ANSYS Fluent user manual[59].

Accelerating Airfoil: Moving Frame of Reference and Stationary Frame of Reference

An accelerating airfoil can be modelled using two approaches in Fluent, as discussed in the Section 2-4-1, namely; the moving frame of reference approach and the stationary frame of reference approach. The former approach resembles the real-life on track scenario where the airfoil is accelerating, while the latter resembles the wind tunnel tests where the airfoil is stationary and the flow is accelerated past the airfoil. The ground must be modelled using appropriate boundary conditions for the two different approaches. Care must be taken to ensure that the ground is stationary with respect to the moving airfoil.

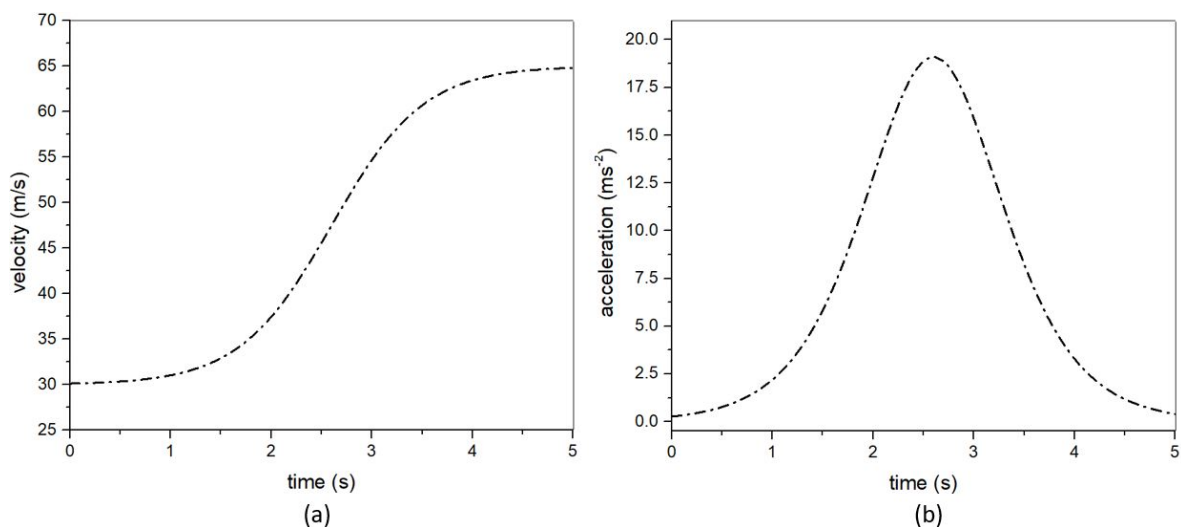


Figure C-1: (a) Velocity profiles for accelerating airfoil, (b) Acceleration profile for accelerating airfoil

For this comparison study between the two different approaches, a 2-dimensional airfoil with a ground height, $h = 0.179c$, is chosen. The chord length, c , is 223.4 mm and the geometric aspect ratio of the wing is 4.92. The velocity profile chosen for the accelerating airfoil is the non-linear velocity profile that resembles the one a racecar is likely to undergo on a racetrack.

C-1 Boundary Conditions

For the moving frame of reference approach, the fluid domain is moved with the velocity profile in the Figure C-1(a) in the negative x-direction. The airfoil is modelled as a no-slip moving wall with a zero relative velocity to the fluid. The ground is modelled as a stationary, no-slip wall in the absolute frame. The inlet is modelled as a zero velocity inlet in the absolute frame and the pressure outlet is specified a uniform gauge pressure 0 Pa relative to the atmospheric pressure of 101,325 Pa.

For the stationary frame of reference approach, the boundary conditions are set using the methods discussed in 2-4-1.

C-2 Results: Forces and Flow Fields

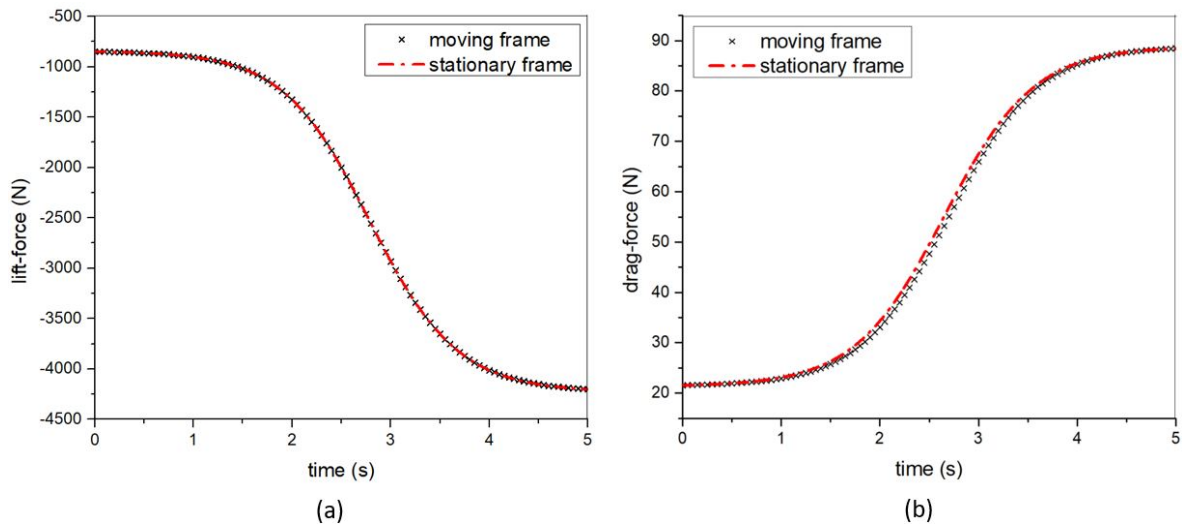


Figure C-2: (a)Downforce generated by the accelerating airfoil, (b)Drag force on the accelerating airfoil

The instantaneous downforce generated by the airfoil and the drag force on the accelerating airfoil is monitored as a function of time. The forces, in the Figure C-2, show that the downforce generated by the accelerating airfoil in the moving frame approach and the stationary frame approach are almost the same. Similarly, the drag forces on the accelerating airfoil in the both the moving frame and stationary frame approach are almost the same, with minute differences between them. The difference in the downforces and the drag force between the moving frame and stationary frame approach is $\sim 0.01\%$. These minute differences can be attributed to numerical errors not being Galilean invariant.

The pressure and the velocity fields for the accelerating airfoil in the moving frame and stationary frame are also identical, as shown in the Figure C-3 and C-4.

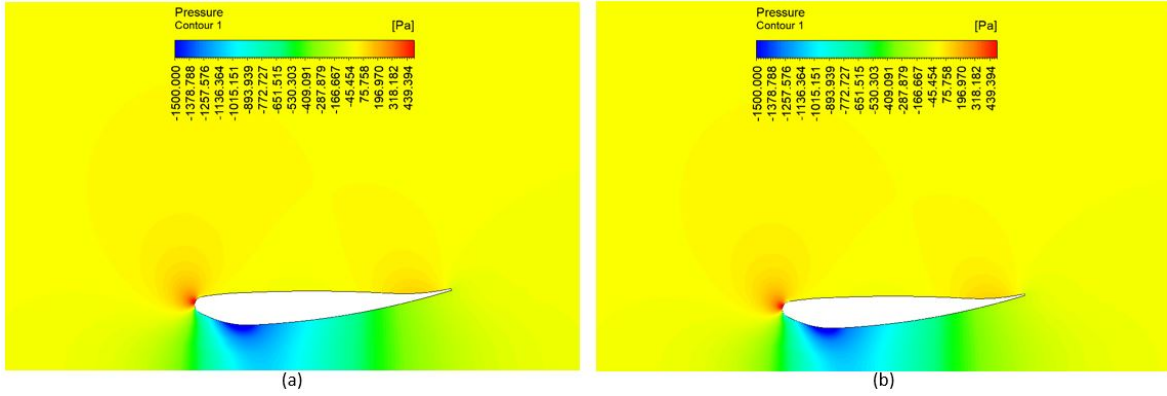


Figure C-3: (a) Instantaneous pressure field for accelerating airfoil in the moving frame at $t = 0s$, (b) Instantaneous pressure field for accelerating airfoil in the stationary frame at $t = 0s$

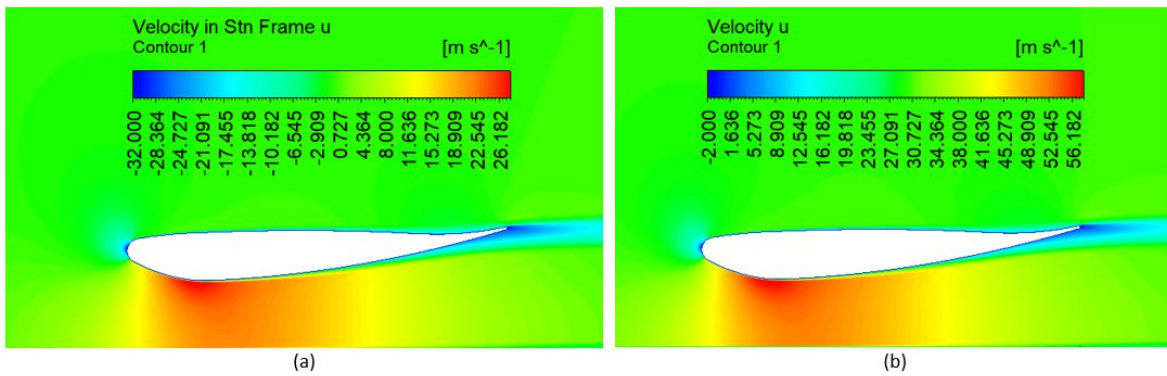


Figure C-4: (a) Instantaneous x-velocity field for accelerating airfoil in the moving frame at $t = 0s$, (b) Instantaneous x-velocity field for accelerating airfoil in the stationary frame at $t = 0s$

Appendix D

Fluent settings

The solver settings in ANSYS Fluent 2019R3 are listed in this Appendix.

1. **Solver**

- (a) Type: Pressure-based
- (b) Velocity type: Absolute
- (c) Time: Transient

2. **Turbulence Model:**SST $k - \omega$

3. **Materials:** Air with default properties at 20°C

- Density, $\rho = 1.225\text{kg}/\text{m}^3$
- Dynamic Viscosity, $\mu = 1.789 \times 10^{-5}\text{Pas}$

4. **Cell Zone Conditions:**

- Phase: Fluid (all volumes)
- Operating pressure: 101325 Pa
- Reference pressure location: Velocity inlet BC

5. **Boundary conditions:** explained in Sections 2-4-1 and 2-4-2.

6. **Solution methods:**

- Pressure velocity coupling scheme: SIMPLE.
- Spatial discretization:
 - (a) Gradient: Least Squares Cell Based.
 - (b) Pressure: Second Order
 - (c) Momentum: Third Order MUSCL.

- (d) Turbulent kinetic energy: Second Order Upwind.
- (e) Specific dissipation rate: Second Order Upwind.
- Transient Formulation: Bounded Second Order Implicit.

7. **Initialization:** Hybrid Initialization

Bibliography

- [1] F. .-T. O. F. Website, “Tech tuesday: The lotus 79, fl’s ground effect marvel,” Aug 2018.
- [2] W. Toet, “Aerodynamics and aerodynamic research in formula 1,” *The Aeronautical Journal*, vol. 117, no. 1187, pp. 1–26, 2013.
- [3] J. Carlton, “Chapter 7 - theoretical methods—basic concepts,” in *Marine Propellers and Propulsion (Fourth Edition)* (J. Carlton, ed.), pp. 141–175, Butterworth-Heinemann, fourth edition ed., 2019.
- [4] J. Katz, “Aerodynamics of race cars,” *Annu. Rev. Fluid Mech.*, vol. 38, pp. 27–63, 2006.
- [5] J. Zerihan, *An investigation into the aerodynamics of wings in ground effect*. PhD thesis, University of Southampton, 2001.
- [6] X. Zhang, J. Zerihan, A. Ruhrmann, and M. Deviese, “Tip vortices generated by a wing in ground effect,” in *Proceedings of the 11th International Symposium on Applications of Laser Techniques to Fluid Mechanics*, Citeseer, 2002.
- [7] J. Zerihan and X. Zhang, “A single element wing in ground effect-comparisons of experiments and computation,” in *39th Aerospace Sciences Meeting and Exhibit*, p. 423, 2001.
- [8] J. W. Vogt and T. J. Barber, “Ground effect phenomena about lift and downforce generating cambered aerofoils,” *International Journal of Numerical Methods for Heat & Fluid Flow*, 2012.
- [9] Wikipedia, “Hurricane katrina,” Oct 2021.
- [10] P. G. Saffman, *Vortex dynamics*. Cambridge university press, 1995.
- [11] A. Fraser-Mitchell, “Fundamentals of aerodynamics—fifth edition, jd anderson, mcgraw-hill, shoppenhangers road, maidenhead, berkshire, sl6 2ql, uk. 2011. 1098pp. illustrated.£ 47.99. isbn 978-007-128908-5.,” *The Aeronautical Journal*, vol. 116, no. 1176, pp. 222–223, 2012.

-
- [12] J. Keogh, G. Doig, S. Diasinos, and T. Barber, "The influence of cornering on the vortical wake structures of an inverted wing," *Proceedings of the Institution of Mechanical Engineers, Part D: Journal of Automobile Engineering*, vol. 229, no. 13, pp. 1817–1829, 2015.
- [13] R. Ellsworth and T. Mueller, "Airfoil boundary layer measurements at low re in an accelerating flow from a nonzero velocity," *Experiments in fluids*, vol. 11, no. 6, pp. 368–374, 1991.
- [14] H. Roohani, "Aerodynamic effects of accelerating objects in air," *University of the Witwatersrand, Johannesburg*, 2010.
- [15] E. Grift, N. Vijayaragavan, M. Tummers, and J. Westerweel, "Drag force on an accelerating submerged plate," *Journal of Fluid Mechanics*, vol. 866, pp. 369–398, 2019.
- [16] I. H. Finlay and J. Roberts, "Corner analysis, <https://aws.amazon.com/f1/corner-analysis/>," 2020.
- [17] P. Wright, "The influence of aerodynamics on the design of formula one racing cars," *International Journal of Vehicle Design*, vol. 3, no. 4, pp. 383–397, 1982.
- [18] A. F. Zahm and R. Bear, "Ground-plane influence on airplane wings," *Journal of the Franklin Institute*, vol. 191, no. 5, pp. 687–693, 1921.
- [19] E. Pistolesi, "Ground effect-theory and practice," 1937.
- [20] A. Gopalarathnam, B. A. Broughton, B. D. McGranahan, and M. S. Selig, "Design of low reynolds number airfoils with trips," *Journal of aircraft*, vol. 40, no. 4, pp. 768–775, 2003.
- [21] P. Owen and L. Klanfer, "On the laminar boundary layer separation from the leading edge of a thin aerofoilv," tech. rep., AERONAUTICAL RESEARCH COUNCIL LONDON (UNITED KINGDOM), 1953.
- [22] P. K. Chang, "Separation of flow," *Journal of the Franklin Institute*, vol. 272, no. 6, pp. 433–448, 1961.
- [23] J. Zerihan and X. Zhang, "Aerodynamics of a single element wing in ground effect," *Journal of aircraft*, vol. 37, no. 6, pp. 1058–1064, 2000.
- [24] X. Zhang and J. Zerihan, "Aerodynamics of a double-element wing in ground effect," *AIAA journal*, vol. 41, no. 6, pp. 1007–1016, 2003.
- [25] K. Knowles, D. T. Donoghue, and M. V. Finnis, "A study of wings in ground effect, conference, vehicle aerodynamics," in *Vehicle aerodynamics, Conference, Vehicle aerodynamics*, pp. 22.1–22.13, Royal Aeronautical Society;, 1994.
- [26] R. Ranzenbach and J. B. Barlow, "Two-dimensional airfoil in ground effect, an experimental and computational study," tech. rep., SAE Technical Paper, 1994.
- [27] R. Ranzenbach and J. Barlow, "Cambered airfoil in ground effect-wind tunnel and road conditions," in *13th Applied Aerodynamics Conference*, p. 1909, 1995.

-
- [28] R. Ranzenbach, J. Barlow, R. Diaz, R. Ranzenbach, J. Barlow, and R. Diaz, "Multi-element airfoil in ground effect-an experimental and computational study," in *15th Applied Aerodynamics Conference*, p. 2238, 1997.
- [29] W. J. Jasinski and M. S. Selig, "Experimental study of open-wheel race-car front wings," *SAE transactions*, pp. 2549–2557, 1998.
- [30] P. Spalart and S. Allmaras, "A one-equation turbulence model for aerodynamic flows," in *30th aerospace sciences meeting and exhibit*, p. 439, 1992.
- [31] F. Menter, "Zonal two equation kw turbulence models for aerodynamic flows," in *23rd fluid dynamics, plasmadynamics, and lasers conference*, p. 2906, 1993.
- [32] S. Mahon and X. Zhang, "Computational analysis of pressure and wake characteristics of an aerofoil in ground effect," 2005.
- [33] B. E. Launder and D. B. Spalding, "The numerical computation of turbulent flows," in *Numerical prediction of flow, heat transfer, turbulence and combustion*, pp. 96–116, Elsevier, 1983.
- [34] D. C. Wilcox, "Multiscale model for turbulent flows," *AIAA journal*, vol. 26, no. 11, pp. 1311–1320, 1988.
- [35] V. Yakhot and S. A. Orszag, "Renormalization group analysis of turbulence. i. basic theory," *Journal of scientific computing*, vol. 1, no. 1, pp. 3–51, 1986.
- [36] T.-H. Shih, W. W. Liou, A. Shabbir, Z. Yang, and J. Zhu, "A new k- eddy viscosity model for high reynolds number turbulent flows," *Computers & fluids*, vol. 24, no. 3, pp. 227–238, 1995.
- [37] P. Durbin, "A reynolds stress model for near-wall turbulence," *Journal of Fluid Mechanics*, vol. 249, pp. 465–498, 1993.
- [38] J. Jeong and F. Hussain, "On the identification of a vortex," *Journal of fluid mechanics*, vol. 285, pp. 69–94, 1995.
- [39] S. I. Green, "Introduction to vorticity," in *Fluid Vortices*, pp. 1–34, Springer, 1995.
- [40] J. M. Delery, "Aspects of vortex breakdown," *Progress in Aerospace Sciences*, vol. 30, no. 1, pp. 1–59, 1994.
- [41] S. I. Green, "Wing tip vortices," in *Fluid Vortices*, pp. 427–469, Springer, 1995.
- [42] W. Phillips, "The turbulent trailing vortex during roll-up," *Journal of Fluid Mechanics*, vol. 105, pp. 451–467, 1981.
- [43] P. Saffman and G. Baker, "Vortex interactions," *Annual Review of Fluid Mechanics*, vol. 11, no. 1, pp. 95–121, 1979.
- [44] C. K. Batchelor and G. Batchelor, *An introduction to fluid dynamics*. Cambridge university press, 2000.

-
- [45] P. Freymuth, W. Bank, and M. Palmer, "Visualization of accelerating flow around an airfoil at high angles of attack.," tech. rep., COLORADO UNIV AT BOULDER DEPT OF AEROSPACE ENGINEERING SCIENCES, 1982.
- [46] Y.-T. Yu, "Virtual masses of rectangular plates and parallelepipeds in water," *Journal of Applied Physics*, vol. 16, no. 11, pp. 724–729, 1945.
- [47] A. Kageyama and M. Hyodo, "Eulerian derivation of the coriolis force," *Geochemistry, Geophysics, Geosystems*, vol. 7, no. 2, 2006.
- [48] J. Keogh, G. Doig, T. J. Barber, and S. Diasinos, "The aerodynamics of a cornering inverted wing in ground effect," in *Applied Mechanics and Materials*, vol. 553, pp. 205–210, Trans Tech Publ, 2014.
- [49] Q. Qu, P. Zuo, Y. Qin, P. Liu, and R. K. Agarwal, "Numerical investigation of the aerodynamics of an inverted three-element airfoil in ground effect for race car application," in *34th AIAA Applied Aerodynamics Conference*, p. 4180, 2016.
- [50] L. Roberts, M. Finnis, and K. Knowles, "Modelling boundary-layer transition on wings operating in ground effect at low reynolds numbers," *Proceedings of the Institution of Mechanical Engineers, Part D: Journal of Automobile Engineering*, vol. 233, no. 11, pp. 2820–2837, 2019.
- [51] K. Nara, M. Tsubokura, and J. Ikeda, "A numerical analysis of unsteady aerodynamics of formula car during dynamic cornering motion," in *32nd AIAA applied aerodynamics conference*, p. 3138, 2014.
- [52] S. Mahon and X. Zhang, "Computational analysis of a inverted double-element airfoil in ground effect," 2006.
- [53] S. B. Pope and S. B. Pope, *Turbulent flows*. Cambridge university press, 2000.
- [54] M. Tsubokura, K. Kitoh, N. Oshima, T. Nakashima, H. Zhang, K. Onishi, and T. Kobayashi, "Large eddy simulation of unsteady flow around a formula car on earth simulator," *SAE Transactions*, pp. 40–49, 2007.
- [55] P. W. Egolf and K. Hutter, "Reynold's averaging of the navier–stokes equations (rans)," in *Nonlinear, Nonlocal and Fractional Turbulence*, pp. 13–18, Springer, 2020.
- [56] R. Cant, "Sb pope, turbulent flows, cambridge university press, cambridge, uk," *Combustion and Flame*, vol. 125, pp. 1361–1362, 2001.
- [57] Pointwise, "Pointwise User Manual."
- [58] G. Doig, T. J. Barber, and A. J. Neely, "The influence of compressibility on the aerodynamics of an inverted wing in ground effect," *Journal of fluids engineering*, vol. 133, no. 6, 2011.
- [59] U. Manual, "Ansys fluent 12.0," *Theory Guide. Canonsburg, PA*, 2009.
- [60] A. Fluent, "16.0, ansys fluent user's guide. ansys," 2015.

- [61] J. N. Newman, *Marine hydrodynamics*. The MIT press, 2018.
- [62] E. H. Kennard, “Irrotational flow of frictionless fluids, mostly of invariable density,” Jan 1967.
- [63] H. Wagner, “Über die entstehung des dynamischen auftriebes von tragflügeln,” 1924.
- [64] J. Wakeling, “Dragonfly aerodynamics and unsteady mechanisms: a review,” *Odonatologica*, vol. 22, no. 3, pp. 319–334, 1993.
- [65] D. C. Wilcox *et al.*, *Turbulence modeling for CFD*, vol. 2. DCW industries La Canada, CA, 1998.
- [66] S.-E. Kim, D. Choudhury, and B. Patel, “Computations of complex turbulent flows using the commercial code fluent,” in *Modeling complex turbulent flows*, pp. 259–276, Springer, 1999.
- [67] D. K. Walters and D. Cokljat, “A three-equation eddy-viscosity model for reynolds-averaged navier–stokes simulations of transitional flow,” *Journal of fluids engineering*, vol. 130, no. 12, 2008.